IN SITU REAL-TIME RUTHERFORD BACKSCATTERING SPECTROMETRY STUDY OF Ni/Ge INTERACTION

A dissertation submitted to the University of Zambia in partial fulfillment of the requirements for the degree of

Master of Science

(Physics)

by

Kanyembo Justin Pondo

July 2010

Professor C.M. Comrie

(Title and Name)

Supervisor

Dr. A. Habanyama

(Title and Name)

Supervisor

Abstract

Silicon-based microelectronic technology is approaching its performance limits due to the rapid downscaling of electronic devices to ever smaller dimensions. Germanium, with its high electron and hole mobility, high carrier injection velocity, very low carrier free-out temperature, etc. is generally considered to be a possible replacement for silicon as the semiconductor of choice for high-performance devices. Before germanium can be adopted a suitable material for making electrical contact to the active areas of the germanium based devices must be identified. In analogy with the current Si-based technology where metal-silicides are used as contacts for the active areas of the devices, the use of metal-germanides is proposed for this purpose. Of all

possible metal-germanides, nickel monogermanide (NiGe) appears to be the most promising. In order to successfully make use of nickel germanides in Ge-based devices it is essential to thoroughly understand all processes and mechanisms involved in germanium metallization as well as the properties of the phases formed. This is necessary in order to avoid or control problems that can be encountered during integration. Some of the important information required during fabrication includes the identification of the phase formation sequence, dominant diffusing species and growth kinetics during the germanidation process.

Rutherford backscattering spectrometry (RBS) is one of the most powerful and frequently used analytical tools for analysis of composition, thickness and depth profiles of thin solid films or surface and near-surface regions of solids. It has proved to be a very valuable technique in studying the growth characteristics during phase formation. In conventional RBS a number of samples are prepared and annealed in sequence for various durations or at different temperatures to induce differing amounts of phase formation. These specimens are subsequently analyzed to unravel the phase formation characteristics. In contrast, the in situ real-time (i.e. during annealing) RBS used in this study allows all the phase formation information to be conveniently obtained from one sample in a single experimental run. This has the advantages of decreasing the workload, reducing material consumption and eliminating the influence of small differences in the sample preparation procedure and experimental conditions. Additionally, it enables one to follow the reaction at all stages of compound growth which limits the risk of overlooking important steps during the phase formation process.

Two samples prepared in high vacuum by electron beam evaporation have been used in this investigation. In both samples thin layers of tantalum approximately 5-6 Å thick have been used as inert markers to monitor the direction of atomic mobility. The first sample had a configuration of Ge<100>/Ta(5 Å)/Ni(800 Å) while the configuration of the second sample was Ge<100>/Ta(6 Å)/Ge(490 Å)/Ni(470 Å). The solid state reactions of nickel with germanium were induced by in situ ramped thermal annealling in a scattering chamber. Using a 2 MeV $^{4}He^{+}$ beam the formation characteristics of the nickel germanides were captured in real-time. The phase formation sequence has been identified to begin with the formation of Ni_5Ge_3 followed by NiGe. The RBS data acquired from the first sample revealed the formation of the Ni_5Ge_3 phase to commence at around 145 ^{o}C and also showed the simultaneous growths of Ni_5Ge_3 and NiGe. It was found from the first sample that Ni was the sole diffusing species during Ni_5Ge_3 formation. The formation of Ni_5Ge_3 in the second sample was observed at room temperature. In this sample it was found that both Ni and Ge diffused during the formation of NiGe. However, Ni was the dominant diffusing species during the growth of the NiGe phase. The activation energy of diffusional growth of Ni_5Ge_3 was found to be 0.75 ± 0.01 eV.

Keywords: Nickel germanides, In situ real-time, Ramped thermal anneal, Dominant diffusing species, RBS, simultaneous growth.

Plagiarism

I solemnly declare that this thesis represents original work which has not been submitted for a degree at this or any other university.

The work reported on in this dissertation conforms to the principles and requirements of the University's guidelines for ethics in research.

The University has permission to keep, to lend or to copy this dissertation in whole or in part on condition that any such use of the material of the dissertation is duly acknowledged.

Signature: ……..

Dedication

To the scientific community for their philosophical acceptance and endurance of the troubles the quest for knowledge entails.

Acknowledgements

The successful completion of this research project report is a result of the numerous contributions of many people. Their assistance, guidance, encouragement and support have not

escaped my attention. To all these people I say I owe you a debt of gratitude and only you know the depth of my indebtedness. Although it is not possible to enumerate all their names here, I want them to know that I whole heartedly appreciate their contributions.

Firstly, I owe a debt of gratitude to my supervisors Prof. C. M. Comrie of the University of Cape Town and Dr. A. Habanyama of the University of Zambia for not only introducing me to solid phase reactions but also for their meticulous supervision and guidance throughout the course of this research work which will remain a valuable lesson for my future research endeavors. Their patience and attention to detail made me really enjoy their company, and through them, I have acquired a lot of research skills.

Particular thanks go to the project coordinator, Dr. G. K. Chinyama, for initiating the Master of Science degree program in Materials Science.

Special thank must be to Prof. P. C. Jain, Prof. P. N. Kaloyerou, Dr. H. V. Mweene, Dr. A. Habanyama, and Dr. G. K. Chinyama for the excellent way in which they handled the course work part of this study and through them the entire academic staff of the Physics Department of the University of Zambia.

I have great pleasure in thanking the technical staff in the Physics Department of the University of Zambia for the all round support they rendered to me in all phases of this postgraduate course.

I thank the entire staff at the University of Cape Town for their facilities and hospitality during my stay there.

I wish to express my gratitude to Lesley Jennings and Nan Warner who worked very well with Prof. Comrie to secure good accommodation for me while in Cape Town.

I also wish to give special thanks to iThemba Labs (formally the National Accelerator Center at Faure) for the provision of materials and equipment from which the experimental part of this study was derived.

I owe much to many at iThemba Labs but for sheer shortage of space I will limit myself to expressing my gratitude to Mr. Karl Springhorn for giving us the beam.

I wish to sincerely thank Mrs Justina Manyoma for encouraging me to return to school to obtaining my M.Sc.

I further wish to extent my grateful thanks to my course mates Mr. P. Simpemba and Mr. G. Kalonga for all constructive discussions we shared during the course work part of this study.

I owe a debt of gratitude to all the members of my family not only for their never ending support but for their understanding of my long periods away from them as well.

Finally, I would like to take this opportunity to express my heartfelt gratitude to my nephew Gift and my friends Evaristo, Mwiinga, Musonda, Mambwe and Winston for their continued support and encouragement. Only them know the depth of my indebtedness.

K.J.P.

Lusaka, Jul. 2010.

Contents

List of Figures

List of Tables

CHAPTER 1
INTRODUCTION

1.1 Background

Germanium and silicon are the best known elemental semiconductors and both belong to the same group in the Periodic Table. However, germanium (Ge) offers several attractive electro chemical properties over silicon (Si). Some of these properties include high saturated velocities of charge carriers of both polarities (electrons and holes) [1-4], very low carrier freeze-out temperatures and a better compatibility with high-k materials. The first of these properties is the most advantageous over Si for deeply scaled metal-oxide-semiconductor field effect transistors (MOSFETs) applications. In general, high performance complementary metal-oxide-semiconductor (CMOS) devices will require these germanium features, and they may replace the silicon supply in International Technology Roadmap for Semiconductors (ITRS). Germanium had been historically one of the most important semiconductors in the past as the first MOSFET and the integrated circuit (IC) were fabricated in Ge. The inferior properties of germanium dioxide (GeO_2) as compared to silicon dioxide (SiO_2) make this dielectric unsuitable for Ge MOSFET gate insulation and field isolation. This has not only obstructed very large scale integration (VLSI) realization in Ge for decades but it also made Ge to lose the race to Si as the semiconductor material of choice. The aggressive downscaling of devices is pushing the venerable SiO_2 to its performance limits since for ultrathin SiO_2 gate layers of typical thickness below 3 nm [5], the gate dielectric breaks down and charge carriers can flow through the gate dielectric by a quantum mechanical tunneling mechanism [6, 7]. Therefore, replacement of the SiO2 with higher permittivity (high-*k*) gate dielectrics [8] such as zirconia (ZrO_2) or hafnia (HfO_2) which enable high gate capacitance with physically thick insulators through which tunneling is low has been proposed. Moreover, high-*k* material based Ge MOSFETs with germanium oxynitride, zirconia and hafnia gate dielectrics have successfully been demonstrated [4, 9, 10]. These recent developments of replacing high-*k* materials over thermally grown SiO_2 as new gate dielectrics in CMOS devices have for consequence to eliminate one of silicon's technological advantages (its remarkable oxide no longer being used as a gate insulator) and also to overcome the major oxide drawback Ge initially faced. Consequently, the doors of Ge have

been reopened to the microelectronic agenda where it reappears as an appealing alternative semiconductor material and it is viewed as a possible replacement for Si. This has caused an extensive amount of renewed interest in understanding the structure, stability and physical properties of metal germanides during the last few decades. Metal germanides have great potential for applications in nano/microelectronics, opto-electronics and solid state detectors.

Before germanium can be adopted, a suitable material for making electrical contacts to the active areas of the germanium based devices must be identified. In analogy with the current Si-based technology where metal-silicides are used as contacts for the active areas of the devices, the use of metal-germanides is proposed for this purpose. Of all possible metal-germanides, nickel monogermanide (NiGe) and palladium monogermanide (PdGe) appear to be the most promising [10]. In order to successfully make use of nickel germanides in Ge-based devices it is essential to thoroughly understand all processes and mechanisms involved in germanium metallization as well as the properties of the phases formed. Identification of the dominant diffusing species (DDS) during formation of each phase, determination of the sequence of formation of the phases and temperatures at which the phases are formed during the germanidation process are among the important information required during fabrication. This is important for industrial applications as it can determine the heat treatment required to obtain a unique targeted phase with specific properties.

The choice of nickel (Ni) as the germanide forming precursor material is due to its low Curie temperature (360 ^{o}C), low thermal reaction temperature [10-14], and low consumption of substrate material [15].

1.2 Thermodynamics of Phase Formation

The thermodynamics of phase formation is one of the major interests of metal-semiconductor compound formation characteristics in the study of thin films. This deals primarily with the prediction of which of the many phases present in the equilibrium phase diagram forms first during solid state reactions and the phase formation sequence of subsequent phases.

Binary equilibrium phase diagrams usually display several equilibrium compound phases. They are a very important tool in the study of alloys because they define regions of stability of the phases that can occur in an alloy system under conditions of constant pressure (atmospheric) and

their significance was acknowledged by the first attempts [16- 18] at formulating phase prediction rules. Solid state reactions can be investigated in three different diffusion coupling regimes. The bulk diffusion couple and thin film diffusion couple regimes form the two extreme ends while the lateral diffusion couple regime forms the bridge between the two extreme regimes. The major difference between solid state reactions in bulk diffusion couple and thin film diffusion couple regimes is the presence of several and in some cases all the compound phases present on the phase diagram if sufficiently long time is allowed in the former regime while only one phase forms at a time in the latter regime. This led to an increased interest in predicting the phase compounds which would form first at interfaces in solids [11-31].

The formation of a compound phase can be discussed with the aid of a schematic diffusion couple arrangement like that shown in Fig. 1.1 which demonstrates as an example the reaction $xA + (1\text{-}x)B \rightarrow A_xB_{1-x}$. In this hypothetical conventional (i.e., with no marker) thin film diffusion couple formed of pure elemental components A and B as end members, a thermally induced compound phase A_xB_{1-x} is shown growing at the A/B interface. This schematic diffusion couple will also be used in subsequent sections and the other chapters to explain concepts related to phase formation.

In Fig. 1.1, the phase A_xB_{1-x} will continue to grow until one of the components (e.g. B) is completely consumed. If there is still A remaining at this stage, it will react with the A_xB_{1-x} phase to form a new more A-rich phase A_yB_{1-y} $(y > x)$. This will continue until either A or A_xB_{1-x} is completely consumed.

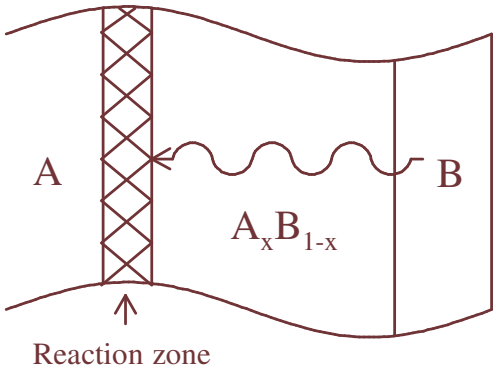

Figure 1.1: Schematic illustration of the formation of a compound phase A_xB_{1-x} at the reaction zone (or growth interface) in a conventional thin film diffusion couple. Atomic species B is assumed to be the dominant diffusing species.

Knowledge of the phase formation sequence is important from the standpoints of academic interest and material processing as it would enable the material scientist to control experimental parameters in a way that allows formation of specific phases with desirable properties.

1.2.1 Walser-Bené (W-B) Model

The Walser-Bené or W-B model [16], based on the argument that the initial condition of the interface consists essentially of a "metallic glass" of a concentration near the lowest-temperature eutectic in the binary system, was one of the earliest models that tackled the problem of first phase formation in thin film metal-silicon binary couples. The interest in first phase formation at metal-silicon planar interfaces was most probably due to their technological importance. The non-congruently melting phases are generally known to be skipped during phase formation in the metal-silicon systems [16, 17, 32]. Walser and Bené attributed this behavior to the higher energy barrier associated with the large rearrangement in short-range order (SRO) required to move from liquid like SRO to crystalline SRO for non-congruent states in contrast with the much smaller change in SRO associated with congruently melting states. They therefore expected the phase closest in concentration to the initial eutectic composition to nucleate. If two congruently melting phases existed on both sides of the eutectic the most stable compound, as indicated by the higher melting temperature, was expected to form.

On the basis of this model Walser and Bené [16] formulated the following rule for predicting first phase formation at the metal-silicon planar interfaces:

> *The first compound nucleated in planar binary reaction couples is the most stable congruently melting compound adjacent to the lowest-temperature eutectic in the bulk equilibrium phase diagram.*

Since this rule also applies to metal-germanium systems it was generalized as a metal-covalent rule for phase selection [17]. This rule was extended to metal-metal systems by relaxing the requirement that the first phase formed be congruently melting and it takes the following form [17]:

> *The first phase nucleated in metal-metal thin film reactions is the phase immediately adjacent to the lowest-temperature eutectic in the binary phase diagram.*

The main difference between the two rules is that the metal-covalent rule predicts "phase skipping" for non-congruently melting compounds [17] whereas the metal-metal rule does not make any reference to the stability of the compound in the event of the eutectic lying between two phases but predicts formation of the phase immediately adjacent to the lowest-temperature eutectic. Later Ronay [20] proposed a first phase formation rule taking into account the central eutectic, diffusing species, and interfacial free energy.

The metal-covalent rule predicted first phase formation with reasonable success and it was later extended by Tsuar et al. [33] to subsequent phase formation sequence as follows:

> *The second phase formed is the compound with the smallest ΔT that exists in the phase diagram between the composition of the first phase and the unreacted element.*

In this rule ΔT is defined as the temperature difference between the liquidus curve and the peritectic point and its value is equal to zero for congruently melting compounds. The peritectic point is the point where a solid breaks up into a liquid and a solid, both with new composition.

It is noteworthy that none of the rules considered so far make direct use of thermodynamic data and it was only after Pretorius [25-29] proposed the effective heat of formation concept that thermodynamic data could be used directly to predict first phase formation and the subsequent phase sequence.

1.2.2 Effective Heat of Formation (EHF) Model

The driving force for a process to take place is the change in free energy which is given by

$$\Delta G^o = \Delta H^o - T\Delta S^o \qquad (1.1)$$

where ΔH^0 is the change in enthalpy or heat of formation, ΔS^0 is the change in entropy and T is the absolute temperature. Since the change in entropy ΔS^0 is usually only about ±0.001kJ/deg per mole of atoms during solid state formation of compounds [34] the product $T\Delta S^0$ is usually negligibly small [29, 32] when compared with heats of formation ΔH^0 for most solid state reactions. Thus, ΔH^0 is a good measure of the change in free energy. That is, $\Delta G^0 \approx \Delta H^0$.

Equilibrium rules cannot be applied directly in these reactions because phase formation at an interface during solid state reaction is a dynamic non-equilibrium process.

The EHF model as proposed by Pretorius [25-31] has been successfully applied to metal-metal, metal-silicon and metal-germanium systems. This model is based on a modified heat of formation or effective heat of formation, $\Delta H'$, which is calculated as a function of the effective concentration of the elements at the reaction interface. Thus, the EHF model links standard thermodynamic concepts (heats of formation) with kinetics (effective concentration) and evaluates phase formation from a thermodynamic-kinetic point of view.

The fundamental concept of the EHF model is that it takes concentration into account and postulates that elements will mix and interact at the growth interface at an effective concentration which could differ significantly from the physical concentration at the growth interface. An effective heat of formation, $\Delta H'$, is then calculated as the maximum heat released per mole of available atoms during the formation of a specific compound at a particular effective concentration at the growth interface.

When calculating the effective heat of formation the concept of a limiting element becomes important. To understand this concept with reference to phase diagrams or specific examples, we refer to the schematic diffusion couple used in section 1.2 and consider the formation of a compound A_xB_{1-x} to take place at an effective concentration x' of element A at the growth interface. If $x' < x$ then the element A becomes the limiting element. The significance of the limiting element is that the effective concentration of the limiting element, x', and the concentration of the limiting element in the compound to be formed, x, dictate the amount of heat released per mole of available atoms. If the heat of formation of the compound phase A_xB_{1-x} is ΔH^0 with the concentration of the limiting element in the compound to be formed being x and the effective concentration of the limiting element is x' then the effective heat of formation can be calculated from

$$\Delta H' = \Delta H^o \times \left(\frac{\textit{effective concetration of limiting element}}{\textit{compound concentration of limiting element}} \right)$$

$$= \Delta H^o \times \left(\frac{x'}{x} \right) \qquad (1.2)$$

where $\Delta H'$ and ΔH^0 are expressed in units of kJ per mole of atoms. Since the effective concentration is always less than the compound concentration, it expresses the availability of the limiting element at the growth interface and excess atoms can be regarded as being available for the formation of the next increment of the compound at the moving interface.

Equation 1.2 shows a linear dependence of $\Delta H'$ on ΔH^0 and it can be used to calculate the effective heat of formation of any compound from the limiting element. Nevertheless, calculation of effective heat of formation from equation 1.2 in order to predict phase formation using the EHF requires knowledge of the effective concentrations of reacting species at the growth interface which cannot be calculated directly. The activation energy for solid state interdiffusion is known to be directly proportional to the melting point of the solid for a large variety of systems of a given structure and bond type [35]. The activation energy determines the mobility of the atomic species involved in a solid state reaction and it is found that smaller activation energies lead to greater mobilities [36]. Therefore, the greatest atomic mobility and hence the most effective mixing at the reaction interface is expected to be at the composition of the liquidus minimum which in many cases is the lowest temperature eutectic. The EHF rule for predicting phase formation in metal-metal systems states [27]:

> *The first phase to form during metal-metal interaction is the phase with the most negative effective heat of formation($\Delta H'$) at the concentration of the liquidus minimum of the binary system.*

While non-congruently melting phases are known to be skipped in metal-silicon systems because they do not nucleate readily [17, 18, 32], the effect of nucleation barriers is not taken into account in the calculation of EHF values. Thus, when formulating rules for phase prediction nucleation barriers must be considered and this is done by applying the restriction of congruency as was proposed for the W-B model. The corresponding EHF rule for predicting silicides and germanides formation states [26, 30, 31]:

> *The first compound phase to form during metal-silicon or metal-germanium interaction is the congruent phase with the most negative effective heat of formation ($\Delta H'$) at the concentration of the liquidus minimum of the binary system.*

From a chemical point of view Ge is more metallic than Si. As a result, germanide formation occupies a position between that of silicide formation where only congruent phases usually form first and metal-metal system phase formation in which the phase with the most negative $\Delta H'$ forms first regardless of the congruency [30, 31]. It is therefore not surprising that in the metal-germanium system it has been found that non-congruent germanide phases with a more negative $\Delta H'$ than the most negative $\Delta H'$ of the congruent phases, sometimes tend to form first [30, 31, 37- 39].

A general EHF rule for phase formation has recently been formulated [30] and it states:

> *Phases will react with each other to form a phase, with a composition lying between that of the interacting phases, whose effective heat of formation, calculated at the concentration closest to that of the liquidus minimum within this composition range, is the most negative.*

This general rule applies not only to phase formation but applies to phase formation sequence and phase decomposition as well.

1.3 Kinetics of Phase Formation

The rate at which a phase grows with time at the growth interface is another major interest in the study of thin film compound phase formation. This time-dependence of the rate at which the reaction or phase transformation occurs is what is meant by the term reaction kinetics. Compound phase formation during solid state reactions under steady state conditions can be divided into two broad categories [40]; the systems that exhibit laterally uniform growth with well-defined kinetics and temperature dependence, and those that show laterally non-uniform growth and exhibit critical temperature dependence.

In laterally uniformly growing systems the compound grows uniformly in a layer-by-layer mode and the reaction takes place in a relatively wide temperature range in a thermally activated manner far below any eutectic or melting temperatures of the system. This category can be further subdivided into two groups. In the first subgroup the compound thickness is proportional to the square root of the anneal time and the growth process is said to be diffusion limited or parabolic. The compound thickness in the second subgroup is proportional to the anneal time and the growth process is said to be interfacial reaction controlled. On the other hand, in the category

of laterally non-uniformly growing systems the compound growth occurs in a very narrow temperature range, usually within 10-30^{o}C [40]. Compound formation in this category is said to be nucleation controlled.

The growth of a new phase (A_xB_{1-x} for example) between a metal A and a semiconductor B requires three steps:

(1) The creation of a new interface;

(2) The diffusion of A (and /or B) through the new phase;

(3) The reaction of A and B at the interfaces to form the new phase [41].

At the beginning of the reaction, the thickness of the new phase is small so that A and B are always available at both interfaces. Therefore, the reaction is only limited by the reaction of A and B at the interface and the thickness of the new phase will increase linearly with time. Compound growth by this mode is said to follow interfacial-reaction controlled kinetics. As the thickness increases, the growth of the new phase becomes limited by the flux of atoms through the new phase to the growing interface(s). The growth of the new phase will be diffusion limited and will increase with the square root of time. This growth mode is said to follow diffusion controlled kinetics.

1.3.1 Diffusion Controlled Kinetics

A reaction is diffusion controlled when the rate of reaction is controlled by the rate of diffusion of one of the reactants through the solid product layer towards the interface where the reaction takes place. The diffusion controlled process follows a parabolic or quadratic growth law and is characterized by the transport of material through the growing compound to the reaction zone as illustrated in Fig. 1.1. The growth rate slows down as the compound grows thicker because the diffusion path becomes longer.

The growth kinetics are described by the following phenomenological relation

$$x^2 - x_0^2 = D(t - t_0) \tag{1.3}$$

where D is the diffusivity or interdiffusion coefficient, x and x_0 are the compound thicknesses at time t and t_0 respectively. The diffusivity is sometimes referred to as diffusion constant because it does not depend on time but it depends on temperature as equation 1.4 indicates. The

temperature dependence of the interdiffusion coefficient D has been found to follow, in most cases, the Arrhenius law

$$D = D_0 \exp\left[-\frac{H_a}{k_B T}\right] \tag{1.4}$$

where D_0 and H_a are called the frequency factor (or temperature-independent pre-exponential (m^2/s)) and activation enthalpy (or energy if $H_a \approx E_a$, where E_a is the activation energy (J/mol or eV/atom)) respectively, k_B is the Boltzmann constant (8.617385×10^{-5}eV/K) and T the absolute temperature.

The in situ, real-time Rutherford backscattering spectrometry (RBS) allows the growth kinetics of a system to be quickly and conveniently analyzed by linear temperature ramping. In this technique the heater is programmed in such a way that the sample is subjected to a linear ramped thermal anneal in the scattering chamber while the RBS spectra are continuously acquired. In this way, it is possible to observe all the phases formed in a system and to determine the growth kinetics from a single sample in one experimental run. This is in drastic contrast with conventional isothermal annealing where many samples have to be prepared and annealed separately in order to obtain similar parameters.

If the constant temperature ramp rate is dt/dT and the compound is assumed not have grown to a measurable thickness at time t_0 (i.e., assuming that $x_0 = 0$ at $t = t_0$), then equation 1.3 can be written as

$$x^2 = \int_{t_0}^{t} D dt = \int_{T_0}^{T} D \frac{dt}{dT} dT \,. \tag{1.5}$$

Substituting equation 1.4 into equation 1.5 leads to

$$x^2 = \int_{T_0}^{T} D_0 \frac{dt}{dT} e^{-\frac{H_a}{k_B T}} dT = D_0 \frac{dt}{dT} \int_{T_0}^{T} e^{-\frac{H_a}{k_B T}} dT \,. \tag{1.6}$$

Integration of equation 1.6 yields

$$x^2 = D_0 \frac{dt}{dT} \frac{k_B T^2}{H_a} e^{-\frac{H_a}{k_B T}} - D_0 \frac{dt}{dT} \frac{k_B T_0^2}{H_a} e^{-\frac{H_a}{k_B T}} \,. \tag{1.7}$$

At $t = 0$ the temperature is typically very low and no reaction can be considered to occur so that T_0 can be approximately taken to be equal to zero. With this assumption equation 1.7 then reduces to

$$x^2 = D_0 \frac{dt}{dT} \frac{k_B T^2}{H_a} e^{-\frac{H_a}{k_B T}} . \qquad (1.8)$$

Dividing equation 1.8 through by T^2 and taking natural logarithms of both sides gives

$$In\left(\frac{x^2}{T^2}\right) = -\frac{H_a}{k_B T} + In\left(D_0 \frac{dt}{dT} \frac{k_B}{H_a}\right). \qquad (1.9)$$

A plot of $In(x^2/T^2)$ versus $1/k_B T$ yields a straight line whose slope gives the activation enthalpy (or energy if $H_a \approx E_a$).

It must be emphasized that when the compound under consideration has already grown to a measurable thickness at the initial temperature T_0, then the last term on the right hand side of equation 1.7 must be taken into account.

In practice the growth kinetics can be determined directly from the plot of either the thickness or the square of the thickness against time. If a plot of the square of thickness against time yields a straight line then the growth is diffusion limited otherwise it is interfacial reaction limited.

1.3.2 Interfacial-Reaction Controlled Kinetics

The interfacial-reaction controlled process is said to follow a linear growth law and the growth kinetics in this case can be described by the relation

$$x - x_0 = K(t - t_0) \qquad (1.10)$$

where K given by

$$K = K_0 e^{-\frac{H_a}{k_B T}} \qquad (1.11)$$

is the interfacial-reaction constant and K_0 is a pre-exponential.

Applying the same arguments employed for the diffusion limited kinetics, an equation similar to equation 1.9 can be written as

$$In\left(\frac{x}{T^2}\right) = -\frac{H_a}{k_B T} + In\left(K_0 \frac{dt}{dT}\frac{k_B}{H_a}\right). \qquad (1.12)$$

The activation energy can be obtained from the slope of $\ln(x/T^2)$ versus $1/k_B T$. If a plot of x against time yields a straight line then the growth is interfacial-reaction controlled otherwise it is diffusion limited. If none of these plots yield a straight line then the reaction is nucleation limited.

1.3.3 Nucleation Controlled Kinetics

Let us now assume that the schematic diffusion couple formed of pure elemental components A and B, similar to the one used in section 1.2, is annealed at a certain temperature. The applied thermal energy causes the two phases A and B to react across their planar interface to form a third phase A_xB_{1-x}. The driving force for the reaction is the change in free energy ΔG upon the formation of A_xB_{1-x}. In this process the system evolves from a system with only one interface A/B to a system with two interfaces A/A_xB_{1-x} and A_xB_{1-x}/B. The creation of this extra interface means that the formation of A_xB_{1-x} will generally be accompanied by an increase in the surface energy $\Delta\sigma$. The classical nucleation theory mandates that the initial process in the formation of A_xB_{1-x} should be a nucleation process with an activation energy ΔG^* given by the relation

$$\Delta G^* \propto \frac{\Delta\sigma^3}{\Delta G^2} \ . \qquad (1.13)$$

An excellent derivation of relation 1.13 is given by Johan Seger [42]. Quite often the value of ΔG^* is so small that nucleation effects are not significant as a rate limiting factor. However, examination of relation 1.13 reveals that for sufficiently small ΔG, the value of ΔG^* can reach such a magnitude that nucleation occurs at high temperatures and with such high diffusion coefficients that the contrary becomes true; diffusion ceases to be significant as a rate limiting

mechanism. Under such conditions the reaction then assumes a nearly explosive character [43] which is manifested in the narrow growth temperature window mentioned earlier.

A study of such nucleation effects contains a number of observations, some of which are predictive in nature such as:

(1) Nucleation effects can generally be anticipated to become predominant when two reacting phases A_xB_{1-x} and A_yB_{1-y} are close in composition [44];

(2) When two elemental components A and B enter into reaction, nucleation can prevent the formation of some phases at low temperature, even if these phases are stable and are duly found in equilibrium phase diagrams [44];

(3) The effective heat of formation is generally close to zero for a nucleation reaction.

1.4 General Considerations of Diffusion Theory

Diffusion is generally present in many dynamical processes in nature and exists in all forms of matter. However, atomic diffusion in solids is much slower than that in gases and liquids. The diffusion process is more pronounced at elevated temperatures but in many cases it occurs even at ambient temperatures depending on the systems involved. Solid-state atomic diffusion is a very important phenomenon which controls atomic redistribution and phase transformation during industrial fabrication. In metallurgy many processes such as homogenization, precipitation, re-crystallization, oxidation, sintering, et cetera are controlled by diffusion. Understanding and controlling diffusion is of great importance in many branches of science and technology.

Roberts and Austen can be claimed to have initiated the study of solid state diffusion about 100 years ago when they discovered the diffusion phenomenon of gold in solid lead in 1896 [45]. Although many diffusion studies were conducted in the 1930's [46], the invention of the transistor in 1948 [47] by Bardeen, Brattain, and Schockley was one of the factors which boosted research in solid state diffusion. The formation of silicides and germanides for use as contact and interconnect material is usually reported to follow a diffusion controlled growth [48, 49]. However, there are exceptions like $NiSi_2$ growth which is nucleation limited [22]. The detrimental effect on the performance of devices resulting from overgrowth and bridging that occurs when the substrate element (Si or Ge) is the dominant diffusing species during device

manufacture, the need for controllable doping of semiconductors, etc., are only a few examples of the processes that require knowledge of atomic diffusion and their coupling with defects which act as diffusion vehicles during solid state reactions.

Atomic diffusion was for a long time believed to occur by a direct exchange mechanism or Zener ring mechanism as shown in Fig. 1.2 (a) and (b) respectively. These mechanisms indicate the equality of diffusion of binary elements in metals and alloy crystals. This was the case until 1947 when Ernest Kirkendall reported the results of experiments on the interdiffusion of copper and zinc in brass in which he observed the movement of the interface between the different phases due to high-temperature interdiffusion [50]. This phenomenon, now called the Kirkendall effect, supported the idea that atomic diffusion occurs through vacancy exchange. This is illustrated in Fig. 1.2 (c). The discovery of the Kirkendall effect is yet another factor that contributed to the significant development of defect and diffusion studies.

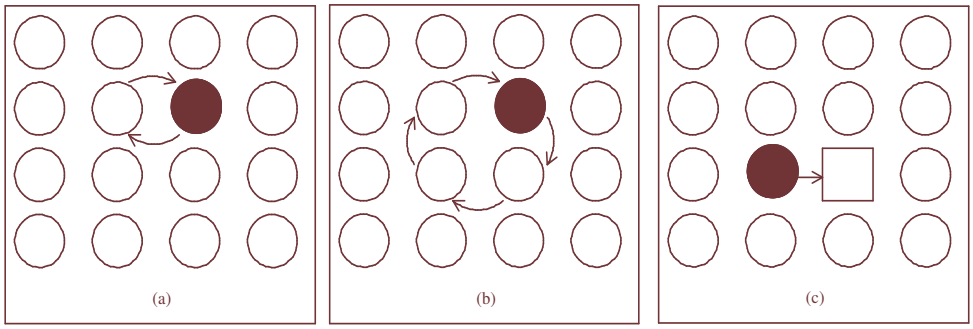

Figure 1.2: The atomic diffusion mechanisms showing (a) a direct exchange mechanism, (b) Zener ring mechanism, and (c) vacancy mechanism.

Diffusion is the process by which particles redistribute themselves as a result of random (Brownian) motion. Random motion requires no driving force of any kind. When considering diffusion it is important to distinguish between diffusion which occurs in homogeneous materials and net diffusion which occurs in inhomogeneous materials. Diffusion is hard to detect in a homogeneous material because atoms move randomly and there will be an equal number of atoms moving in one direction or the other. In an inhomogeneous material such as a diffusion couple, the effect of diffusion is readily seen by a change of concentration with time. In this case

there is a net diffusion because although all atoms are moving randomly there are more atoms of one type moving from a region where their concentration is higher.

The flux of diffusing atoms, *J*, is used to quantify how fast diffusion occurs. The flux is defined as either the number of atoms diffusing through a unit area per unit time (atoms/m^2-second) or the mass of atoms diffusing through a unit area per unit time (kg/m^2-second) because of a concentration gradient. Under steady state conditions the flux does not change with time and it is given by the equation proposed by Adolf Fick [51], known as Fick's first law

$$J(x,t) = -D\left(\frac{\partial C(x,t)}{\partial x}\right) \tag{1.14}$$

where D is the interdiffusion coefficient (or often referred to as diffusivity) as defined earlier in equation 1.4, x is the position parameter, $C(x, t)$ is concentration of the moving atoms and $\partial C(x,t)/\partial x$ is the concentration gradient which is often considered to be the driving force in diffusion although it is not a force in a mechanistic sense. D is a constant because it does not depend on time, but it depends on temperature (see equation. 1.4). The negative sign in equation 1.14 stems from the fact that diffusion occurs in the direction opposite to that of increasing concentration.

If the composition (of flux) changes with time, the time-dependence of concentration is given by Fick's second law which is derived from Fick's first law and the law of mass conservation as

$$\frac{\partial C}{\partial t} = -\frac{\partial J}{\partial x} = \frac{\partial}{\partial x}\left(D\frac{\partial C}{\partial x}\right). \tag{1.15}$$

If D is not a function of position or composition, equation 1.15 reduces to

$$\frac{\partial C}{\partial t} = D\left(\frac{\partial^2 C}{\partial x^2}\right). \tag{1.16}$$

Equation 1.16 is called the concentration independent diffusion equation and it can sometimes be solved analytically.

It is evident from the experiments conducted in the early 20th century that the diffusion coefficients in solid state reaction are not constant but are a function of composition and temperature [52, 53]. The diffusivity D is said to be concentration dependent in extrinsically doped semiconductors [54].

When D is a function of composition, which in turn is a function of x, Fick's second law can be written as

$$\frac{\partial C}{\partial t} = \frac{\partial}{\partial x}\left(D(x)\frac{\partial C}{\partial x} \right) = \frac{\partial D(x)}{\partial x}\frac{\partial C}{\partial x} + D(x)\frac{\partial^2 C}{\partial x^2}. \qquad (1.17)$$

The term $\partial D(x)/\partial x$ makes equation 1.17 inhomogeneous and the solution in a closed form is not possible.

In a hypothetical conventional thin film diffusion couple formed of pure elemental components A and B such as the one introduced in section 1.2, diffusion is responsible for the thermally induced solid state reaction which leads to the formation of new phases between the two pure elements. The nature of the phase formed depends on the strength of the bonds developed between the type A and type B atoms as illustrated in Fig. 1.3. When the A-B bond is intermediate in strength between the bonds of the A-A and the B-B atoms, a solid solution is formed and the atoms of both A and B occupy random positions in the crystal. This situation is illustrated in Fig. 1.3 (a). A eutectic is formed when the A-B bond is weaker than the A-A and the B-B bonds. In this case each component element has a low solubility in the other element, which is the solid equivalent of the water-oil mixture.

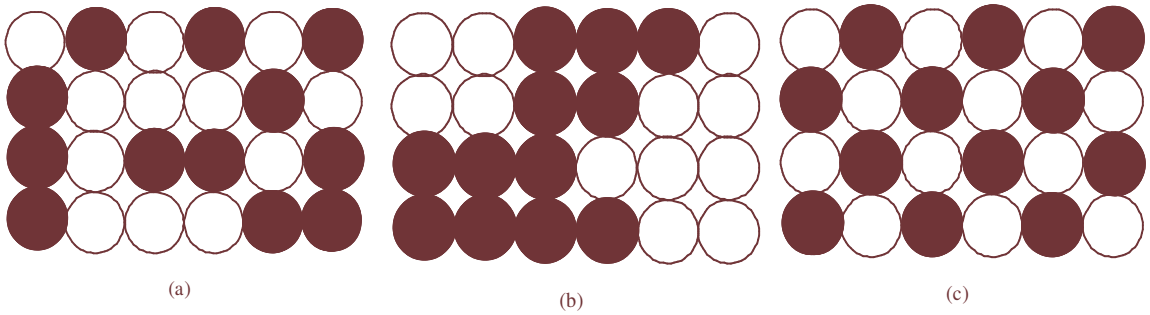

Figure 1.3: Schematic illustration of differing configurations of A and B atoms in a binary A-B alloy: (a) Solid solution, (b) segregation in a eutectic and (c) compound formation.

The arrangement of atoms of each type in a eutectic is depicted in Fig. 1.3 (b). A compound is formed when the A-B bond is stronger than the A-A and B-B bonds which is the situation shown in Fig. 1.3 (c).

In order to understand the physics of diffusion, it is helpful to examine the underlying microscopic mechanisms more closely. All atoms vibrate constantly about their lattice positions when the temperature is above absolute zero. The atoms vibrate with a distribution of frequencies and amplitudes (i.e., there is a distribution of vibrational energies). The vibrational energy of a particular atom varies over time and as temperature increases its average vibrational energy also increases.

Diffusion is the movement of an atom from one lattice position to another (i.e., diffusion is material transport by atomic motion). Active diffusion of an atom can occur if there is an adjacent space and if the temperature is high enough for an atom to have sufficient energy required to overcome the energy barriers to atomic motion. In order to jump from one lattice site to another, atoms need energy to break bonds with neighbors and to cause the necessary lattice distortions during the jump. This energy comes from the thermal energy of atomic vibrations ($E_{av} \sim k_B T$ where E_{av} is the average thermal energy of the atoms and k_B and T are as defined in section 3.2.1).

Two types of diffusion can be distinguished, namely, self-diffusion and interdiffusion (or impurity diffusion). Self-diffusion is diffusion in a one-component material, when all toms that exchange positions are of the same type. On the hand, interdiffusion (or impurity diffusion) is diffusion that occurs in response to a concentration gradient. The rate of diffusion is influenced by such factors as temperature, diffusion mechanism, microstructure as well as diffusing and host species. The rate of diffusion increases very rapidly with increasing temperature. As will be explained later, diffusion occurs faster via some mechanisms than others. For example, diffusion by interstitial mechanism is usually faster than by vacancy mechanism. It will also be explained later that diffusion is faster in polycrystalline materials than in single crystals due to the accelerated diffusion along grain boundaries. In general the diffusivity is greater through less restrictive structural regions such as grain boundaries, dislocation cores, and external surfaces. The pre-exponential factor (D_0) and activation energy for diffusion (E_a) are different for each solute-solvent pair which affects the rate at which either the solute or solvent diffuses. Table 1.1 lists some of the dependences of diffusion rate on the structure of the material.

Atomic movements suggested to be responsible for the diffusion process in a crystal can be classified into two categories, those involving the motion of one atom at a time and those

involving cooperative movement of two or more atoms at a time. The former category includes interstitial, interstitialcy, vacancy, kick-out and dissociative mechanisms while the latter includes direct interchange and Zener ring mechanisms.

Table 1.1: Some dependences of diffusion rate on the structure of the material.

Diffusion is faster for …	Diffusion is slower for …
1. open crystal structures	close-packed structures
2. lower melting temperature materials	higher melting temperature materials
3. materials with secondary bonding	materials with covalent bonding
4. smaller diffusing atoms	larger diffusing atoms
5. cations	anions
6. lower density materials	higher density materials

These diffusion mechanisms, some of which are already illustrated in Fig. 1.2, are briefly discussed below.

1.4.1 Vacancy Diffusion Mechanism

A vacancy is the absence of an atom from its normal location in a perfect crystal structure. The vacancy mechanism is the best-known and most common diffusion mechanism. This diffusion mechanism is illustrated in Fig. 1.4.

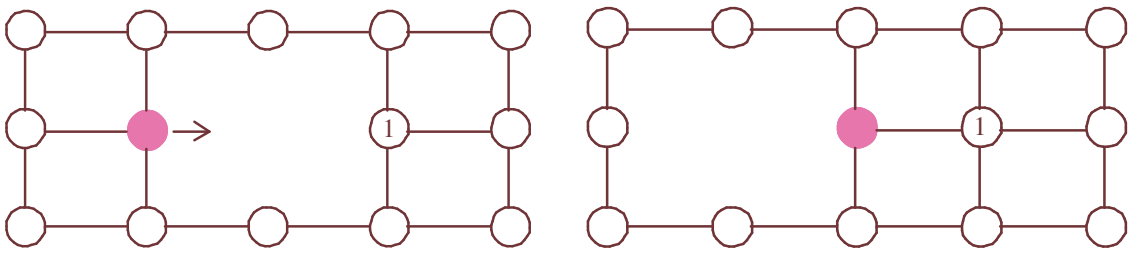

Figure 1.4: Vacancy diffusion mechanism.

At any temperature above absolute zero a crystal will have a finite concentration of vacancies given by

$$N_v = \exp\left(-\frac{\Delta G_v}{RT}\right), \tag{1.18}$$

where N_v is the mole fraction of vacancies, ΔG_v is the free energy of formation, T is the absolute temperature, and R is the gas constant [55]. Since at any temperature above absolute zero all the atoms are in a state of constant vibratory motion, it is possible for the shaded atom in Fig. 1.4 to move to the right by exchanging places with the vacancy. The direction of flow of atoms is opposite to the vacancy flow direction. Since vacancies also move through the crystal by the same mechanism, a subsequent vacancy may appear at site 1 and the shaded atom moves further to the right. In this way the resident atom is able to move through the crystal.

This mechanism will be dominant in self diffusion in which the diffusing atoms are of the same type. If the diffusing atoms are of different types with one atomic species larger than the other, then interstitial diffusion becomes the most likely diffusion mechanism.

1.4.2 The Interstitial Diffusion Mechanism

Interstitial diffusion is the simplest diffusion mechanism in semiconductors in which the diffusant hops from one interstitial site (or space between lattice atoms) to another. Diffusion via the interstitial mechanism is usually characteristic of very small atoms moving in the voids between larger host lattice atoms (i.e, it requires small impurity atoms that can fit into interstices of the host atoms) as illustrated in Fig. 1.5.

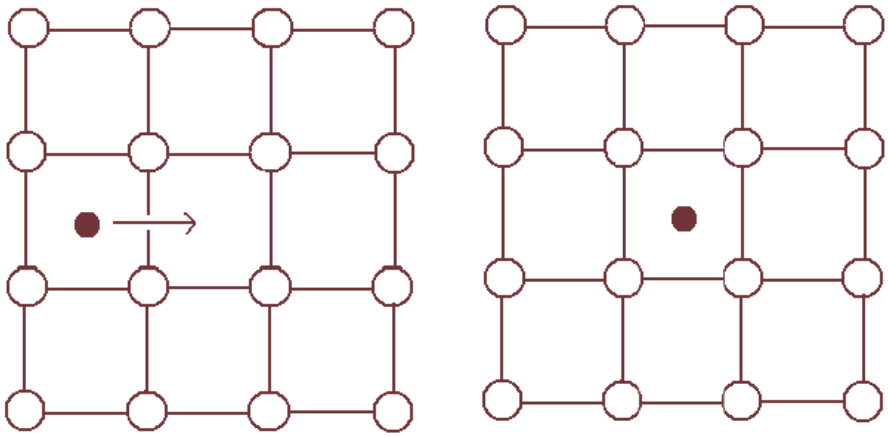

Figure 1.5: Schematic illustration of the interstitial diffusion mechanism.

Interstitial diffusion is typically very fast because interstitial (impurity) atoms are smaller and hence more mobile. The other reason why interstitial diffusion is fast is that interstitial atoms are virtually always surrounded by empty interstitial sites and so they do not have to wait for an adjacent site to fall empty. Diffusion of interstitials is typically faster as compared to the vacancy diffusion mechanism (self-diffusion or diffusion of substitutional atoms) because the bonding of interstitials to the surrounding atoms is normally weaker and there are many more interstitial sites than vacancy sites to jump to.

The jumping of impurity atoms from one interstitial site (or interstice) to another is inhibited by the host atom because the motion of impurity atoms distorts the host atoms. This distortion of host atoms constitutes a barrier to the motion of the interstitial atoms and the situation implies some sort of energy barrier.

This mechanism will be dominant in any non-metallic solid in which the diffusing interstitial atom does not distort the lattice too much. However, if the diffusing interstitial atom is not much smaller than the resident atoms then the distortion involved becomes too large and another diffusion mechanism such as interstitialcy diffusion mechanism becomes more likely.

1.4.3 The Indirect Interstitial or Interstitialcy Diffusion Mechanism

The interstitialcy mechanism, which is a variant of the interstitial mechanism, is often referred to as the interstitial mediated mechanism. In this mechanism the migration occurs by an interstitial atom moving onto a normal lattice site whilst simultaneously the original lattice atom moves into an interstitial position. It is similar to the interstitial diffusion mechanism because both involve dissolution of interstitial sites. The difference between the two mechanisms is that in interstitialcy diffusion the diffusing interstitial atom is not much smaller than the host atom which makes it difficult for it to push its way directly through to the next interstitial site. In this mechanism the diffusion maneuver is executed in two steps rather than in a single step. This mechanism is illustrated in Fig. 1.6. Instead of moving to adjacent interstitial sites such as those labeled as A and C in Fig. 1.6 (a), the interstitial atom originally at site 1 pushes the resident (host or substitutional) atom from site 4 to site B and then takes up its position.

This two step maneuver is easier from energy considerations than moving directly to an adjacent site because the distance between atoms at sites 5 and 6 is longer than either the distance

between atoms at sites 3 and 4 or atoms at sites 2 and 4. Therefore, less energy is expended in first pushing the host atom to site B than moving directly into an adjacent interstitial site A or C. Fig. 1.6 (b) illustrates the subsequent positions of the interstitial (or substitutional) atoms.

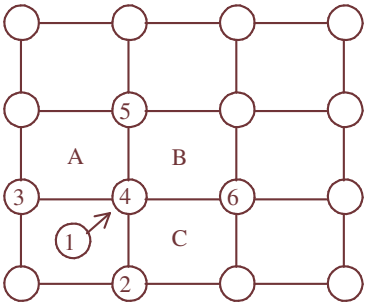

(a)

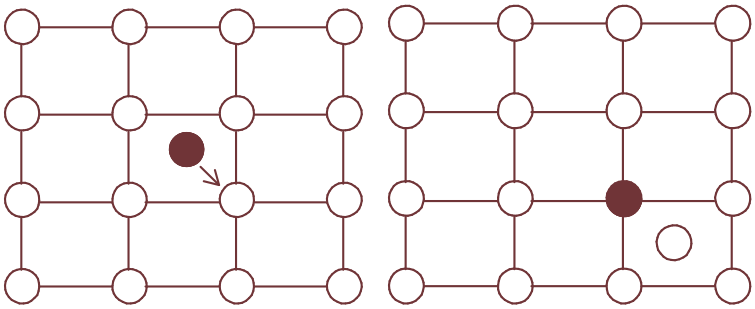

(b)

Figure 1.6: Schematic illustration of (a) two step diffusion maneuver, and (b) subsequent positions of the interstitial atom in interstitialcy diffusion mechanism.

When an atom can occupy both the host (substitutional) and the interstitial sites, then it is possible for the diffusion of this atom to proceed via the kick-out or substitutional-interstitial (dissociative) mechanisms.

1.4.4 Substitutional-Interstitial or Dissociative Diffusion Mechanism

This is one of the most extensively investigated mechanisms because it is believed to occur in a number of technologically important semiconductor systems. It is one of the interesting examples of two diffusion mechanisms operating together. In this mode of diffusion (also known

as the Frank-Turnbull mechanism [56]) the lattice type change occurs via interaction with vacancies.

In a typical sequence, a substitutional site atom (resident or host atom) can dissociate to an interstitial site atom and a vacancy (formation of a Frenkel pair). In the interstitial state the atom diffuses through the lattice very fast until it finds a vacancy. It then rejoins the lattice (substitutional site) by recombining with a vacancy.

1.4.5 Kick-out Diffusion Mechanism

The reaction with defects in the kick-out diffusion mechanism is exactly the same as in the interstitialcy diffusion mechanism because the change in lattice sites in both mechanisms occurs by kicking between substitutional atoms and interstitial atoms. The main difference is that in the kick-out mechanism an atom in the interstitial state can diffuse long distances via the direct interstitial mechanism before it is kicked back into the substitutional position.

1.4.6 Direct Exchange Diffusion Mechanism

This is the simplest conceivable cooperative movement of atoms. As illustrated in Fig. 1.2 (a), in this diffusion mode two atoms jump past each other and exchange positions. It has the attractive property of not requiring the presence of defects for it to operate but this involves the outward displacement of the atoms surrounding the jumping pair during the jumping period which would cause large lattice distortion and consequently its occurrence is unlikely. Glazmann et al. [57] have proposed that the self-diffusion of silicon proceeds by this mechanism. The so-called fourfold coordinated defect (FFCD) has recently been suggested as the diffusion vehicle for silicon, where the diffusion jump can occur by the swing of a special two-atom defect [58].

1.4.7 Zener Ring Diffusion Mechanism

This is the diffusion mechanism illustrated in Fig. 1.2 (b). In this mechanism thermal vibrations are assumed to be sufficient to cause a number of atoms, which form a natural ring in a crystal, to jump simultaneously and in synchronism in such a manner that each atom in the ring advances one position around the ring. This mechanism is not as likely as the substitutional or interstitial mechanisms.

No experimental evidence so far has been found to support this mechanism and the direct exchange mechanism.

1.4.8 Grain Boundary and Free Surface Diffusion Mechanism

The movement of atoms in solids is not restricted to the interiors of crystals. It is well known that diffusion processes also occur on the surfaces and along the boundaries of crystals. A grain boundary can be defined as the interfacial transition region between two grains in a single phase material, which are in contact with each other but differ in crystallographic orientation [59]. Grain boundary diffusion is the process of atomic transport along grain boundaries in polycrystalline materials. Sufficient evidence has been accumulated [60] to conclude that diffusion is more rapid along grain boundaries than in the interiors of crystals, and that free-surface diffusion rates are larger than either of the other two. These observations can be understood on the basis of the progressively more open structure found on exterior surfaces and at grain boundaries. It is quite reasonable that atoms should move most easily on free surfaces, with more difficulty in grain boundary regions and least easily in the interior of crystals. Since grain boundaries are highly disordered, it could be suggested that they provide a more "open" medium for diffusion compared with the other mechanisms considered earlier. Therefore, it would be reasonable to expect the values of activation energy for diffusion along grain boundaries to be smaller in general.

As the density of grain boundaries is particularly high in polycrystalline thin films, grain boundary diffusion could be the most dominant transport mechanism in these structures at relatively low temperatures.

1.5 The Ni-Ge Binary System

Bulk metal-germanium binary systems are relatively well characterized [61, 62] but the reaction of thin metal films with germanium has received less attention [63-84]. The Ni-Ge system is one of the binary systems whose reaction pathway is still plagued by misunderstanding especially regarding the first phase formed during the solid-state reaction of thin nickel films with germanium. The binary equilibrium phase diagram of the Ni-Ge system is presented in Fig. 1.7 [85].

The binary equilibrium phase diagram of this system shows nine phases of which four are thermodynamically stable at room temperature: cubic β-Ni_3Ge, orthorhombic Ni_2Ge, monoclinic Ni_5Ge_3 and orthorhombic NiGe whereas five others are only stable at elevated temperatures: hexagonal Ni_5Ge_2, hexagonal Ni_5Ge_3, orthorhombic $Ni_{19}Ge_{12}$, hexagonal Ni_3Ge_2, and γ-Ni_3Ge [71].

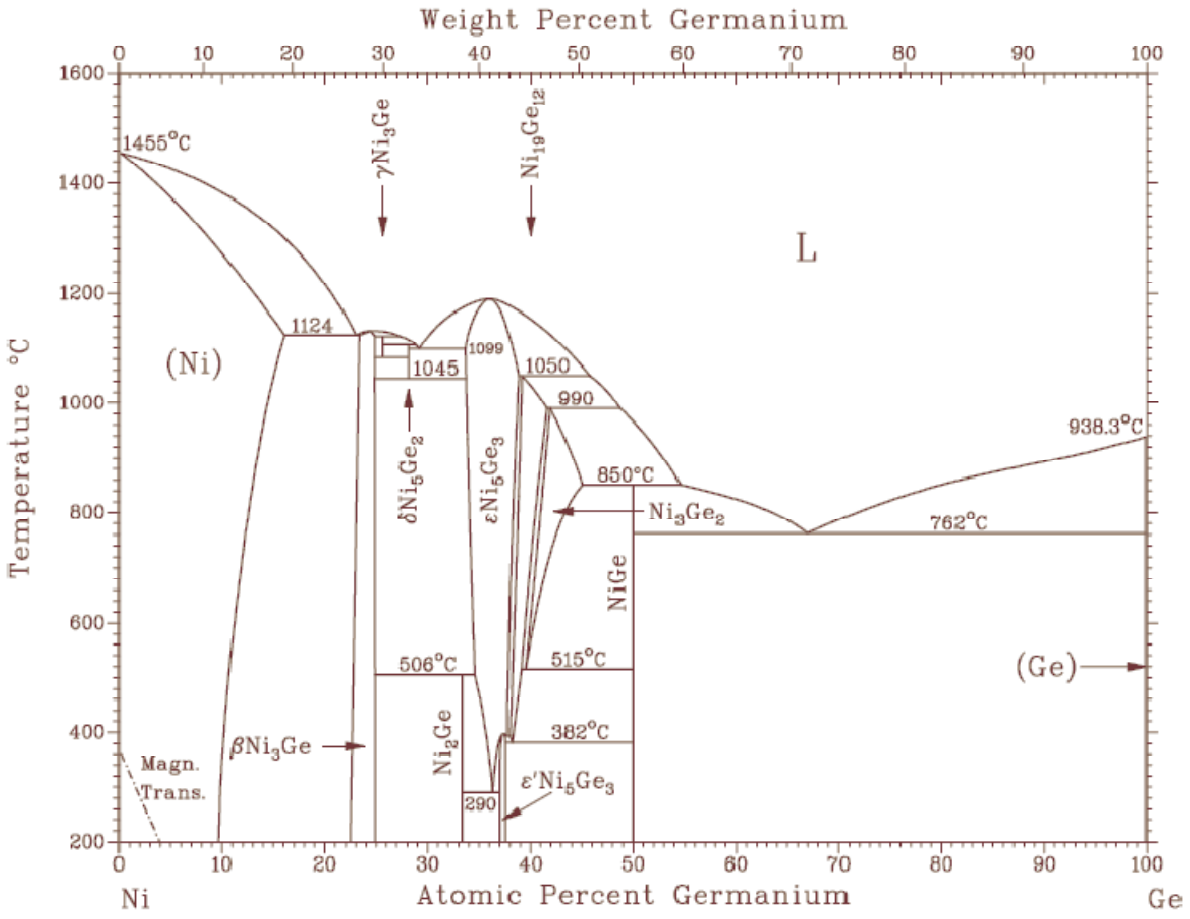

Figure 1.7: Phase diagram of the Ni-Ge system courtesy of [85].

In both Ni-Si and Ni-Ge thin film systems only some compounds from the equilibrium phase diagram are found to appear during solid state reactions. For the Ni-Si system the phase formation sequence generally accepted is, Ni_2Si, NiSi and $NiSi_2$ although recent studies have reported transient phases [86, 87] while only two phases are usually reported for the nickel germanides.

The available reports agree on the second and final phase, NiGe, but disagree on the first phase. Table 1.2 summarizes the phase formation sequences and their typical formation temperatures as reported by different researchers.

Table 1.2: Some the observed phase formation sequence and the typical formation temperature of these phases in the Ni-Ge system reported in literature

No	First phase		Second phase		Reference
	Observed phase	Typical formation temperature (^oC)	Observed phase	Typical formation temperature (^oC)	
1	Ni_2Ge	≈ 250 160 150-300	NiGe	260-600 250 250-600	Marshal et al. [67] Hsieh et al. [13] Wittmer et al. [80]
2	Ni_3Ge_2	-	NiGe	-	Jin et al. [55][a]
3	Ni_5Ge_3	- - -	NiGe	- 150 200–300	Gaudet et al. [10, 79][b] Nemouchi et al. [71, 72, 83][c] Patterson et al. [81]
4	Ni_5Ge_3/ Ni_2Ge	250/300	NiGe	350	Mueller et al. [66][d]

[a]Formed by rapid thermal annealing (RTA) at 400 ^oC. [b]The phases appeared consecutively on Ge(111) while they grew simultaneously on α-Ge and Ge(001). The first phase on Ge(111) was observed near an annealing temperature of 170 ^oC and was identified to Ni_5Ge_3 although they did not rule out Ni_2Ge. [c]The simultaneous growth of the two phases is also reported with formation of NiGe being observed to have occurred during deposition at room temperature. [d]The metal-rich phases formed below 350 ^oC but starting with this temperature the monogermanide dominated.

While the more common Ni phases, Ni_5Ge_2, Ni_5Ge_3, Ni_2Ge and NiGe are established in literature, the $Ni_{19}Ge_{12}$ phase has only been reported by Ellner et al. [88]. Although the binary equilibrium phase diagram of the Ni-Ge system indicates the presence of only 9 phases, a new nickel germanide, $NiGe_2$, has recently been synthesized under high pressure and temperature conditions [68]. In bulk diffusion couples simultaneous growth of phases present in the binary equilibrium phase diagram is possible. However, compound formation in the thin film diffusion couple regime is known to be sequential in which one phase grows at a time before another phase can begin to grow. In stark contrast with the usual sequential growth reported in thin films,

simultaneous growth of Ni_5Ge_3 and NiGe has been reported on amorphous and polycrystalline germanium in a reaction between nickel films and germanium [10, 71, 72].

1.6 Scope of the Thesis

The purpose of the present study is to obtain and extend the basic understanding of the solid phase interaction between germanium and nickel in the thin film diffusion couple regime. Although silicon is the main semiconductor material in the electronic industry, the aggressive down scaling of microelectronic devices to ever smaller dimensions and ever better performance has pushed the Si based materials to its physical limits. Germanium is considered to be a possible replacement for silicon because it offers a lot of attractive electrochemical properties. Clear understanding and knowledge of the phase formation characteristics of metal germanides such as nickel germanides which hold a lot of promise for the microelectronic and opto-electronic industry therefore becomes very important for device fabrication. The aim of this investigation is to determine the germanide formation characteristics in the Ni-Ge binary system. Thus, the study focuses on the growth characteristics of nickel germanides which involves the determination of phase formation temperature, phase formation sequence, activation energy for the solid state diffusional growth and identification of the dominant diffusing species during the formation of each phase.

The Ni-Ge binary system contains 9 phases as can be seen from the binary equilibrium phase diagram in Fig. 1.7. A review of some of the experimental results published by other researchers was summarized in Table 1.2. Examination of the results given in that table reveals at once the confusion regarding the first phase that forms in the Ni-Ge system and to some extent the temperature of formation of the observed phases. It is hoped that this study will contribute to the body of knowledge and literature that will eventually clear this misunderstanding.

Chapter 2 focuses mainly on the explanation of experimental procedures used in this investigation. A description of the sample preparation procedures, an explanation of the data acquisition and sample characterization techniques are presented. In this study we report the use of in situ real-time RBS technique in a random geometry to study solid state reactions between thin nickel films and the <100>-oriented Ge substrate. The literature surveyed showed that the Ni-Ge system has never been investigated using the in situ real-time Rutherford Backscattering

Spectrometry (RBS) method. In this chapter the mathematical formalism of the fundamental concepts on which the RBS technique is based are also presented. Chapter 2 ends with a description of the marker technique as a tool for monitoring the direction of atomic mobility.

The main findings of this investigation are presented in chapter 3. The results are detailed, discussed and elaborated upon in this chapter.

Finally, in chapter 4 a summary of the important results obtained in this study is presented. Various conclusions and discussions of the nickel-germanium system with some suggestions for future work in this field are also presented.

CHAPTER 2
EXPERIMENTAL METHODS

2.1 Sample Preparation and Processing

2.1.1 Substrate Preparation and Cleaning

The samples were prepared on <100>-oriented single crystal germanium substrates of thicknesses that were effectively infinite. The substrates were first degreased by sequential ultrasonic washing for 5 minutes in acetone and 5 minutes in ethanol. The degreasing is necessary to remove any hydrocarbons which would prevent the hydrofluoric acid (HF) from removing the germanium oxide. They were then rinsed in a deionised water solution with a resistivity of better than 10 MΩ.cm. The resistivity is just a measure of the purity of the water. As metal ions reduce the resistivity, if the resistivity is too low we could leave traces of metal on the sample.

The cleaning process was completed by etching the substrates in a dilute HF solution (1:20) for 30 seconds to remove the native oxide and passivate the surface with hydrogen. Passivating the substrate with hydrogen rather than with oxygen has the advantage that the hydrogen is readily desorbed at lower temperatures than are required to remove the passivating oxide. Finally, the substrates were rinsed in deionised water. This process was repeated until the substrates were completely hydrophobic after which they were blown dry with filtered nitrogen.

The substrates were then mounted on aluminum holders and immediately loaded into an electron-beam evaporation system. The important features of the vacuum system used for electron beam evaporation of thin films are shown in Fig. 2.1.

2.1.2 Vacuum Deposition System

The evaporator has three crucibles into which elements to be evaporated are loaded. The position of the crucibles can be moved from the outside so that each of the three crucibles can be placed in the path of the electron beam in turn. The electron beam supplies heat to the crucibles. The crucibles were cleaned before introducing the elements to be evaporated. Each crucible is separated and shielded from that adjacent to it by partitions which are 20 mm in height to prevent cross-contamination during deposition. Electrons are supplied by the electron gun. The filament current can be varied thus changing the electron beam current which in turn alters the rate of deposition. Sample holders, each of which can take up to seven samples, are loaded face down on a rotating platform which can take up to six sample holders. A quartz monitor was used to determine the deposition rate as well as the thicknesses of evaporated layers. All depositions were done in vacuum. The vacuum was maintained by means of ion pumps, sublimation pumps, cryopanel and turbomolecular pump. The top part of the evaporator can be isolated from the bottom part by means of a baffle valve (see Fig. 2.1). This valve was kept closed during the cleaning of crucibles and re-loading of samples, so that the bottom part was at a pressure better than $\approx 10^{-8}$ kPa. Pressure measurements were taken by means of a Penning gauge in the range of 10^{-3} kPa to 10^{-8} kPa.

The ion pump consists of pumping elements which are surrounded by a strong magnetic field. Each pumping element consists of a multi-cell structure between two titanium cathode plates. A voltage of about 6000 V is maintained between the anode and the cathode. Electrons moving from the cathode to the anode are forced by the magnetic field to spiral, thus increasing their path and probability of colliding with gas molecules. Collisions ionize the gas. Positively charged gas ions are accelerated by the electric field and move towards the titanium cathode. This effect sputters the titanium atoms. Titanium then getters the oxygen and nitrogen part of the gas. The gettering action of the ion pumps is increased by sublimation and cryopumping. The turbo pump on the top part of the evaporator can reduce the pressure to about 10^{-5} kPa if it is left to pump overnight. On opening the baffle valve and pouring liquid nitrogen, the vacuum is improved to about 10^{-9} kPa. Vapors such as H_2O and CO_2 are trapped on the cooled surface of the cryopanel. Non-condensable gases are then carried down by the condensable vapor and then trapped within the condensate. Sublimation pumps are also used to further decrease the pressure.

After evaporation the samples were allowed to cool in vacuum for more than one hour to prevent oxidation of the samples. As a further precaution, the vacuum was broken by means of dry high grade nitrogen.

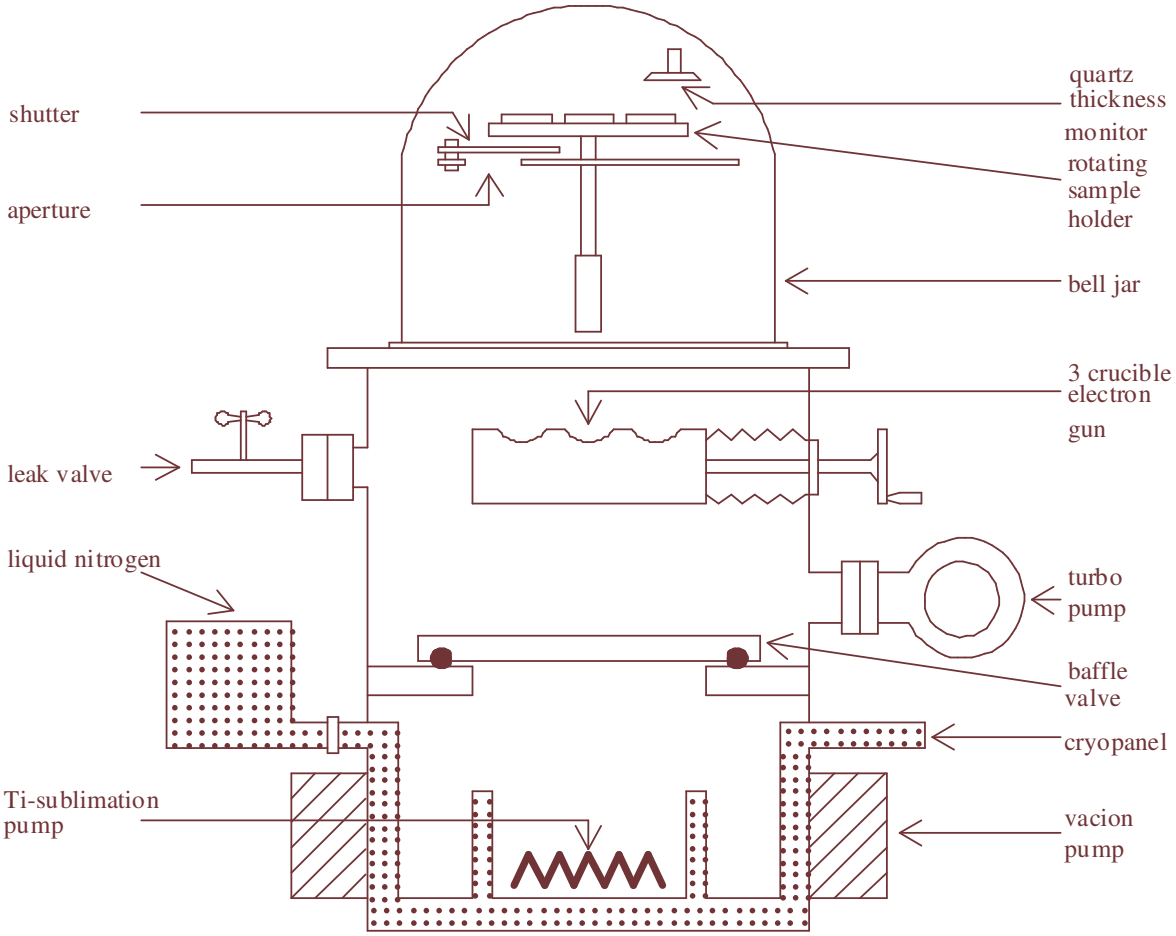

Figure 2.1: Schematic illustration of the high vacuum system used for electron beam evaporation of thin films. The upper section contains the sample holder, thickness monitor and electron gun. The baffle valve is closed to ensure that the lower section of the system is maintained under vacuum when the system is not in use or during sample changing.

2.1.3 Nonconventional Thin Film Structures

The materials to be evaporated were placed in a three-crucible water-cooled copper hearth and evaporation was accomplished by electron beam heating using the vacuum deposition system described in the previous section. The two unconventional (i.e., with marker) thin diffusion couples used in this investigation were prepared with a very thin layer of an inert material (Ta)

sandwiched between the germanium substrate and the overlying metal film. The Ta was only used as an inert marker to monitor the direction of atomic mobility. All the depositions were carried out at room temperature. The first sample was obtained by depositing a 5-Å thin layer of tantalum (Ta) on a <100>-oriented germanium substrate under ultra-high vacuum. Then an 800-Å thick layer of nickel was deposited on top of the Ta, without breaking the vacuum. This resulted in a sample with a layer structure of Ge<100>/Ta(5 Å)/Ni(800 Å). A slash "/" between two materials indicates deposition sequence. The second sample was obtained by first depositing a 6 Å thin layer of Ta on a <100>-oriented germanium substrate. Then without breaking the vacuum, a 490 Å thick layer of germanium was deposited on top of the Ta. Finally, under the same vacuum conditions a 470 Å thick layer of nickel was deposited on top of the 490 Å thick layer of germanium. The sample produced had a configuration of Ge<100>/Ta(6 Å)/Ge(490 Å)/Ni(470 Å). The base pressure during electron beam vacuum evaporation was kept in the low 10^{-7} torr region.

By controlling the current through the electron gun, the deposition rate was kept typically around 4-5 $Ås^{-1}$ for Ni and Ge deposition and 1 $Ås^{-1}$ for Ta deposition. Layer thicknesses were monitored with a vibrating quartz crystal.

The prepared samples were then heat treated to induce the formation of nickel germanides and characterized using in situ real-time Rutherford Backscattering Spectrometry.

2.2 Sample Characterization

Rutherford Backscattering Spectrometry (RBS) was the only method used in this study to determine the compound phases that grew during annealing as well as their thicknesses. RBS is a beam-based non-destructive method of analysis which does not necessitate direct mechanical contact and is thus one of the most powerful analytical tools for surface and near-surface region analysis for solids. Two of the commonly used variants of the RBS technique are in situ real-time RBS, which was employed in this study, and conventional or normal RBS.

2.2.1 Conventional (Normal) RBS

In conventional RBS, a series of samples have to be prepared and annealed for different times. Each sample is then analyzed using RBS and the spectra are compared in order to obtain

information on how phases evolve with time. The major problem with this approach is the sample to sample variation in structure and impurity content (which are assumed to be absent in studies that employ conventional RBS). The preparation of many samples required in this form of RBS is problematic as it entails consumption of more materials. Each of the samples must then be annealed separately which leads to the problem of long data acquisition time. Conventional RBS also suffers from complications that might arise in cases where sample preparation is difficult or sometimes irreproducible due, for example, to experimental detail [89]. These problems are eliminated by using in situ, real-time RBS.

2.2.2 In Situ Real-time RBS

This is the variants of the RBS technique that was used to characterize the samples in the present study. In contrast to conventional RBS, in situ real-time RBS is achieved by complementing the simultaneous depth and compositional profiling capabilities of RBS with in situ annealing. With real-time RBS, the sample is continuously analyzed while it is simultaneously subjected to a thermal anneal to induce phase formation. In this way all the information about the evolution of phases is derived from a single sample by linear ramped thermal annealing in the scattering chamber while the RBS signal is continuously acquired. The phase formation characteristics can thus be monitored in real-time. This makes RBS an ideal non-destructive analytical tool for the study of thin film solid state interactions. The term “real-time” is indeed appropriate because the data acquisition system is fully automated with a PC interface. The monitor of the PC displays the virgin sample spectrum, the current spectrum, the spectrum 20 minutes before, the contour map of the reaction, the beam current and the temperature simultaneously giving a more or less photographic view of the reaction as it is actually taking place. Firstly, the sample was mounted on the flat surface of a copper heating stage with a highly thermal conducting silver paste. To avoid channelling the sample is mounted slightly tilted so that none of the sample edges is parallel to the vertical or horizontal. This was done outside the scattering chamber. The heating stage was then transferred into the RBS scattering chamber. Inside the RBS chamber, silver rings surrounding the heating stage shielded the chamber from the heating stage and also formed an air-cooled heat sink to minimize unwanted heating of the chamber. The heating stage was placed at such an angle that the normal of the sample was tilted 50^{o} away from the incident beam direction as illustrated in Fig. 2.2. The temperature of the sample was monitored with a

thermocouple. The thermocouple was mounted from the rear through a narrow hole drilled in the copper block so that the tip of the thermocouple was located just underneath the copper surface. The thermocouple was calibrated using the eutectic melting points of Au-Si (T_m = 363 ^oC) and Al-Si (T_m = 577 ^oC) systems. Both of these systems are simple eutectics with no intermetallic phases. The melting of a eutectic is not a thermally activated process and results in a large and abrupt change in resistance. By measuring the surface resistance of the two systems as a function of the thermocouple temperature, the relationship between the actual sample temperature and the temperature reading of the thermocouple embedded in the copper heating stage was determined. The resistance was measured using the standard four point probe geometry.

The RBS chamber was pumped down to a pressure of about $5x10^{-4}$ torr by a combination of the turbo and rotary pumps. With the help of a liquid nitrogen cold trap, formed by the conical trough in the lid of the RBS scattering chamber, the pressure inside the scattering chamber was brought to down to the low 10^{-7} torr. The RBS spectra were acquired continuously in situ while the sample was annealed. The heating stage temperature was controlled by a Eurotherm 815 microprocessor which was part of a feedback system between a thermocouple mounted in the heating stage and the heating stage power supply. This allowed a temperature cycle which included isothermal or linear temperature ramps to be pre-programmed. The scattering geometry for the RBS data acquisition is shown in Fig. 2.2.

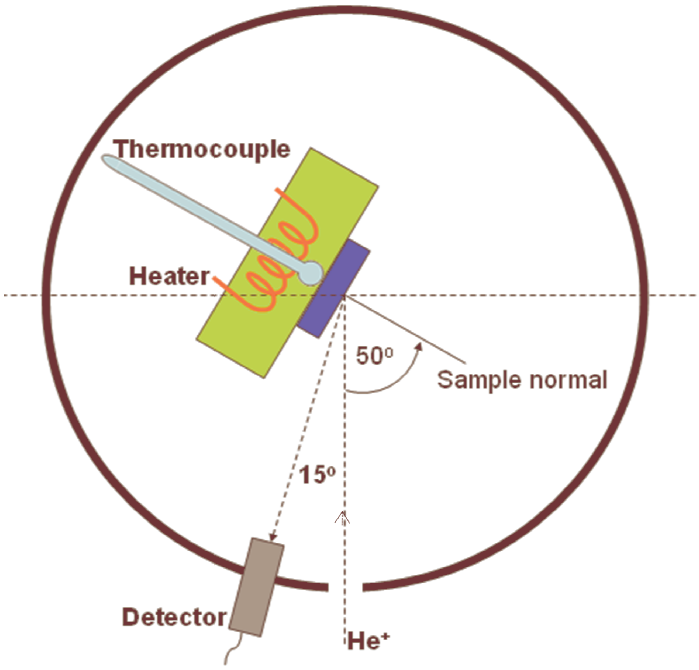

Figure 2.2: Setup for in situ, real-time RBS data analysis.

The RBS spectra were acquired continuously and stored at regular intervals of 30 seconds. The acquired charge and recorded sample temperatures were also saved with each spectrum in an event by event mode which could subsequently be played back by different softwares for analysis. A 2.0 MeV $^{4}He^{+}$ beam was used with a scattering angle of 165^{o}. After the run was completed the RBS spectra could be added to improve the statistics and the charge normalized. Any variations in charge measurement were corrected for by requiring that a certain region of the substrate contain the same number of counts in all spectra.

The RBS spectra were then analyzed using the RUMP [90, 91] computer simulation package. Since sequential spectra do not differ too much it is possible to quickly analyze them by the semi-automatic perturbation code.

The next section describes the general features and the physical concepts on which the RBS technique is based.

2.3 RBS Technique

The origin of backscattering can be traced back to 1908 when Rutherford conceived an idea of testing Thompson's plum pudding model of the atom by measuring deflection of alpha particles

from a thin gold foil [92]. The method was employed in 1951 by nuclear physicists to analyze their targets [93] but extensive application to material science began in the late 1960s [94]. The backscattering technique has been greatly refined and now constitutes one of the most common methods for compositional analysis of surface regions.

In RBS the sample constituting the target is irradiated by a beam of high-monoenergetic and mono-atomic probe ions, usually H or He ions with energies in the range 1-4 MeV, which provide information about the target structure and composition when the energy of the backscattered beam of ions is analyzed. Both the mass and depth resolution are poorer for H ions than for He ions but H ions are sometimes used in RBS for the analysis of deeper regions. When the sample is thin almost all the incident particles are transmitted through the target with only a slightly reduced energy and a slightly altered direction. A few particles are lost due to close encounters with the nuclei of single atoms and undergo large changes in both energy and direction [92]. If the sample is thick, as is the case with thin films deposited on thick substrates, almost all the ions penetrate deep into the sample up to approximately 10 μm [94] until all their kinetic energy is lost. However, some of the ions collide with the target atoms during penetration and are subject to elastic Coulomb scattering (Rutherford scattering) between the projectile and the target nuclei and may be backscattered from the sample. The dependence of the energy of the backscattered ions on the atomic mass of the target atoms allows compositional analysis by measuring the energy spectrum of the backscattered ions [92].

In addition to the simplicity of the RBS experiment in both its concept and execution, RBS has many other outstanding features which include [92]:

(1) Allowing quantitative analysis of all elements simultaneously except for hydrogen (as explained in next section);

(2) Possession of a depth resolution typically of about 10 nm which can be improved up to monolayer resolution in the surface region with special equipment;

(3) Short measurement time;

(4) Good sensitivity of about 100 ppm for heavy elements although it is not so good for light elements;

(5) It is a nondestructive method of analysis.

The RBS technique relies only on four basic physical concepts. Each of these concepts is at the origin of a particular analytical capability or limitation of the backscattering spectrometry technique and corresponds to a specific physical phenomenon. These are [92, 94]:

(1) The kinematic factor which describes energy transfer from a projectile to a target nucleus in an elastic two-body collision. This leads to the capability of mass determination since the resulting energy of the backscattered ion increases with the mass of the target atom. This allows identification of the target atom mass by measuring the energy of the backscattered ion;

(2) The differential scattering cross section which gives the probability that a collision will result in a detected particle. This leads to the capability of quantitative analysis of atomic composition;

(3) The stopping power or stopping cross section which is defined by the average energy loss of the probe ion per unit length inside the target. The backscattered energy depends on the depth from which the ion was scattered because the path length is proportional to the depth. This leads to the capability of depth profiling of elements in the target;

(4) The energy-loss straggling which is defined as the fluctuation of the energy loss arising from the statistical feature of the energy loss process. This leads to a limitation in the ultimate mass and depth resolution of backscattering spectrometry.

2.3.1 The Kinematic Factor *K*

When a particle of mass M_1 in a monoenergetic beam of probe ions moving with constant velocity collides with a stationary target particle of mass M_2, energy will be transferred from the moving particle (projectile) to the stationary particle (target). If $M_2 = \infty$, M_1 is scattered back without any loss of energy. If $M_2 = M_1$, then M_1 transfers all its kinetic energy to M_2 and comes to rest while M_2 moves forward with the initial energy of M_1. For the case $M_2 < M_1$, part of the energy of M_1 is transferred to M_2 and both particles move forward. This makes it difficult to analyze hydrogen with backscattering because hydrogen is the lightest element and thus cannot backscatter any other elements. If $M_2 > M_1$, M_1 is scattered back after transferring part of its initial energy to M_2 which is the situation that prevails in backscattering experiments.

The two conditions that must be satisfied in order for the assumption that the interaction between atoms is properly described by the simple elastic collision of two isolated particles are [92, 94]:

(1) The projectile energy E_0 must be much larger than the binding energy of the target atoms and their thermal vibrations. This condition is easily met for 2 MeV He ions used in backscattering experiments since chemical bonds are of the order of 10 eV;
(2) There must not be nuclear reactions and resonances. This imposes an upper limit to the projectile energy.

The simple elastic collision between a projectile atom of mass M_1 and a target atom of mass M_2 can be fully solved by applying the principle of conservation of energy and momentum. Before collision the incident energetic particle of mass M_1 has an initial velocity v_0 and energy $E_0 = \frac{1}{2} M_1 v_0^2$ while the target atom of mass M_2 is initially at rest. The velocities and energies v_1, $E_1 = \frac{1}{2} M_1 v_1^2$ and v_2, $E_2 = \frac{1}{2} M_2 v_2^2$ of the projectile atom and target atom after collision respectively are determined by the scattering angle θ and the recoil angle ϕ. The notation and geometry for this scattering problem in the laboratory system of coordinates is given in Fig. 2.3.

By definition the kinematic factor *K* is the ratio of the projectile energy after elastic collision to that before the collision, i.e.,

$$K = \frac{E_1}{E_0} = \left(\frac{v_1}{v_0} \right)^2 . \qquad (2.1)$$

Application of the principle of conservation of energy and momentum parallel and perpendicular to the initial direction of incidence leads to

$$K_{M_2} = \left[\frac{(M_2^2 - M_1^2 \sin^2 \theta)^{\frac{1}{2}} + M_1 \cos\theta}{M_2 + M_1} \right]^2$$

$$= \left\{ \frac{\left[1 - (M_1/M_2)^2 \sin^2 \theta\right]^{\frac{1}{2}} + (M_1/M_2)\cos\theta}{1 + (M_1/M_2)} \right\}^2 . \qquad (2.2)$$

Following traditional practice, a subscript has been added to *K* to denote the target mass for which the kinematic factor applies.

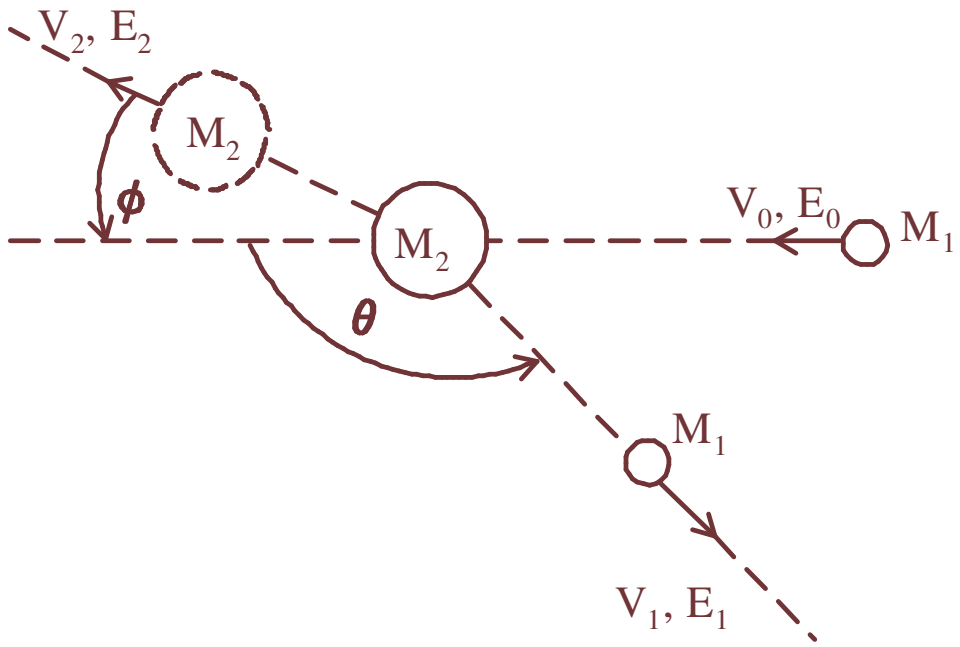

Figure 2.3: Schematic representation of an elastic collision between a projectile of mass M_1, velocity v_0, and energy E_0 and a target of mass M_2 which is initially at rest. After the collision, the projectile and target masses have velocities and energies v_1, E_1 and v_2, E_2 respectively. The angles θ and φ are positive as shown and all quantities refer to a laboratory frame of reference.

The basic idea of RBS relies on Eqn. 2.2. It is clear from this equation that the kinematic factor is determined only by the mass ratio M_1/M_2 and the scattering angle θ. A plot of the kinematic factor as a function of the mass ratio M_1/M_2 is given in Fig. 2.4 [94]. It can be seen from Fig. 2.4 that kinematic factor and hence the backscattered ion energy increases monotonically with the mass ratio. This indicates that the target atom mass can be determined from the observed scattered ion energy.

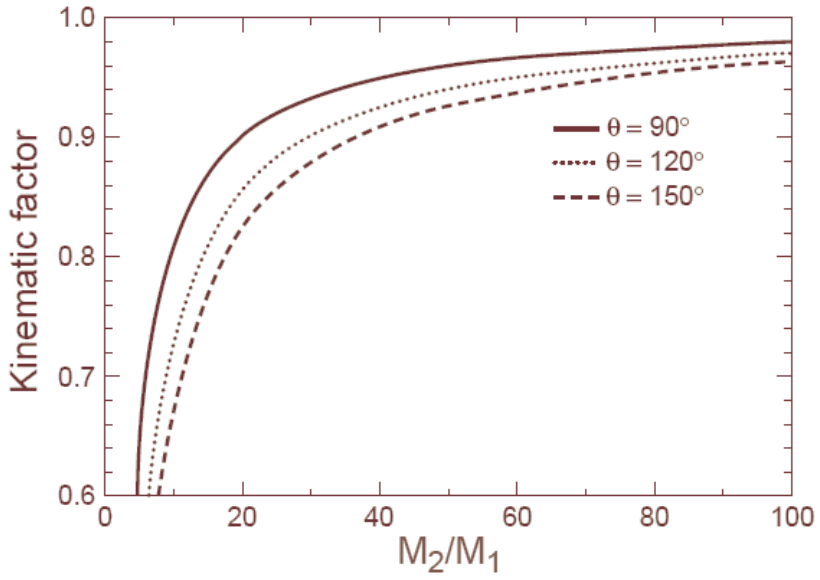

Figure 2.4: Kinematic factor K as a function of the ratio of the target mass to the ion mass $(M_1/M_2)^{-1}$ [94].

2.3.2 The Differential Scattering Cross Section (dσ/dΩ)

The physical concept of kinematic factor establishes the relationship between the energy E_0 of the incident particle of mass M_1 and the energy $K_{M_2}E_0$ possessed by the same particle at any angle θ after an elastic collision with an initially stationary target atom of mass M_2. However it says nothing about the probability of the incident particles being scattered into a given solid angle where they can be recorded by a detector. The differential scattering cross section is the concept that is introduced to relate the number of detected particles Q_D to the total number of incident particles Q and the number of atoms per unit area N_S of the target material.

The differential scattering cross section in the laboratory frame of reference is given by

$$\frac{d\sigma}{d\Omega} = \left[\frac{Z_1 Z_2 e^2}{4E}\right]^2 \frac{4}{\sin^4\theta} \frac{\left(\left[1-\left((M_1/M_2)\sin\theta\right)^2\right]^{\frac{1}{2}} + \cos\theta\right)^2}{\left[1-\left((M_1/M_2)\sin\theta\right)^2\right]^{\frac{1}{2}}}. \qquad (2.3)$$

For $M_1 << M_2$ the angular dependence of the right hand side of equation 2.3 can be expanded in the power series to give

$$\frac{d\sigma}{d\Omega}=\left(\frac{Z_1Z_2e^2}{4E}\right)^2\left[\sin^{-4}\frac{\theta}{2}-2\left(\frac{M_1}{M_2}\right)^2+\cdots\right] \qquad (2.4)$$

where Z_1 and Z_2 are the atomic numbers of the projectile and target atoms respectively and e is the electric charge.

The significant functional dependences of the Rutherford cross section revealed by equation 2.4 are:

(i) $\frac{d\sigma}{d\Omega}$ is directly proportional to Z_1^2. This means that for a given target atom higher backscattering yields are obtained from heavier projectile atoms;

(ii) $\frac{d\sigma}{d\Omega}$ is directly proportional to Z_2^2. Thus, for a particular projectile atom heavier target atoms produce higher backscattering yields;

(iii) $\frac{d\sigma}{d\Omega}$ is inversely proportional to E^2. Therefore, the lower the incident particle energy the higher the yield of backscattered particles;

(iv) $\frac{d\sigma}{d\Omega}$ is axially symmetrical with respect to the axis of the incident particle beam since it a function of θ only;

(v) $\frac{d\sigma}{d\Omega}$ is approximately inversely proportional to $\sin^4\frac{\theta}{2}$ when $M_1 << M_2$ so that a reduction in the scattering angle θ results in rapidly increasing backscattering yields.

In backscattering experiments the detector solid angle is very small (10^{-2} steradian or less [95]) so that an average differential scattering cross section $\sigma(\theta)$ can be defined as

$$\sigma(\theta)=\left\langle\frac{d\sigma}{d\Omega}\right\rangle=\frac{1}{\Omega}\sum\left(\frac{d\sigma}{d\Omega}\right)_i d\Omega_i \,. \qquad (2.5)$$

Since both $\left(\frac{d\sigma}{d\Omega}\right)_i$ and $d\Omega_i$ are very small the summation can be replaced by an integral

$$\sigma(\theta)=\frac{1}{\Omega}\int_{\Omega}\frac{d\sigma}{d\Omega}d\Omega \,. \qquad (2.6)$$

2.3.3 The Energy Loss *dE/dx*

The high unlikelihood of the large angle Rutherford scattering collisions means that most of the particles in an energetic beam impinging on a target will penetrate into the target. The fate of the impinging energetic particles is largely determined by processes that control penetration into the target rather than large-angle collisions. Therefore implantation of beam particles into the target is the first-order process, making backscattering spectrometry a secondary process analytical method. The impinging particles lose energy and slow down as they penetrate the target via many individual encounters with electrons of the target atoms which are either raised to excited states or ejected from the atoms. As the impinging ion penetrates the target medium it loses an amount of energy ΔE per distance Δx traversed which depends on the identity and velocity of the projectile as well the density and composition of the target. The energy lost per unit path length is referred to as the stopping power. Fig. 2.5 gives a depth illustration of a particle beam scattered through a thickness Δx of a target sample. In Fig. 2.5, E is the energy of the particle before scattering and the meanings of the other symbols are as described in section 2.3.1.

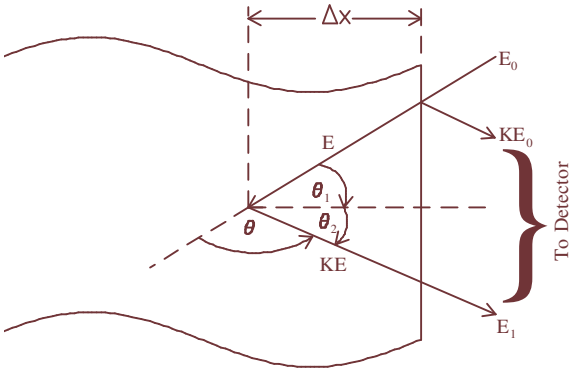

Figure 2.5: A depth illustration of a beam particle scattered through a thickness Δx of a target sample. θ_1 and θ_2 are the angles made by the incident beam and the scattered beam with the normal to the sample surface respectively.

The energy difference between a particle scattered from the surface and that scattered from a depth Δx is given by

$$\Delta E = KE_0 - E_1 = \left(\frac{K}{\cos\theta_1} \frac{dE}{dx}\bigg|_{in} + \frac{1}{\cos\theta_2} \frac{dE}{dx}\bigg|_{out} \right) \Delta x \qquad (2.7)$$

where dE/dx is the energy loss per unit length averaged along the inward and outward path. Equation 2.7 can be simplified to

$$\Delta E = [S]\Delta x \qquad (2.8)$$

where $[S]=\left(\frac{K}{\cos\theta_1}\frac{dE}{dx}\Big|_{in}+\frac{1}{\cos\theta_2}\frac{dE}{dx}\Big|_{out}\right)$ is commonly referred to as the energy loss factor. Measurement of ΔE provides the ability of depth resolution.

2.3.4 The Stopping Cross Section ε

It has been shown in the previous section through equation 2.8 that the energy width ΔE in a backscattering spectrum is related to the thickness Δx by the factor $[S]$ which is itself a function of the energy loss per unit length dE/dx. However, it is useful to express the energy loss in terms of the stopping cross section ε. The stopping cross section gives the number of target atoms per square centimetre that are traversed and is given by $(1/N)dE/dx$, where N is the number of target atoms per unit volume. Information on energy loss per unit length dE/dx is generally presented in the form $dE/\rho dx$ or the stopping cross section which is given by

$$\varepsilon = \frac{1}{N}\frac{dE}{dx} = \frac{M}{N_0}\frac{dE}{\rho dx}. \qquad (2.9)$$

In Eqn. 2.9, M and ρ are the atomic mass and mass density (mass per unit volume) of the target respectively while N_0 is Avogadro's number. An energetic particle traversing a medium loses energy through a random sequence of independent encounters with electrons of the target atoms. For a target consisting of more than one element the Bragg law, which is based on the simple assumption that the constituent elements act independently in the energy loss process, gives the energy loss as the sum total of the losses of the constituent elements weighted by the abundance of the elements. Let us suppose that when a hypothetical conventional thin film diffusion couple formed of pure elemental components A and B is annealed a compound target of stoichiometry A_xB_{1-x} is formed. Then using the Bragg law, the stopping cross section of this compound is given by

$$\varepsilon_{A_xB_{1-x}} = x\varepsilon_A + (1-x)\varepsilon_B \qquad (2.10)$$

where ε_A and ε_B are the stopping cross sections of the constituents.

2.3.5 The Energy-Loss Straggling δE_S

The stochastic nature of the processes by which an energetic particle loses energy as it penetrates a medium causes the slowing down of ions to be accompanied by energy spreading. This is called energy-loss straggling or simply energy straggling. Therefore energy straggling places a finite limit on the precision with which energy losses, and hence the depths, can be resolved by backscattering spectrometry. This phenomenon also impairs the ability to identify masses except for atoms located at the surface. The reason for this is that even if the incident beam energy E_0 was initially monoenergetic, the energy E before collision with a specific target atom M_2 at some depth within the target is no longer monoenergetic. For this reason, determination of the kinematic factor K_{M_2} and hence the identification of M_2 become equally uncertain. It is therefore important to have quantitative information on the magnitude of energy straggling for any given combination of energy, target material and thickness, and projectile.

2.3.6 Computer Simulation Analysis of RBS Spectra

When the mass difference of elements is small the signals overlap in a spectrum. The derivation of target composition as a function of depth in such cases is not straightforward. Since elemental and depth information is convoluted in RBS spectra, the use of computer simulation is a powerful approach to deconvolute this information in the analysis of RBS data. There are a number of computer simulation programs for analyzing RBS spectra which include RUMP [90, 91], GISA [96, 97], SCATT/HYPRA [98], SIMNRA [99, 100], ANN [101, 102], CASSIS [103], and IBA DataFurnace [104]. To simulate RBS spectra with a program like RUMP, the composition of the target is changed until the calculated spectrum matches the measured spectrum; that is until the simulation fits the actual spectrum. This is an inverse problem and like any other inverse problems, this procedure may obtain a local minimum. A simulated annealing algorithm was recently successfully applied to the analysis of RBS spectra [105]. This algorithm tends to the absolute minimum rather than to a local minimum with any initial composition which allows fully automatic analysis without time-consuming human intervention. With RUMP, convergence to the absolute minimum is ensured by increasing and decreasing the composition at the current minimum and checking whether this leads to the same minimum. The semi-automatic PERT code of the RUMP program allows simulation of RBS spectra with

minimum human intervention. Computer simulations of energy widths and signal heights are also an excellent guide in the design of sample configuration and scattering geometry.

2.3.7 Set Up of the RBS System

The main components of a standard RBS system are presented in the block diagram of Fig. 2.6. The megaelectron-volt probe ions are mostly produced by the Van de Graaff, Cockcroft or Walton type of accelerators.

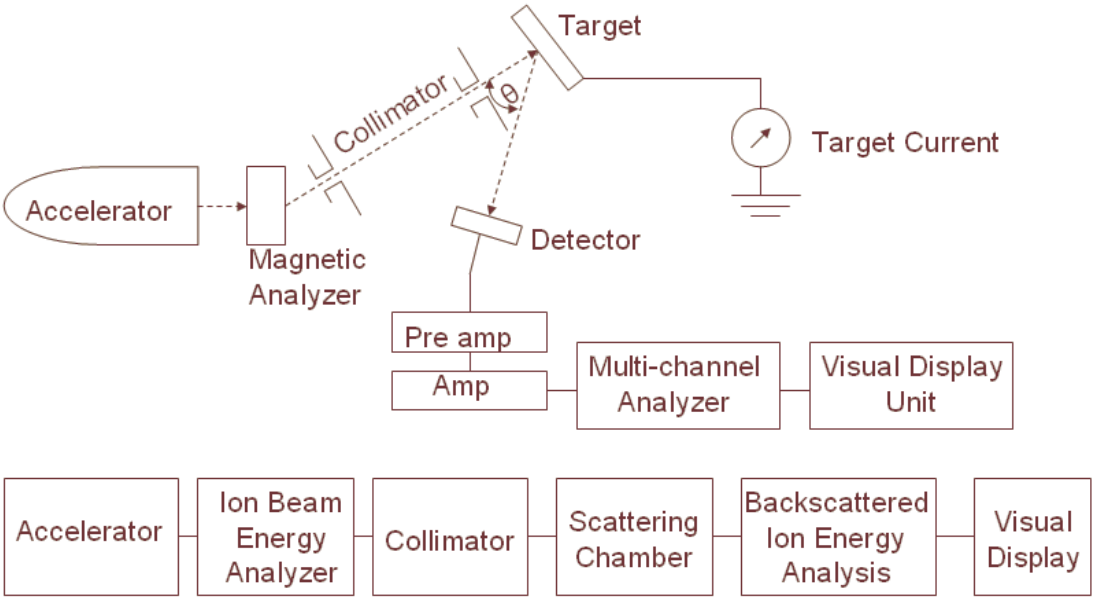

Figure 2.6: Schematic diagram of an ion backscattering experiment [92].

The Van de Graaff electrostatic accelerator, either single ended or double ended (tandem Van de Graaff) is by far the most widely used for the production of MeV ion beams [106]. Since the accelerators normally produce ions in several charge states and even a multiplicity of species, the beam is passed into the field of an analyzing magnet to eliminate contaminant ion species and select the ion energy in order to extract a beam suitable for materials analysis. A mass and charge selected ion beam then enters an ultra- high vacuum (UHV) environment via differentially pumped apertures which collimate the beam to a typical size of 1 mm^2.

The beam is then steered to the target mounted on a manipulator by magnetic or electrostatic lenses. When small beam spots are desired as in microprobe RBS, they can be obtained by suitable apertures and lens systems.

The analyzing magnet is usually calibrated by using resonant nuclear reactions. The beam current which is typically of the order of 10 nA is usually monitored by a monitoring system installed between the final aperture and the target. When channelling [92] measurements are required, the beam divergence angle and precision of the manipulator should be less than 1 mrad [94]. The detection of backscattered ions is usually performed with:

(1) A solid-state detector which can be a silicon surface barrier (SSB) detector or a passivated implanted planar silicon (PIPS) detector;

(2) A time-of-flight (TOF) detector;

(3) An electrostatic or magnetic analyzer.

For routine RBS analysis an SSB detector installed inside the scattering chamber is used for measuring the energy spectrum of the scattered ions. The properties of silicon which makes it especially desirable as a detector material include:

(1) Low ionization energy (good signal);

(2) Long mean free path (good charge collection efficiency);

(3) High mobility (fast charge collection);

(4) Low Z (low multiple scattering);

(5) Very well developed silicon technology.

The SSB detector is basically a Schottky barrier diode. Application of a reverse bias to this diode creates a depletion region of the order of 100 μm [94] which is greater than the penetration range of the megaelectron-volt light ions. The bias is placed across two electrodes sandwiching the semiconductor which causes the electrons and holes to move in opposite directions thereby separating the charges. The bias also prevents electrons and holes from recombining. The backscattered ions create electron-hole pairs in the depletion region which are swept away by the high electric field. The high applied voltage pulls the electrons to the back of the detector, where they are collectively recorded as a negative pulse. A multi-channel analyzer (MCA) then counts these pulses, and sorts them into size (which is equivalent to the ion energy). The collected charge on the electrodes (i.e., the current) is sent to an amplifier. There is a linear relationship

between the total energy spent to create the electron-hole pairs (about 3.6-3.7 eV per electron-hole pair) and the quantity of charge collected [94]. The higher the ion energy, the larger the number of electron hole pairs. The linearity between the collected charge and the ion energy is quite good for megaelectron-volt light ions.

The signal from the semiconductor detector is in the form of voltage pulses. This signal is amplified by a pre-amplifier and a linear amplifier and then sent to a pulse height analyzer (PHA). The PHA stores pulses of a given height in a given voltage bin or channel (hence the alternative description, MCA). The channel numbers are calibrated in terms of the pulse height which establishes a direct relationship between channel number and energy [95]. The sources of energy loss in the detection system are in the entrance window and nuclear scattering. Without these losses the pulse height in the output would be more. The equivalent thickness of the entrance window is about 100 nm, which translates to an energy loss of about 30 keV for 1-MeV He ions [94]. For heavy ions these effects become serious and must be taken into account when converting pulse height to ion energy, especially in the low-energy region.

2.4 Dominant Diffusing Species (DDS)

The formation of a compound at the interface of a binary couple involves the relative motion of atoms past each other. The process of diffusion is the mechanism responsible for the displacement of the atoms. Thus, a situation can be imagined in which only atoms of one element diffuse while atoms of the other species do not change their relative positions. It could also be that the atoms of the first element are the ones that do not diffuse while those of the other species diffuse. The reality usually lies between these two limiting cases. It is therefore of interest to know which of the two species is the dominant diffusing species. The knowledge of diffusing species sheds light on the microscopic processes that control reactions. Also, some practically relevant properties of the compounds formed during solid state reactions can depend very directly on the identity of the diffusing species. For this reason, several types of marker experiments have been developed and used to obtain information on the motion of atoms during solid-state reactions.

The term marker refers to a material deliberately introduced into the sample to act as a tracer or reference plane for monitoring the flow of atoms during a reaction. Hartley [107] was the first to

use purposely introduced foreign inert particles, titanium oxide (TiO_2) in an organic acetone/cellulose-acetate system, to study the inequality of the diffusing species. Marker techniques can be classified in two broad categories as either inert markers or tracer-type markers.

2.4.1 Tracer-type markers

These are atom-size markers intended to trace the location of one or other type of element involved in the formation of a new binary phase. They can be formed in one of the following ways:

(1) Maximization of the chemical affinity of a third element with respect to one of the two species of a binary reaction couple. The best example of this type of marker is the use of traces of oxygen in Si to act as a marker for Si in the formation of Ni_2Si [108], because oxygen bonds strongly to Si ($\Delta H_f^o(SiO_2) = -205.5$ kcal/mole) and very weakly to Ni ($\Delta H_f^o(NiO) = -58.4$) kcal/mole [40]. Although oxygen is found to slow down the reaction somewhat, it does not however modify the phases formed or the dominant diffusing species [40];

(2) Substitution of a stable atom whose movement is desired to be monitored by its radioactive isotope as in the use of ^{31}Si to act as a marker for ^{30}Si. This is known as the radiotracer method because it requires radioactive isotopes of the diffusing element. Although isotopes are chemically indistinguishable, their net movement can be monitored through their radio emission in the form of concentration profiles before and after the reaction. In concept, any layer with an artificially enhanced concentration of a stable isotope could serve as a marker but this poses a problem in that isotopes only differ by a few atomic mass units which requires high mass resolution techniques in order to monitor the marker movement. Secondary ion mass spectrometry (SIMS) offers high mass resolution but its depth resolution and quantification are problematic. On the other hand, Backscattering Spectrometry (BS) combines good depth resolution and quantification but its mass resolution is poor. Baglin et al. [109] circumvented this dilemma by using as a marker a third element that is much heavier than the element being traced but which falls in the same chemical subgroup of the periodic table to minimize chemical difference between the two species such as using Ta to mark niobium (Nb) or tungsten (W) to

mark molybdenum (Mo). Finstad used this method to show that Ni and platinum (Pt) are the diffusing species in the Ni_2Si and Pt_2Si reactions [110].

2.4.2 Fiducial (Inert) markers

In this type of marker technique a very thin layer of a third element, usually a refractory metal, which is quite distinct (much heavier) from the two reacting elements is deposited at the interface or implanted within the growing layer of the reacting species. The displacement of the plane of the inert marker depends on the net flow of the atoms past the marker [111]. This displacement is in a direction opposite to that of the flow of the dominant diffusing species. In Figure 2.7 (a), we present a schematic nonconventional thin film diffusion couple formed of pure elemental components A and B. If atomic species B is the DDS during the formation of a compound A_xB_{1-x}, then the marker is displaced to the right (i.e., towards the surface of the hypothetical diffusion couple) as shown in Fig. 2.7 (b). If atomic species A is the DDS during the formation A_xB_{1-x}, then the marker is displaced to the left (i.e., away from the surface of the hypothetical diffusion couple) as shown in Fig. 2.7 (c).

In order for the marker to be truly inert, the marker object is assumed to fulfil the following conditions:

(1) It must be chemically inert with respect to its surroundings, that is, it should not take part in the diffusion or react with any of the components at the temperatures where the thermal treatment takes place;

(2) It should not interfere significantly with the overall development of the reaction (although it will necessarily do so locally [89]);

(3) It should not be selectively coupled to the diffusive motion of either element involved in the reaction but rather serve as an object against which the overall flux of atoms of either kind may be measured;

(4) It must be readily identifiable before and after annealing.

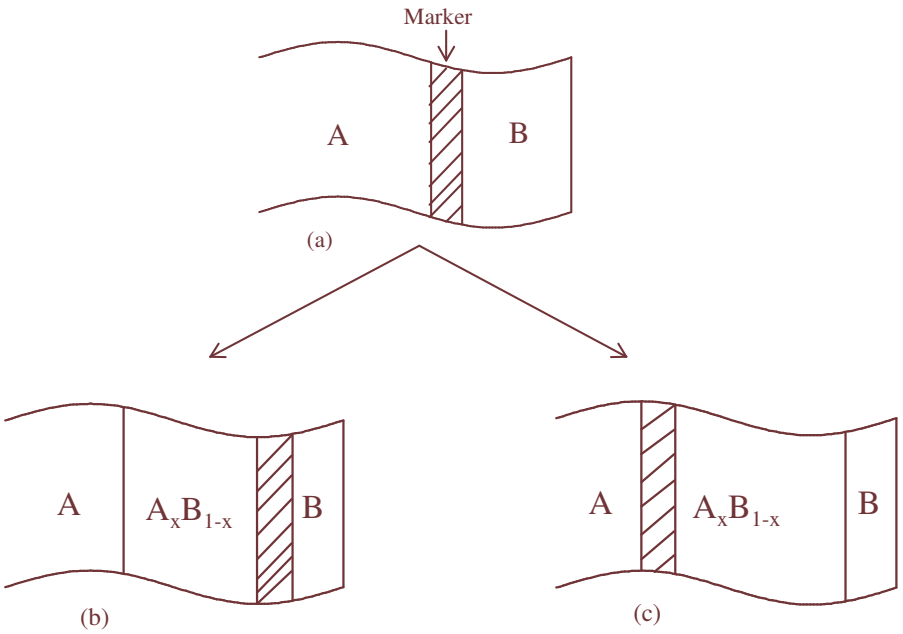

Figure 2.7: (a) Schematic representation of the virgin sample. Here (b) and (c) show the relative shift of the marker plane after annealing with B and A as the dominant diffusing species respectively.

Although markers are intended to be inert, they very often are barriers to the free motion of the atoms and the degree to which a specific marker interferes with the reaction depends to a large extent on the conditions at the interface created by insertion of the marker [89].

In this study Ta was chosen as a suitable marker to monitor the direction of atomic mobility during the reaction of Ni with Ge for two reasons. Firstly, it is relatively inert in the temperature range from room temperature to 350 ^{o}C (thermocouple reading) used in the present investigation. This is supported by the results of a study by Marshal et al. [67] which showed that Ta only reacts with Ge at temperatures greater than 700 ^{o}C. Secondly, since Ta has a higher atomic mass, the Ta peak will be well separated from the Ge and Ni signals in the RBS spectra.

Inert markers commonly used in the past include thin layers of titanium (Ti) [112], Ta [89], Mo or W [67], while implanted inert gases such as xenon (Xe) [113] have also sometimes been used.

CHAPTER 3
RESULTS AND DISCUSSION

3.1 Introduction

3.1.1 Choice of Marker

Studies by Marshal et al. [67] and by Gaudet et al. [10] have shown that Ni, Pd and Pt form compounds with Ge at low temperatures (≤ 300 ^{o}C), while W and Ta form compounds with Ge at temperatures greater than or equal to 700 ^{o}C and Ti at temperatures of ~ 450 ^{o}C. Since in the present study the reaction between Ni and Ge was expected to be completed well below 400 ^{o}C either of W, Ta or Ti would have been suitable for use as a marker. The former two are however much heavier than Ge and Ni and thus their RBS signal will be well separated from the Ge and Ni signal while Ti, being lighter than Ge, will have its signal lost in the Ge background, making monitoring its movement by RBS impossible. Ta was made the marker of choice for this investigation because it was slightly easier to evaporate than W.

In the present study the solid state reactions of Ni and Ge are investigated by ramping the temperature using ramped annealing according to the temperature profile given in Fig. 3.2. In the interval 140 – 350 ^{o}C (thermal couple reading) the ramp rate was maintained at 1 ^{o}C/min. It should be pointed out that this was the temperature range set on the temperature controller. On calibration of the thermocouple this range was established as 23-333 ^{o}C. The calibration curve for obtaining these temperatures is given in appendix A. The method by which this curve was drawn is also explained in appendix A. Our ramped thermal anneal was from 20 ^{o}C to 350 ^{o}C as recorded by the thermocouple. Unless other stated, all temperatures shown in our figures and reported in the text were obtained in this manner from temperature readings of the thermocouple.

3.1.2 RBS spectra of Ni and Ta Films on Germanium

Before presenting and discussing the main results, an energy spectrum of a thin film of nickel deposited on a germanium substrate with a very thin layer of tantalum interposed between the nickel and germanium presented in Fig. 3.1 will be considered. This is necessary in order that the

salient features of an RBS spectrum arising from the complicated overlap of the Ni and Ge signals may be better understood. The insert in Fig. 3.1 shows a schematic diagram of the configuration of the sample from which the spectrum was taken. The spectrum presented in Fig. 3.1 is a measured RBS spectrum of the as-deposited sample (i.e., the sample before the beginning of the solid state reaction) with a configuration of Ge<100>/Ta(5 Å)/Ni(800 Å). This was one of the samples used in this study. It must be emphasized that Fig. 3.1 has only been included as a useful aid in understanding the energy spectra of Ta and Ni deposited on a Ge substrate which will be introduced later.

The ions scattered from each element form a separate peak. The number of target atoms in the film can be derived from the peak yields and the peak width gives the film thickness. Also shown in Fig 3.1 are the surface positions of Ta (channel 453.457 or 1.883 MeV), Ge (channel 396.325 or 1.610 MeV) and Ni (channel 375.691 or 1.529 MeV) together with the simulated contribution of the Ni and Ge signals to the RBS spectrum. The surface position of a particular element is the position where the signal of that element would appear if that element were at the surface of the sample. From the schematic of the sample configuration one can see that only Ni is at the surface of the sample and thus only the Ni RBS signal appears at its surface position in the energy spectrum. Referring to equation 2.1, only particles scattered from the surface of the Ni film have an energy given by the kinematic equation $E_1 = K_{Ni}E_0$. As particles traverse the solid, they lose energy along the incident path. Particles scattered from an Ni atom at the Ta-Ni interface therefore have energies less than $K_{Ni}E_0$. On the outward path the particles again lose energy. On emerging from the surface, the particles scattered at the Ta-Ni interface have a total energy difference ΔE_{Ni} from the particles scattered at the surface.

Since there are no Ta atoms at the surface position, the energy spectrum produced by scattering from Ta starts at a lower energy than $K_{Ta}E_0$ (with reference to equation 2.1). However, the Ta signal is well separated from the signals of Ni and Ge even though Ta is deeply buried below the Ni because the atomic mass of Ta is much larger than those of both Ni and Ge. The good separation between the Ta signal and those of Ge and Ni confirm that Ta is a suitable choice for a marker. As there are no Ge atoms on the surface, the energy spectrum produced by scattering from Ge also starts at an energy lower than $K_{Ge}E_0$ and then extends to zero energy because Ge atoms form the substrate with an effectively infinite thickness. The overlap between the front of

the Ge signal and the back of the Ni signal is what gives rise to the peak which appears to rise above a continuous background.

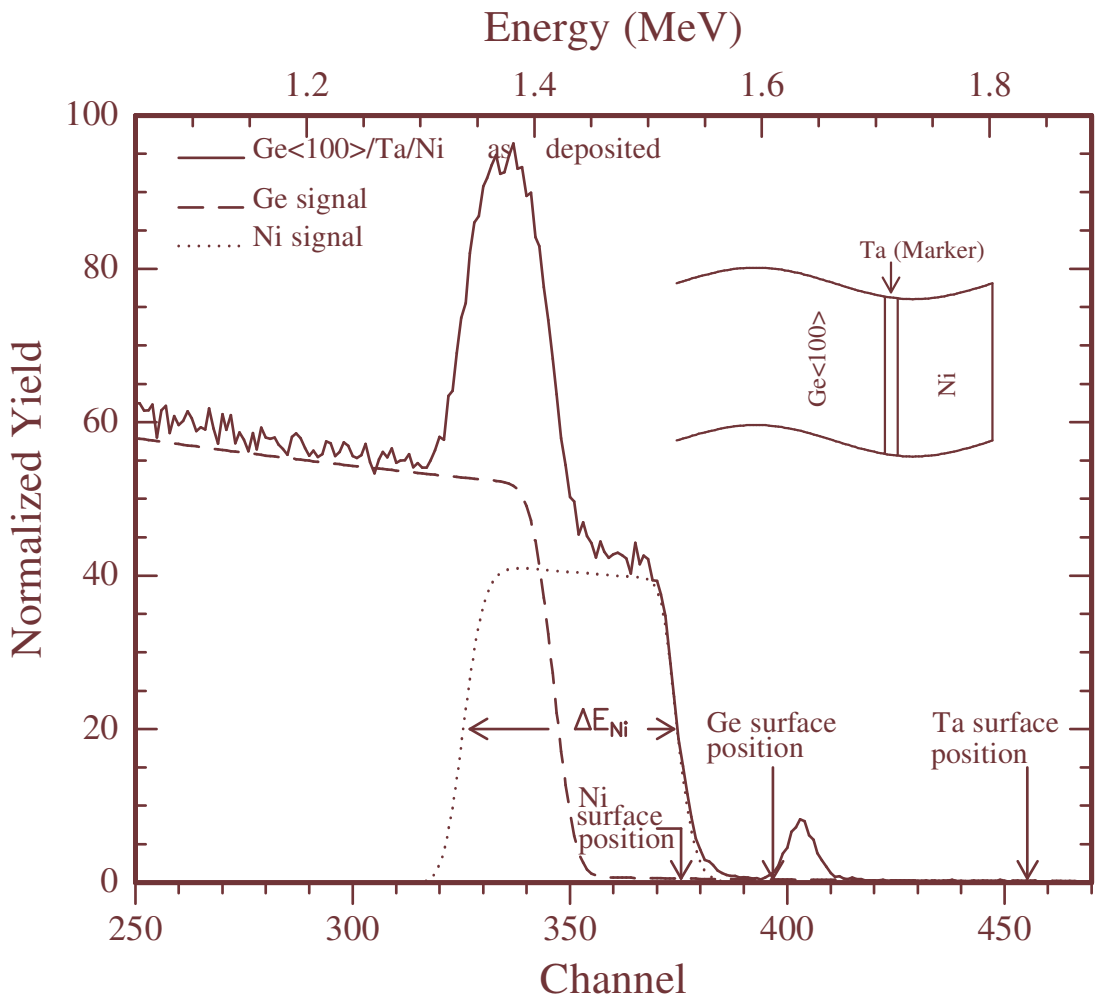

Figure 3.1: 2 MeV ^{4}He+ backscattering energy spectrum from an as-deposited sample formed of a 5 Å thin layer of tantalum electron beam evaporated on a <100>-oriented germanium substrate followed by an 800 Å thick layer of nickel. The simulated contributions of the Ni (dotted line) and Ge (dashed line) signals included in the RBS spectrum are useful in revealing spectral features that might not be immediately apparent. ΔE_{Ni} is the energy difference between the energy of the alpha particles scattered from the Ni atoms at the surface and the energy of the alpha particles scattered from the Ni atoms at the Ni/Ta interface. The insert shows the sample configuration.

It must be emphasized that this peak is not due to the superposition of a peak on a continuous background (as for example an oxygen peak on a silicon background in SiO_2) but from the

overlap of two signals, and that the background at the back is that from Ge, while that in front arises from Ni (and so the background is in no way "continuous").

In general, for surface analysis by RBS conditions must be such that the mass of the surface atoms is considerably higher than the mass of the substrate atoms if the peak arising from the surface atoms is to be completely resolved. Nevertheless, the use of the RUMP program allowed this problem to be circumvented when analyzing our RBS spectra.

3.1.3 Real-Time RBS

For real-time RBS the sample was continuously analyzed with 2 MeV alpha particles while undergoing a ramped thermal anneal from room temperature to 333 ^{o}C. The ramp rate used to anneal the first sample is shown in Fig. 3.2.

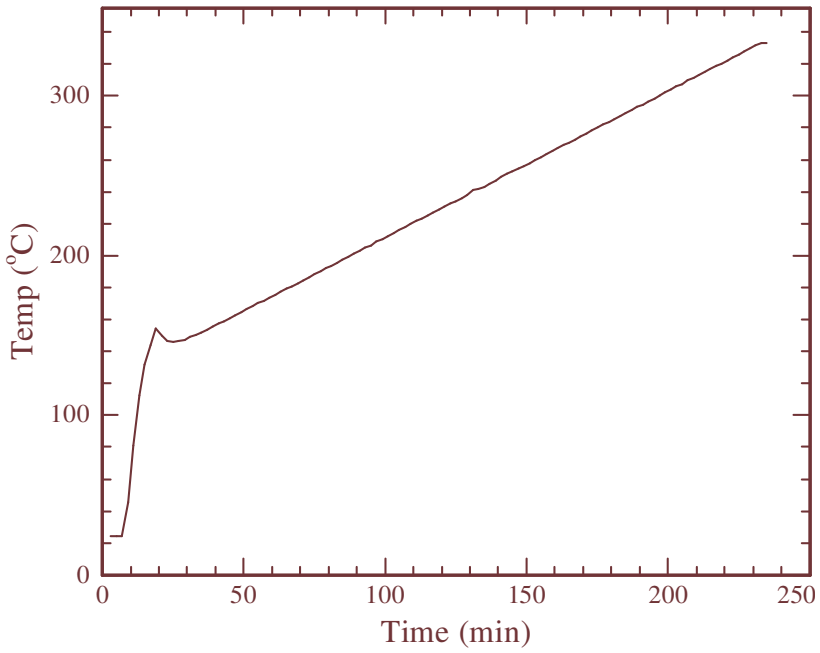

Figure 3.2: Temperature profile during Rutherford Backscattering Spectrometry (RBS) analysis of a sample with configuration Ge<100>/Ta(5 Å)/Ni(800 Å). The sample was initially ramped at a faster rate than 1 ^{o}C/min but between 136 ^{o}C and 333 ^{o}C the ramp rate was maintained at 1 ^{o}C/min. The temperature was then held at 333 ^{o}C for a further 40 minutes to ensure complete germanide formation. This figure does not show the complete temperature profile but only a segment within 250 minutes.

To ensure complete germanide formation the sample was held at 333 °C for a further 40 minutes. During the ramped thermal anneal the chamber pressure, beam current and target temperature were measured every 3 s and the RBS spectra were recorded every 30 s. This resulted in the acquisition of more than three hundred 30-s RBS spectra. To improve the statistics four 30-s RBS spectra were added together to form a composite 2-min RBS spectrum. The four spectra shown in Fig. 3.3 were recorded over a 2 minute period around 240 °C.

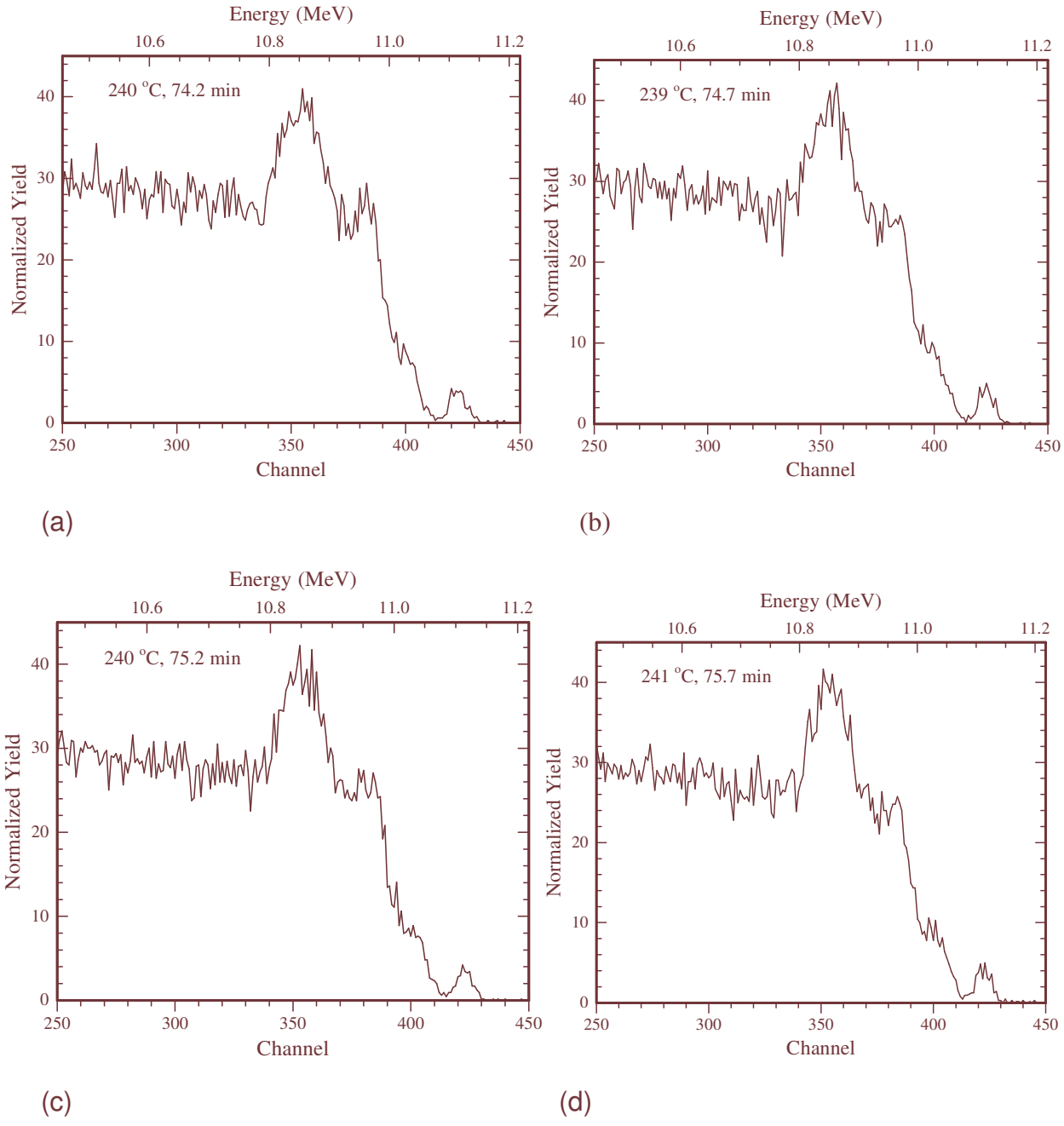

Figure 3.3: 30-s RBS spectra taken around 240 ^{o}C. Although the spectrum in (a) was taken at 240 ^{o}C, 74.2 min, (b) 239 ^{o}C, 74.7 min, (c) 240 ^{o}C, 75.2 min, and (d) 241 ^{o}C, 75.7 min, the four spectra show that very little change has occurred during the 2 minute period.

From Fig. 3.3 (a) to Fig. 3.3 (b) the temperature appears to fall slightly to 239 ^{o}C from 240 ^{o}C over a time interval of 0.5 minutes. The fluctuations in our temperature readings over such small intervals of time were largely a result of noise in the temperature signal sent back to the computer, as a careful scrutiny of the actual temperature measured at the temperature monitor showed that the actual fluctuations in temperature were much smaller, almost nonexistent.

These four spectra in Fig. 3.3 are included here to demonstrate that little change in layer composition occurred during the 2 minutes, as can be seen by making a comparison of the spectra. The composite RBS spectrum of these four 30-s RBS spectra is shown in Fig. 3.4. This spectrum therefore spans a temperature range of 2 ^{o}C.

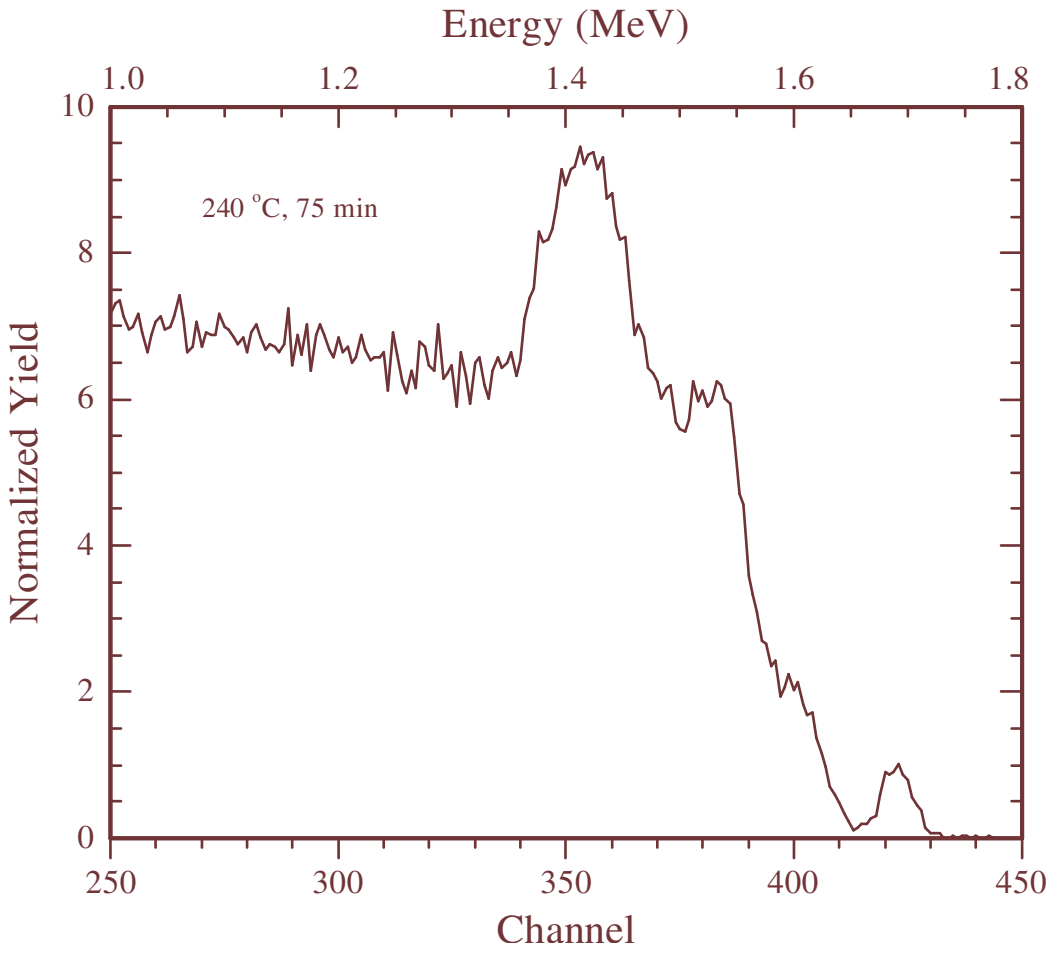

Figure 3.4: A composite 2-min RBS spectrum formed by merging the four 30-s spectra presented in Fig. 3.3.

3.2 First Phase Formation

3.2.1 Sample Configuration

A sample with the configuration Ge<100>/Ta(5 Å)/Ni(800Å) was used to study first phase formation (see insert in Fig. 3.1). The sample was subjected to in situ real-time RBS analysis while undergoing ramped annealing according to the temperature profile given in Fig. 3.2. In the interval 140 – 350 ^{o}C (thermal couple reading) the ramp rate was maintained at 1^{o}C/min.

3.2.2 First Phase Marker Results

The in situ, real-time RBS results acquired from the sample with configuration Ge<100>/Ta(5 Å)/Ni(800 Å) revealed that the reaction commenced around 145 ^{o}C with the formation of the Ni_5Ge_3 phase. At a later stage of the annealing, even before all the Ni had been completely consumed, the second phase started growing. This second phase was identified to be NiGe and its formation was detected at around 170 ^{o}C. The growth and decomposition of the Ni_5Ge_3 and NiGe phases together with the consumption of Ni are presented in Fig. 3.5.

Although the growth of phases in thin film solid state reactions is known to be sequential in which one phase grows before another phase can start to grow, Fig. 3.5 demonstrates an unusual simultaneous growth of the Ni_5Ge_3 and NiGe phases in the presence of unreacted Ni. The simultaneous growth of Ni_5Ge_3 and NiGe lasts from the onset of the growth of the latter phase until 243 ^{o}C. During this period the two phases can be seen to grow together. It can be seen from Fig. 3.5 that the thickness of the Ni_5Ge_3 phase increases in what appears to be a parabolic manner from its nucleation until the time it started to decompose. On the other hand Fig. 3.5 also shows that the formation of NiGe is characterized by a change in the growth rate. The growth rate of NiGe is very similar to that of Ni_5Ge_3 when there is simultaneous growth because during this period the thicknesses of both phases appear to be increasing quadratically. For some unknown reasons the NiGe phase was forced to start decomposing at 245 ^{o}C when it had reached a thickness of 189×10^{15} at/cm^2. The NiGe continued to decompose from 245 ^{o}C up to 272 ^{o}C where its thickness had dropped to about 54×10^{15} at/cm^2 and then it maintained this thickness until the total consumption of Ni at around 298 ^{o}C. In Fig. 3.5, the thickness to which the NiGe phase dropped before it stopped decomposing appears far less than 54×10^{15} at/cm^2 because the plotted thicknesses are normalized to the number Ni atoms present in each phase (i.e., the actual thickness divided by two for the NiGe phase). From this temperature until the end of the reaction, the NiGe phase resumed its growth at a much faster growth rate while the Ni_5Ge_3 was consumed.

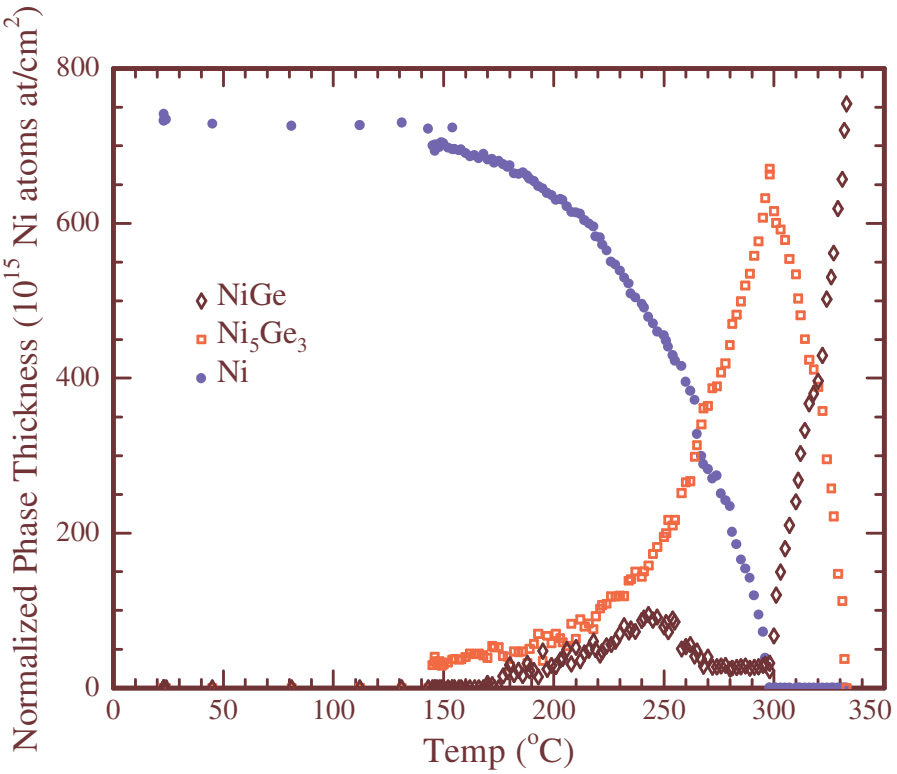

Figure 3.5: Germanide compound phase formation during ramped temperature induced reaction of nickel with germanium in a sample with configuration Ge<100>/Ta(5 Å)/Ni(800 Å) showing the individual phases present from 23 ^{o}C to 333 ^{o}C. The simultaneous growth of Ni_5Ge_3 and NiGe in the presence of unreacted nickel can clearly be seen from 170 ^{o}C until the Ni_5Ge_3 phase started to decompose at 298 ^{o}C.

The temperature was held constant at 350 ^{o}C (thermocouple reading) for a further 40 min but no new phases were observed. Fig. 3.5 demonstrates that the in situ real-time RBS data allow a quantitative analysis of the germanide thin film growth. Both reactions, i.e. the formation of Ni_5Ge_3 and the formation of NiGe, can be distinguished and contain enough data points for each of the phases which allows for the growth of each of the phase to be characterized. The RBS spectra presented in Fig. 3.6 were acquired at five selected stages of the solid state reaction during the in situ real-time RBS measurement and they show the composition of the sample at each of these stages of the reaction.

These spectra were selected to illustrate the spectrum of the sample as it was deposited at room temperature (RT), the spectrum at the beginning of Ni_5Ge_3 growth around 145 ^{o}C, the onset of

NiGe formation around 170 °C, the stage at which all the Ni was totally consumed and the spectrum at the end of the reaction at 333 °C.

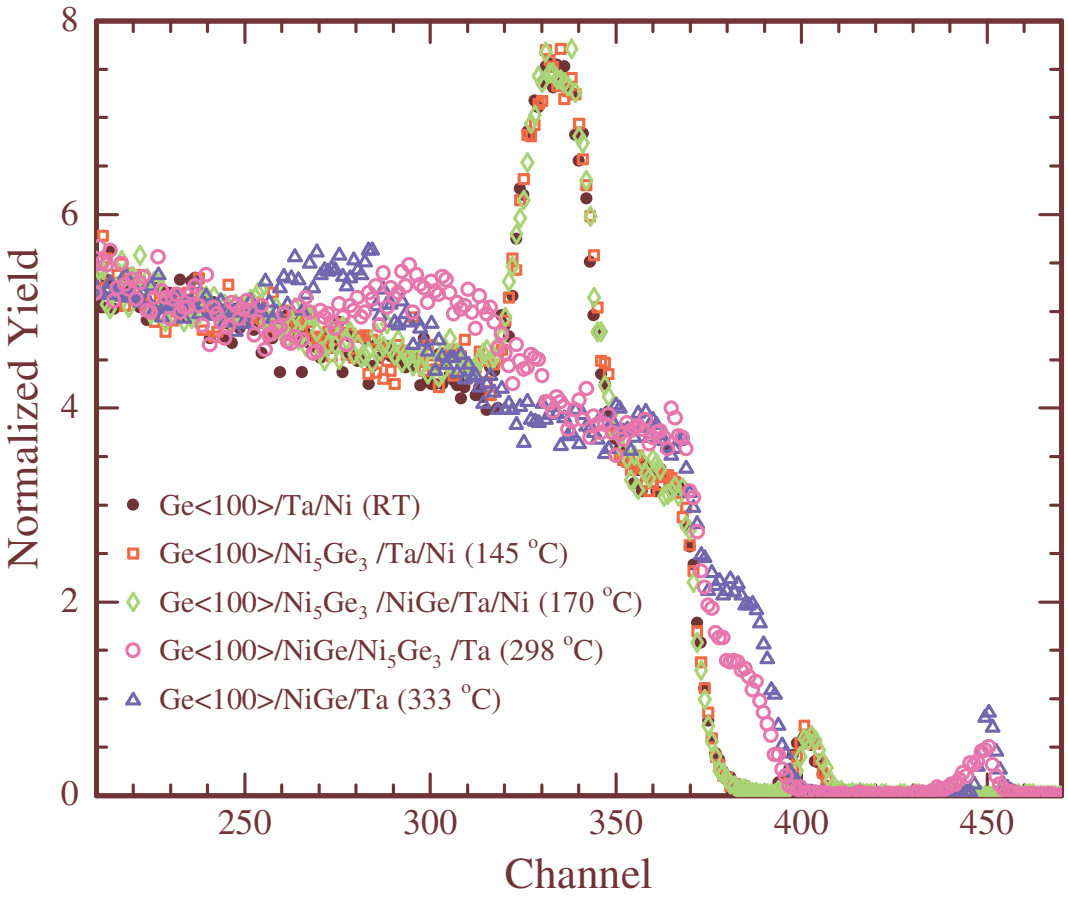

Figure 3.6: Selected RBS spectra acquired during the real-time RBS measurement of an 80 nm thin Ni film on Ge<100> at several stages of the solid-phase reaction, i.e. as deposited (at RT, solid circles), during the onset of Ni_5Ge_3 growth (at 145 °C, squares), during the onset of NiGe formation (at 170 °C, diamonds), when all the surface Ni is totally consumed (298 °C, open circles) and the spectrum at the end of the reaction (at 333 °C, triangles).

In Fig. 3.6 the spectrum of the virgin (as-deposited) sample, the spectrum taken at the start of Ni_5Ge_3 growth and the one captured around the onset of NiGe growth almost overlap. However, careful examination of the Ta marker signal in these three spectra reveals a slight displacement of the Ta signals towards higher channels which indicates that the reaction had already started taking place. The spectra in Fig. 3.6, except the spectrum taken when all the Ni was totally

consumed, are presented individually in Fig. 3.7 corroborated by their RUMP simulations to show agreement between the measured and calculated (simulated) spectra.

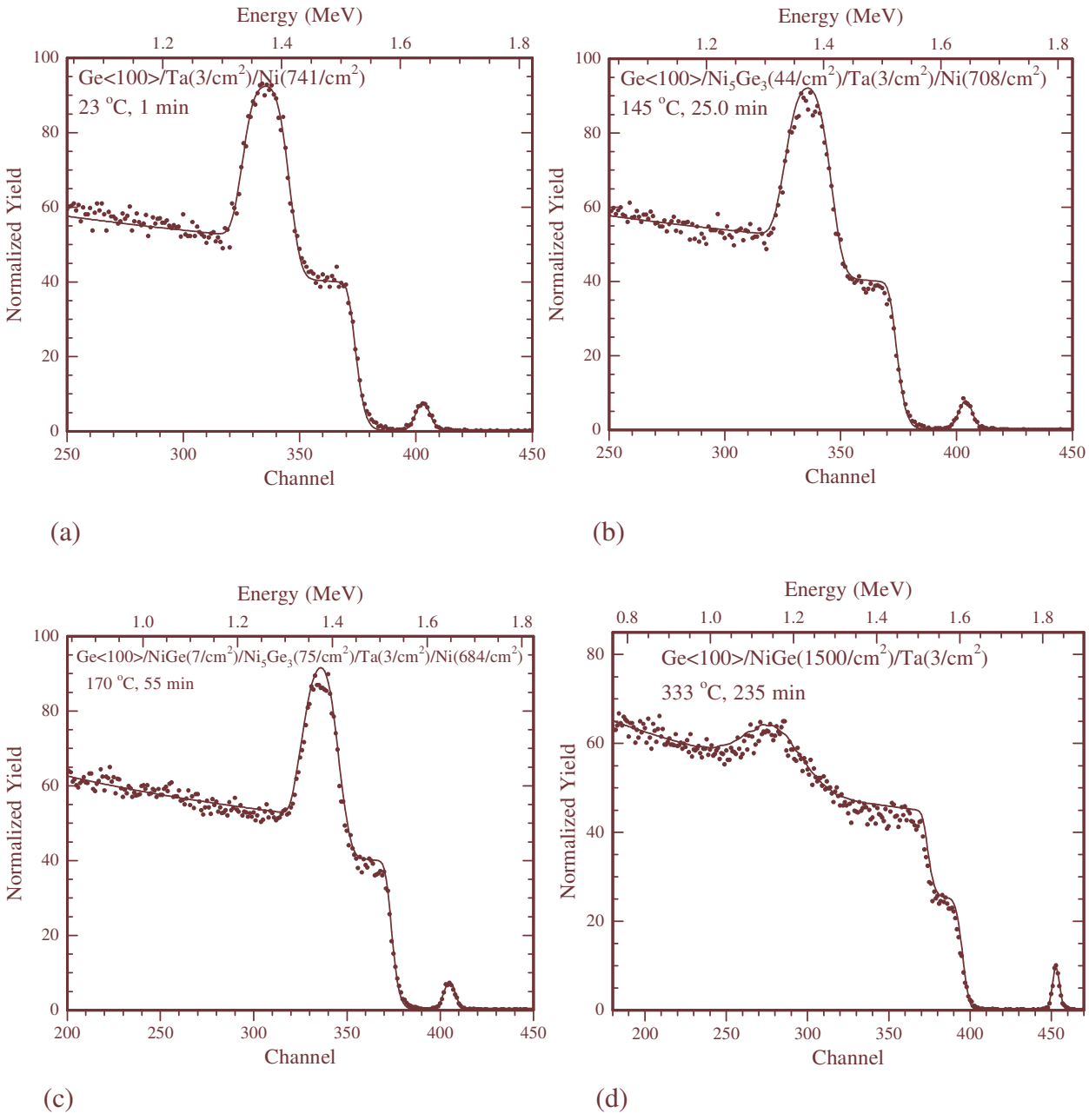

Figure 3.7: The spectra in Fig. 3.6, except the spectrum illustrating the total consumption of Ni, corroborated by their RUMP simulations. The spectrum in (a) is from the as-deposited sample, (b) shows the onset of Ni_5Ge_3 formation, (c) shows the onset of NiGe formation and (d) is the spectrum taken at the end of the reaction. The temperature and time period of annealing at which each spectrum was taken are also indicated. The thicknesses are in units of 10^{15} atoms/cm^2.

The RUMP simulation of the spectrum illustrating the sample at the end of the reaction (Fig. 3.7 (d)) indicates that all the Ta atoms diffused to the surface of the sample resulting in an interlayer inversion between the Ni which was initially at the surface of sample and the Ta which was initially buried beneath the Ni atoms.

By adding a third dimension, time (or temperature) it is possible to represent the spectra for the complete reaction as a single three dimensional plot. Since temperature was held constant at 333 ^{o}C for several minutes, the time was chosen as the third dimension for the 3-D plot presented in Fig. 3.8.

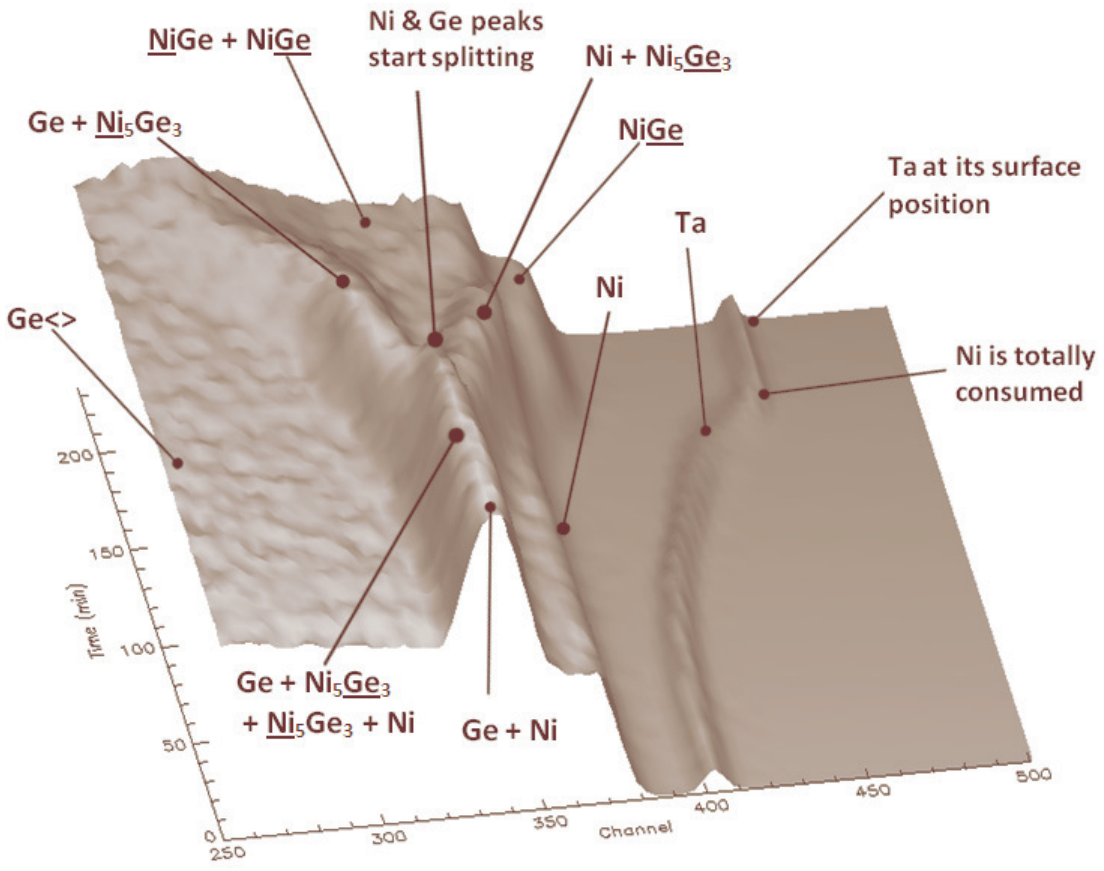

Figure 3.8: In situ, real-time RBS spectra of the formation of Ni_5Ge_3 and NiGe on Ge<100> substrate during ramped thermal annealing from room temperature to 333 ^{o}C. The Ta marker

embedded between the Ge<100> and the Ni layer shifts to higher channels (or energies) during the formation of both phases.

In Fig. 3.8 various features constituting the 3-D plot together with the different atomic species leading to the formation of these features are indicated. The progressive shift of the Ta marker signal towards higher energies throughout the reaction from its initial position at channel 403.1 (or 1.636 MeV) to the position where it finally stops moving around channel 450 (or 1.82 MeV) is also clearly visible in the 3-D plot given in Fig. 3.8. It can be seen from Figure 3.8 that before the point where the Ni and Ge peaks start splitting there is only one single peak forming the highest ridge in the 3-D plot but after this point the peak splits forming two ridges with one ridge moving to the left while the other moves to the right.

The two individual spectra presented in Fig. 3.9 have been included in order to explain how the splitting of peaks forming the two ridges moving in opposite directions comes about.

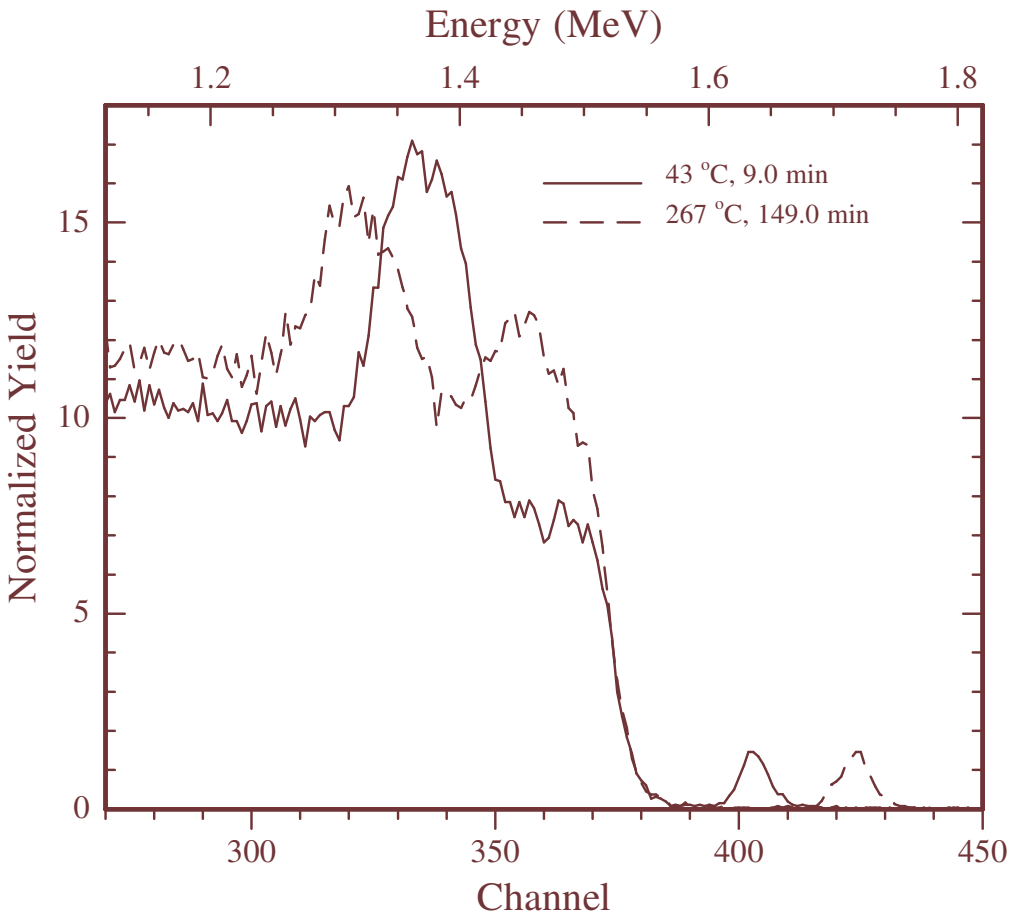

Figure 3.9: In situ, real-time RBS showing a spectrum captured before the splitting of Ni and Ge peaks (solid Line) and another spectrum captured after splitting of the peaks (dashed line).

These spectra were captured during the run at very different stages of the reaction, namely the spectrum captured at 43 ^{o}C (which is very similar in form to the spectrum in Fig. 3.1 since the reaction had not yet commenced at this temperature) and the one captured at a temperature of 267 ^{o}C. The single peak in the spectrum captured at 43 ^{o}C (solid line) arises from the overlap of the Ni and Ge signals as explained in section 3.1.2. As the reaction progresses the Ni moves deeper into the sample making the layer of Ni above the Ta marker thinner.

Since Ge has higher atomic mass than Ni, the thinning of the Ni layer above the Ta causes the Ge in the growing germanides to appear at higher channels while the Ni in the growing germanides appear at lower channels. This results in the splitting of the peak into two peaks which are clearly visible in the 267 ^{o}C spectrum. The spectrum captured at a temperature of 267 ^{o}C is again

presented in Fig. 3.10 with simulated contributions of the Ni (dashed line) and the Ge (dotted line) signals to illustrate how the splitting of the peaks occurs.

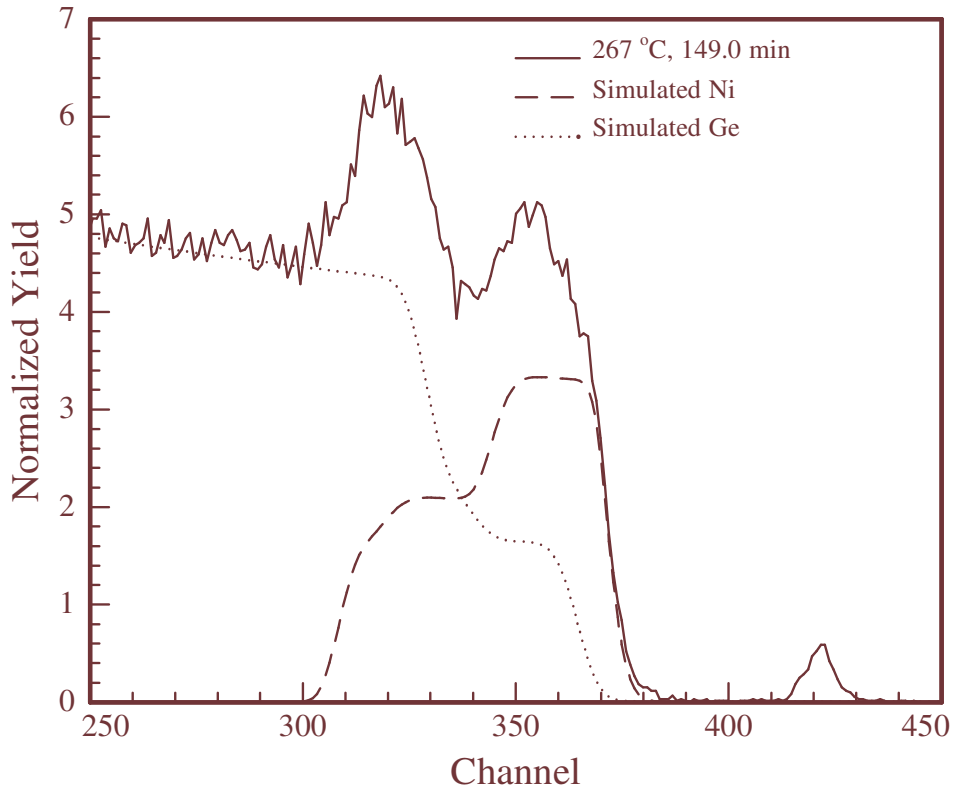

Figure 3.10: In situ, real-time RBS showing a spectrum captured at around 267 °C after the splitting of Ni and Ge peaks had already begun. The simulated contributions of the Ni (dashed line) and Ge (dotted line) signals to this spectrum are also included.

The kink in the leading (front) edge of the Ge signal represents the Ge atoms in the growing germanides while the kink in the back edge of the Ni signal represents the Ni atoms in the growing germanides. Therefore, the peak on the left in Fig. 3.10 arises from the overlap of the Ni atoms in the growing germanides and the Ge atoms in the substrate while the peak on the right arises from the overlap of the Ge in the growing germanides and the unreacted surface Ni. Figure 3.10 is especially useful to gain an intuitive feeling for complex overlapping spectra.

A comparison of the positions of the front edge of the simulated Ge signal and the back edge of the simulated Ni signal in Fig. 3.1 with the positions of these edges in Fig. 3.10 reveals that these edges have moved to higher and lower channels (or energies) respectively. By using the splot

command of the RUMP code it was possible identify the contributions of Ni and Ge atoms to the various features appearing in Fig. 3.8.

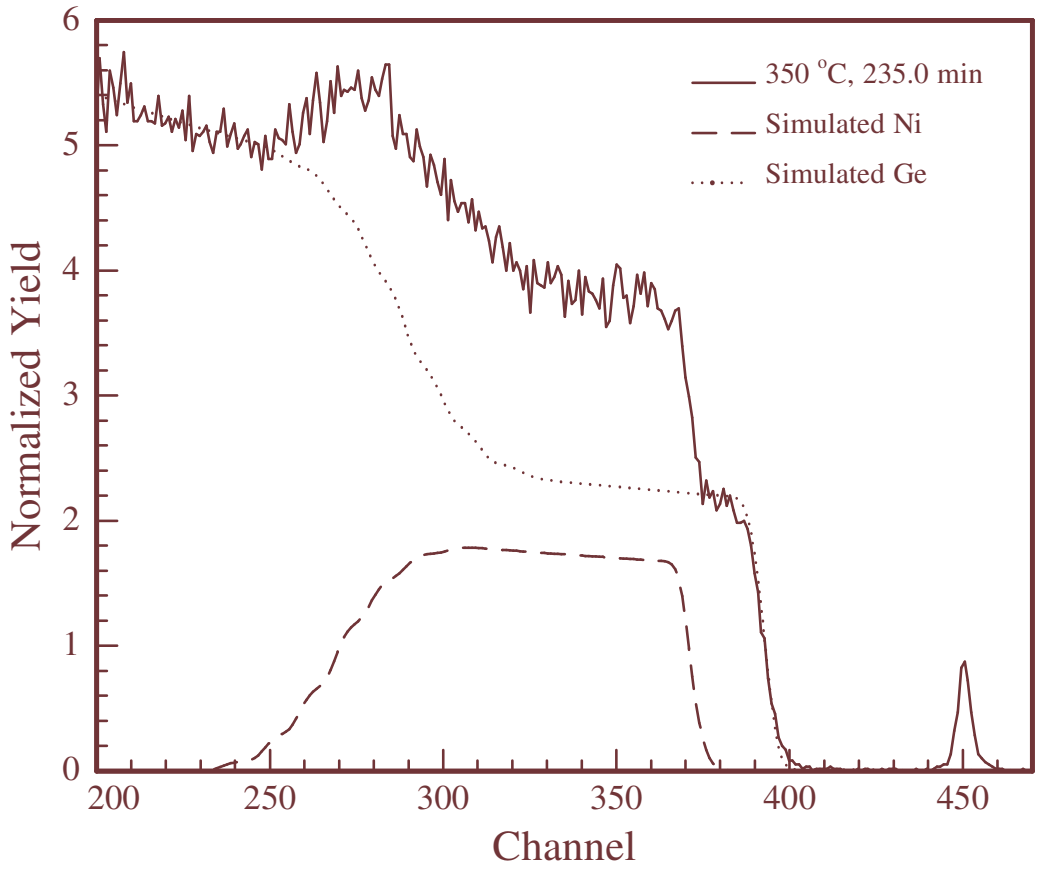

Figure 3.11: In situ, real-time RBS showing a spectrum captured at around 350 °C (thermocouple temperature) illustrating how the feature labeled Ni<u>Ge</u> in Fig. 3.8 is produced.

The atomic species which are responsible for the formation of the various features identified in Fig. 3.8 are all indicated. In the case where the atomic species is part of a compound this is indicated by underlining the element. Thus, the underlined element such as Ge in Ni<u>Ge</u> shows that the indicated feature results from the Ge in the NiGe phase. Similarly a feature indicated as Ge + $\underline{Ni}_5Ge_3$ shows that this feature results from the overlap of Ge in the substrate and Ni in the Ni_5Ge_3 phase. The spectrum in Fig. 3.11 was taken at 350 °C (thermocouple reading) and is very useful in illustrating how the feature labeled Ni<u>Ge</u> in Fig. 3.8 is produced. This plot shows that at this stage of the reaction the Ni signal is entirely under the Ge signal with the leading edge of the Ni signal well behind the leading edge of the Ge signal. Therefore the feature labeled Ni<u>Ge</u> in Fig. 3.8 results solely from the Ge in the NiGe phase. The 3-D plot presented in Fig. 3.8 is

therefore a graphical illustration of the complex overlap of the Ni and Ge signals that occur at different stages of the solid state reaction in the Ni/Ge system.

3.2.3 Discussion

The first phase marker results have shown that only two phases form in the Ni/Ge binary system. The phase that formed first during the solid state reactions of Ni and Ge was found to be Ni_5Ge_3 and the growth of this phase started around 145 ^oC. The second and final phase was found to be NiGe and its growth started around 170 ^oC. The results further show an unusual simultaneous growth of the Ni_5Ge_3 and NiGe phases in the presence of unreacted Ni. This simultaneous growth of the two phases lasted from the onset of the formation of the NiGe phase until 245 ^oC when the NiGe phase had reached a maximum thickness of 189×10^{15} at/cm^2 (actual thickness). The NiGe phase then started to decompose at 245 ^oC. The decomposition of the NiGe phase between 245 ^oC and 272 ^oC observed in Fig. 3.5 was rather strange and the reason for this behavior is not very clear but it could probably have resulted from a phase competition between the Ni_5Ge_3 and NiGe phases which favored the growth of the former phase more than the latter phase. It is equally not very clear why the NiGe maintained an almost constant thickness of about 54×10^{15} at/cm^2 (actual thickness) in the temperature window between 272 ^oC and 298 ^oC instead of decomposing completely. The NiGe phase was observed to resume its growth with a very rapid growth rate after all the Ni was totally consumed around 298 ^oC. This rapid growth resulted from the thermal dissociation of the Ni_5Ge_3 phase. Since the Ni_5Ge_3 phase did not stop growing during the interval from the onset of NiGe formation to the stage where the NiGe started to decompose, the growth of NiGe in this interval (170-243 ^oC) must have been as a result of the reaction of the diffusing Ni atoms with the Ge atoms in the substrate.

The formation of phases during solid state reactions in the thin film regime is known to be sequential where one phase grows at a time. Although typically not observed for thin film reactions, our results from the first sample have demonstrated a rather an uncommon behaviour for thin film phase formation in which a simultaneous growth of Ni_5Ge_3 and NiGe in the presence of unreacted Ni was observed at a later stage of the reaction. This unusual simultaneous growth of these two phases has also been reported by Gaudet et al. [79] and Nemouchi et al. [72, 72, 83]. There is a concept of a critical thickness associated with the growth of phases in thin films. A critical thickness is defined as the thickness which one phase must reach before another

phase becomes thermodynamically favored. According to Nemouchi et al. [72] the observed simultaneous growth seems to manifest due to the low critical thickness of Ni_5Ge_3 as well as the different control of the growths of the Ni_5Ge_3 and NiGe phases during heat treatment. Nemouchi et al. [71] further noted that the switch from a sequential to a simultaneous growth during thin film reaction might be important for industrial applications where a unique phase with specific properties is needed.

It was observed from Fig. 3.6 that the virgin spectrum (as-deposited), the spectrum taken at the start of Ni_5Ge_3 growth and the spectrum captured around the onset of NiGe growth almost overlap. The spectra up to these three stages of the solid state reaction appear almost the same because so far only very little of the surface Ni is consumed in the formation of Ni_5Ge_3 and NiGe. This means that the amount of Ni and Ge in these compounds is equally small so that the overall shape of each of the three energy spectra is predominantly due to the overlap of the unreacted surface Ni and the Ge in the substrate. However, it can be seen from the spectrum illustrating the total consumption of Ni and the spectrum at the end of the reaction that the shape of the energy spectra changes markedly as the surface Ni becomes thinner and as the amount of Ni and Ge in the grown compounds increase. As a result of this thinning of the Ni layer above the Ta the Ge in the growing germanides appear at higher channels or energies while the Ni in the growing germanides appear at lower channels or energies which finally cause the splitting of the Ni and Ge peaks (Fig. 3.10).

It must also be noted that the Ta signals in the spectrum captured when the Ni is totally consumed and the one at the end of the reaction overlap because at this stage of the reaction all the Ta has now moved to the surface of the sample. This resulted in an interlayer inversion between the Ni which was initially at the surface of sample and the Ta which was initially buried beneath the Ni atoms.

Although the temperature was held constant at 350 ^{o}C (thermocouple reading) for a further 40 min, there were no new phases observed. This indicates that NiGe is the last germanium rich phase that forms during the solid phase reaction (SPR) of Ni with Ge which is in agreement with the Ni-Ge binary equilibrium phase diagram (see Fig. 1.7) where NiGe is predicted as the last and most Ge-rich phase to form in the Ni/Ge system.

According to the Walser and Bené (W-B) rule [16], which was later generalized as a metal-covalent rule for phase selection, the first compound nucleated in planar binary reaction couples is the most stable congruently melting compound adjacent to the lowest-temperature eutectic in the bulk equilibrium phase diagram. For the Ni-Ge system the most stable congruently melting compound adjacent to the lowest-temperature eutectic in the bulk equilibrium phase diagram (see Fig. 1.7) is Ni_2Ge. Therefore, the W-B rule predicts Ni_2Ge as the first nucleating phase in the Ni-Ge system. The identification of Ni_5Ge_3 as the first phase in the present study therefore violates the W-B rule.

The identification of Ni_5Ge_3 as the first phase for the Ni-Ge system in our study is in agreement with the results of Nemouchi et al. [71, 72, 83] who also reported the simultaneous growth of the Ni_5Ge_3 and the NiGe although the latter phase was found to have occurred during deposition in their study. The identification of the Ni_5Ge_3 as the first phase is also in agreement with the results of Gaudet et al. [79] who observed the same phase near an annealing temperature of 170 ^oC. Their study further reported the simultaneous growth of the Ni_5Ge_3 and the NiGe phases on both α-Ge and Ge(001) but they found the growth of the two phases to appear consecutively on Ge(111). Our results are further in agreement with the results of Patterson et al. [81] who also found Ni_5Ge_3 to be the first nucleating phase in the Ni/Ge system. Studies by Mueller et al. [66] identified Ni_5Ge_3 and Ni_2Ge as the metal-rich phases that formed below 350 ^oC while they found NiGe to dominate starting from this temperature. Their results are therefore in agreement with our results as regards the formation of Ni_5Ge_3 as the first phase. Nevertheless, their results disagree with our results on the formation of Ni_2Ge since we did not observe this phase during the analysis of our RBS data. The other results that disagree with our observation of Ni_5Ge_3 as the first nucleating phase include those reported by Marshal et al. [67], Hsieh et al. [13] and those by Wittmer et al. [80] who all identify Ni_2Ge as the first phase as well as the results by Jin et al. [64] who found Ni_3Ge_2 to be first phase.

The progressive movement of the Ta marker towards higher energies observed in Fig. 3.8 indicates that during the formation of the Ni_5Ge_3 and the NiGe phases all the Ni is being supplied by direct diffusion through the Ta to the substrate. The appearance of Ta at surface of the sample shows that during the formation of both Ni_5Ge_3 and NiGe phases the reaction takes place entirely below the Ta marker.

It has been shown that there is excessive overlapping of the Ni and Ge peaks in the Ni/Ge system. However, by using the RBS technique and the splot command of the RUMP code we were able to identify the different features appearing in the 3-D plot presented in Fig. 3.8. The characterization of the growth of thin Ni_5Ge_3 and NiGe films on Ge<100> substrates using ramped thermal annealing has demonstrated the applicability of in situ, real-time RBS and the RUMP code as powerful tools for studying solid state interaction in thin film binary diffusion couples such as the Ni/Ge system.

3.3 Second Phase Formation

3.3.1 Sample Configuration

The marker results obtained during the formation of the Ni_5Ge_3 phase show that the Ta marker was subsequently rendered useless as a tool for monitoring the direction of atomic mobility during the NiGe phase formation. This is so because the marker moved towards and reached the surface of the sample during the first phase formation process. Therefore, the NiGe phase formation took place below the marker. Under these conditions the signal of the Ta marker could no longer monitor the direction of atomic mobility (i.e. the Ta ceased to function as a marker) and the sample configuration had to be changed. In order to determine the dominant diffusing species during NiGe formation we need a configuration which allows the system to form the first phase, Ni_5Ge_3, above the Ta marker without nickel atoms diffusing past the marker. The configuration therefore adopted to monitor diffusion during second phase formation is shown in Fig. 3.12 below. The actual structure of this sample was Ge<100>/Ta(6 Å)/Ge(490 Å)/Ni(470 Å). This sample configuration was chosen in such a way that all the amorphous germanium atoms above the marker would be completely consumed during the formation of the first phase but with some unreacted Ni atoms still remaining above the marker.

Once the Ge above the marker is totally consumed in the formation of the first phase two situations can arise. One possibility is that the excess Ni atoms remain immobile while the Ge atoms in the substrate diffuse past the Ta marker to react with the excess Ni atoms. The other possibility is for the Ge atoms in the substrate to remain immobile while the excess Ni atoms diffuse past the Ta marker and react with the Ge atoms in the substrate. It is also possible to have a situation where the two possibilities to take place together. However, on the basis of the first

marker results the excess Ni atoms are expected to diffuse past the Ta marker and react with the Ge atoms in the substrate because the observed motion of the Ta marker towards the surface of the sample implies the diffusion of Ni.

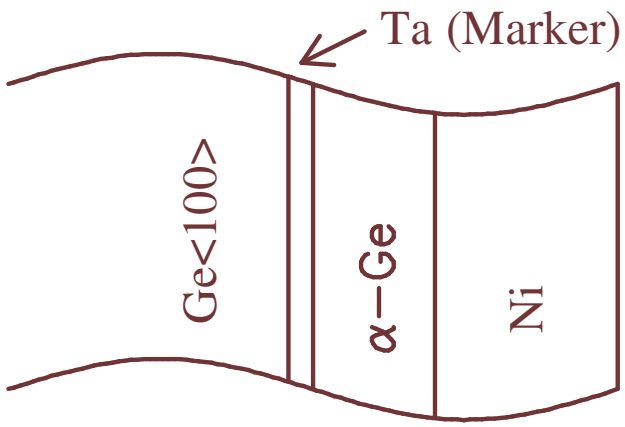

Figure 3.12: Sample configuration adopted to force the formation of Ni_5Ge_3 above the Ta marker without the Ni diffusing past the marker to the substrate. The amount of Ni deposited was such that it would react with all the α-Ge above the marker but with excess Ni remaining after all the Ge above marker has been completely consumed in the formation of Ni_5Ge_3.

3.3.2 Second Phase Marker Results

In situ, real-time RBS data for the sample described in section 3.2.1 were acquired by continuously analyzing the sample while it was simultaneously subjected to linear thermal annealing to induce phase formation. The temperature profile showing the ramp rates at which thermal annealing of the sample was carried out from room temperature to 333 ^{o}C is presented in Fig. 3.13.

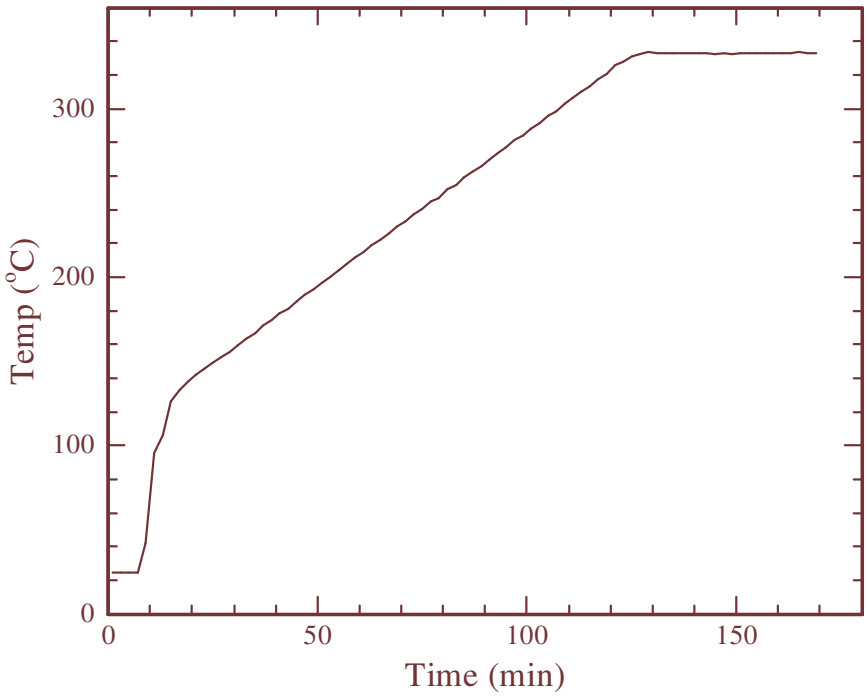

Figure 3.13: Temperature profile during RBS analysis for a sample with configuration Ge<100>/Ta(6 Å)/Ge(490 Å)/Ni(470 Å). The sample was initially ramped at a faster rate than 1°C/min but between 136 °C and 333 °C the ramp rate was maintained at 1 °C/min. The temperature was then held at 333 °C for a further 40 minutes to ensure complete germanide formation.

The in situ real-time RBS data of the observed nickel germanides phase formation sequence during the solid state reaction of nickel with germanium in the sample described in section 3.3.1 is presented diagrammatically in Fig. 3.14. The thicknesses of the germanides in Fig. 3.14 are all expressed in terms of the number of Ni atoms present in each compound phase. It can be seen from Fig. 3.14 that there is a room temperature reaction of germanium with nickel to form the metal-rich Ni_5Ge_3 since the phase formation graph for Ni_5Ge_3 starts at 23 °C which was our room temperature. Like in the sample without Ge above the Ta, the thickness of the Ni_5Ge_3 phase can be seen to increase in what appears to be a parabolic manner from the time its growth started until the total consumption of germanium above the Ta marker around 239 °C. The Ni_5Ge_3 phase then stopped growing for a brief period in the interval between 240-250 °C (Fig. 3.14). After 250 °C the Ni_5Ge_3 phase started to dissociate. The dissociation or consumption of Ni_5Ge_3 results from either or both of the two possible mechanisms, $Ni_5Ge_3 \rightarrow 3NiGe + 2Ni$ or $Ni_5Ge_3 + 2Ge \rightarrow 5NiGe$.

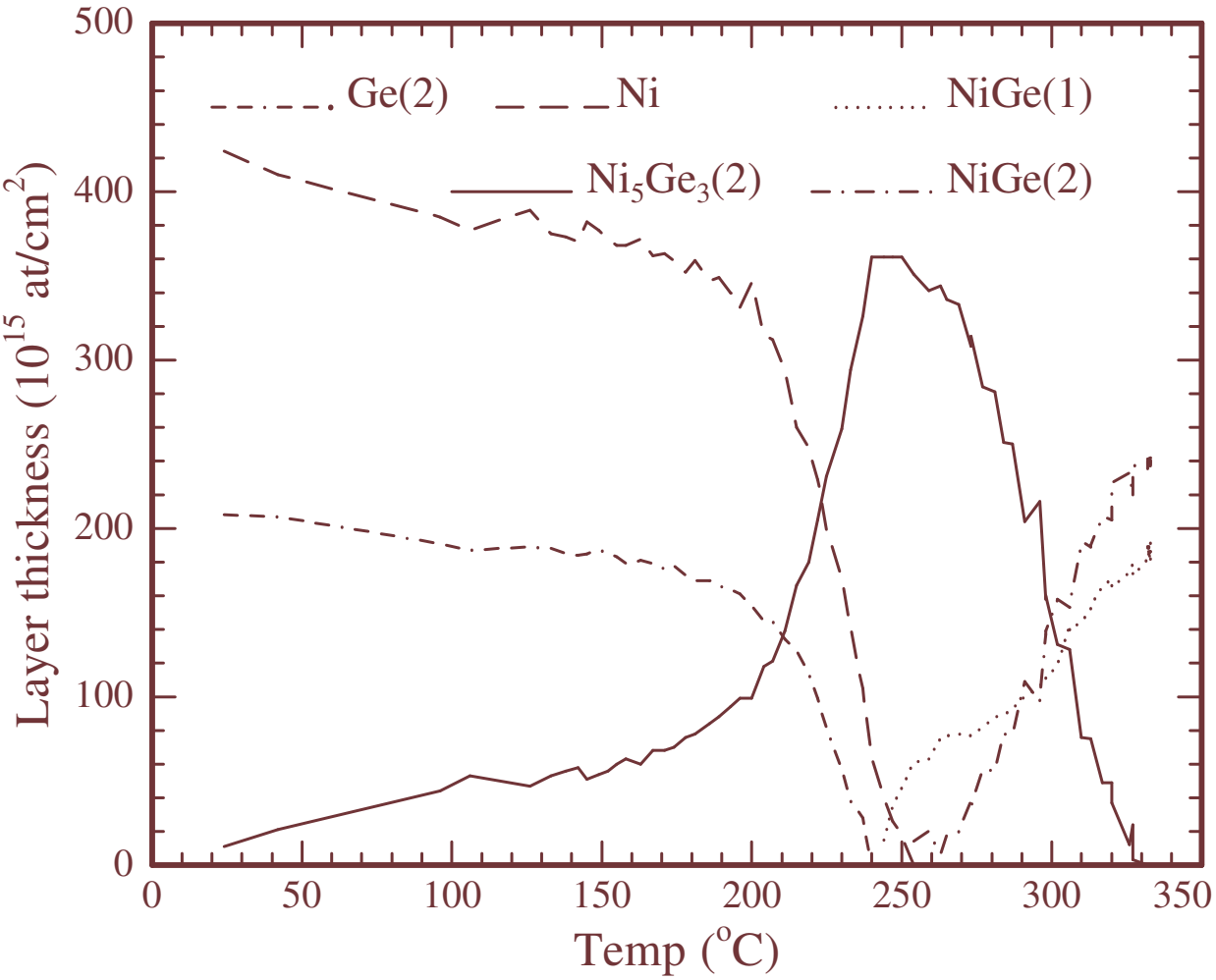

Figure 3.14: Nickel germanides phase formation during ramped temperature induced reaction of nickel with germanium showing individual phase evolution below and above the Ta marker. The digits 1 and 2 in brackets refer to phases formed below and above the marker respectively.

When the germanium above the marker was completely consumed in the formation of Ni_5Ge_3, the excess Ni started diffusing to the substrate. On diffusing to the substrate, the unreacted Ni atoms go straight into the formation of NiGe below the marker by the reaction Ni + Ge → NiGe skipping the formation of another layer of the Ni_5Ge_3 phase. The growth of NiGe below the Ta marker started around 239 ^{o}C. This layer of NiGe below the marker does not stop growing even after the unreacted nickel above the marker is completely consumed. When all the Ni was totally consumed, the Ni_5Ge_3 started to decompose through either or both of the mechanisms described

earlier to form another layer of NiGe above the Ta which started around 249 ^{o}C. These two layers of NiGe are summed up and plotted as the total NiGe growth in Fig. 3.15. Again, the thicknesses of the germanides in Fig. 3.15 are all expressed in terms of the number of Ni atoms present in each compound phase.

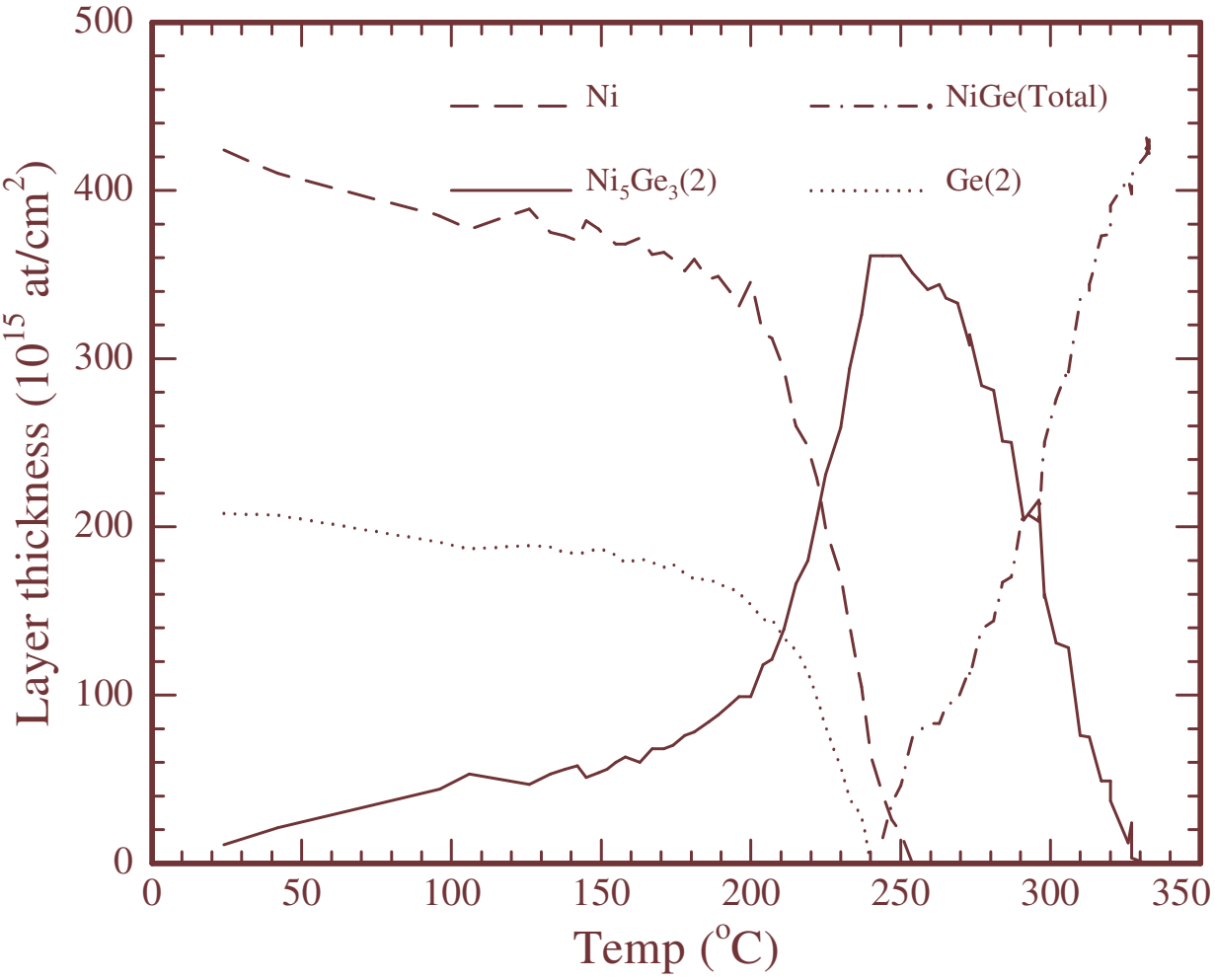

Figure 3.15: Germanide compound phase formation during ramped temperature induced reaction of nickel with germanium showing the total growth of the NiGe phase. The digit 2 in brackets refers to the compound formed above the Ta marker.

The spectrum of the sample before the start of the reaction (as-deposited) and the spectrum at the end of the reaction are presented in Fig. 3.16 (a) and (b) respectively. The measured spectra in

Figs. 3.16 (a) and (b) are supported by their RUMP simulations to show agreement with the actual data.

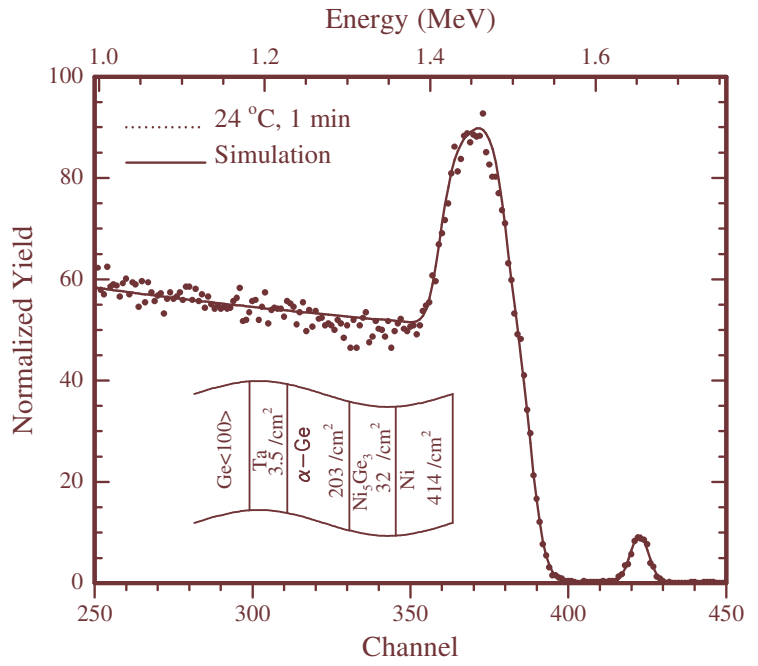

(a)

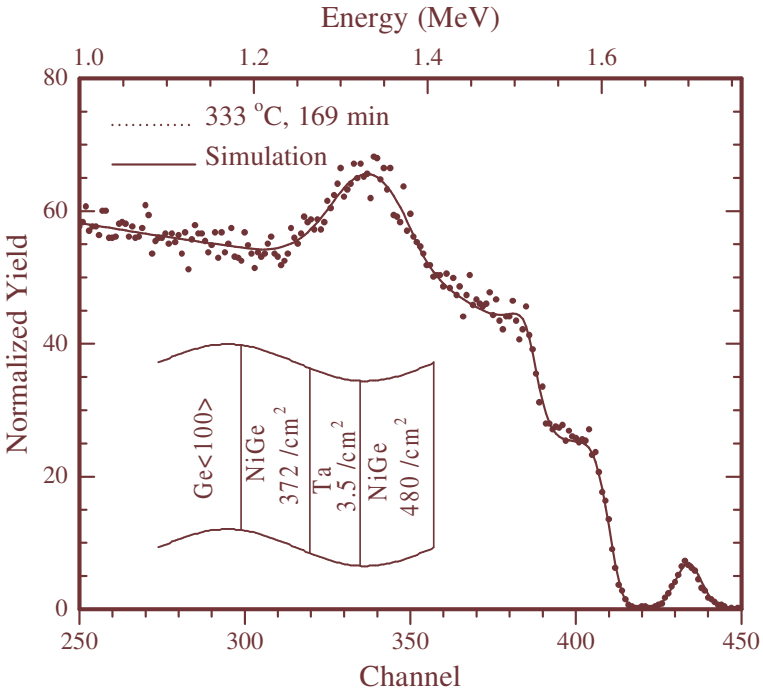

(b)

Figure 3.16: Measured spectrum (dotted line) and its RUMP simulation (solid line) depicting the sample (a) in its as-deposited (or virgin) state and (b) at the end of the reaction respectively. The thicknesses are in units of 10^{15} atoms/cm^2. (b)

According to the RUMP simulation shown in Fig. 3.16 (a) the as-deposited sample contains about 215×10^{15} atoms/cm^2 of Ge above the marker; that is 203×10^{15} atoms/cm^2 in unreacted Ge above the Ta and 12×10^{15} atoms/cm^2 in the 32×10^{15} atoms/cm^2 Ni_5Ge_3 layer.

The spectrum of the sample at the end of the reaction (end spectrum) given in Fig. 3.16 (b) shows the presence of about 480×10^{15} atoms/cm^2 of NiGe above the Ta marker. There is therefore 240×10^{15} atoms/cm^2 of Ge in this layer of NiGe. The end spectrum therefore has 25×10^{15} atoms/cm^2 more Ge than was initially deposited above the Ta marker.

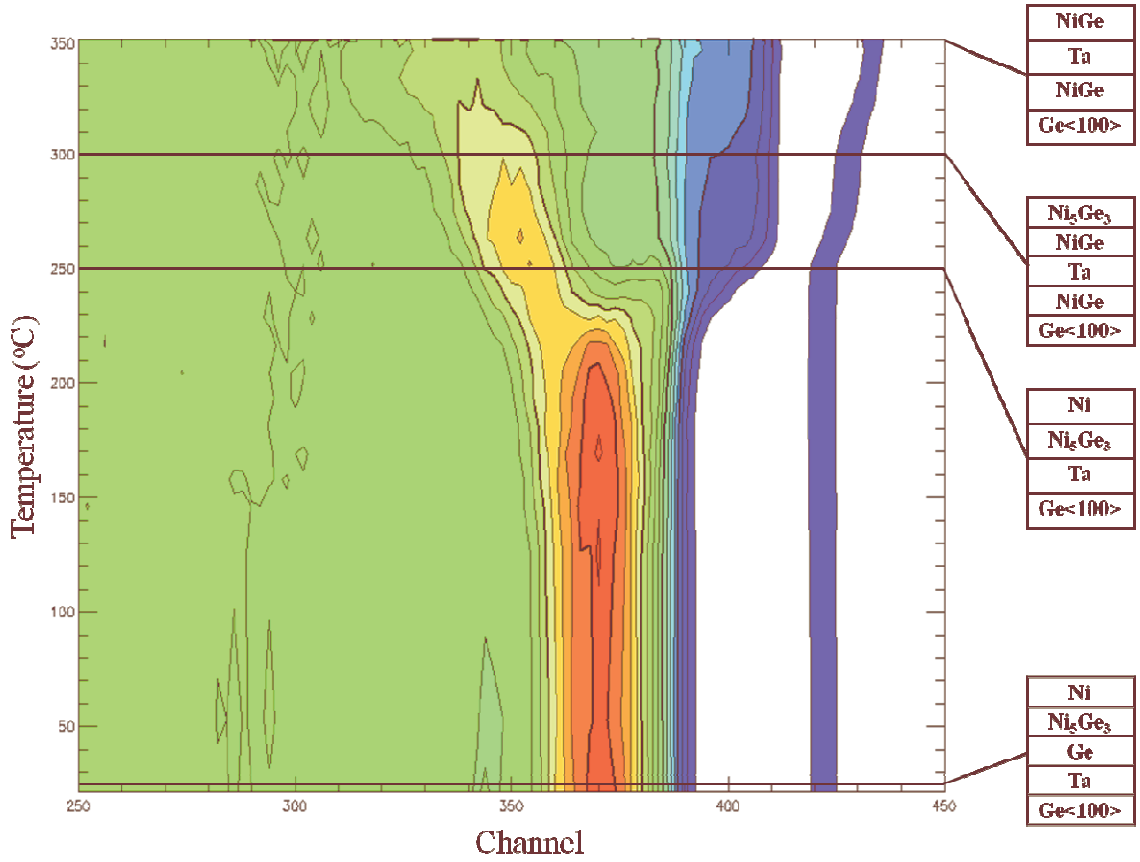

Figure 3.17: Contour map illustrating the sample composition at different stages of the reaction and the thermocouple temperature readings at which they were observed.

The consumption of the Ni_5Ge_3 phase was completed around 328 ^oC. The compositions of the sample at four selected stages of the reaction starting from the as-deposited sample to the end spectrum are illustrated in the contour map shown in Fig. 3.17.

The first stage shows the composition of the sample at the beginning of the reaction (as-deposited). The presence of Ni_5Ge_3 at room temperature has already been confirmed by the RUMP simulation given in Fig. 3.16 (a). The second stage depicts the composition of the sample at 250 ^oC. It can be seen that at this temperature the formation of NiGe had not yet started. This situation is presented in Fig. 3.18 which shows a spectrum measured around this temperature with its corresponding RUMP simulation.

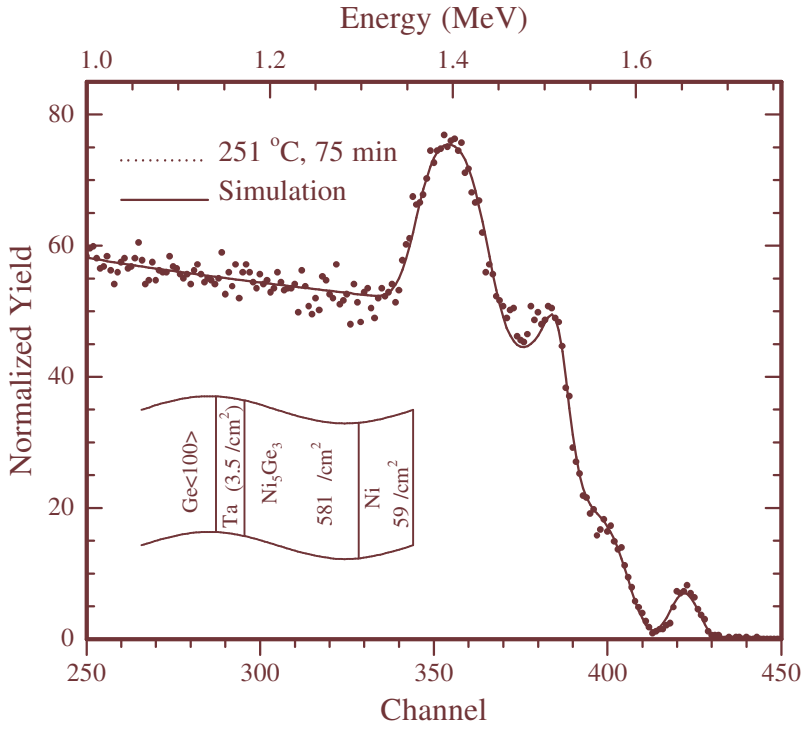

Figure 3.18: Measured spectrum (dotted line) with its RUMP simulation (solid line) taken around 250 ^oC. It illustrates the sample before the transformation of Ni_5Ge_3 to NiGe. The thicknesses are in units of 10^{15} atoms/cm^2.

The third stage illustrates the composition of the sample when the reaction had progressed to about 300 ^oC. At this stage of the reaction the Ni_5Ge_3 phase above the Ta marker is decomposing into the NiGe phase. The Ni freed from the decomposition of Ni_5Ge_3 diffuses to the substrate

where it forms another layer of the NiGe Phase. A measured spectrum captured at this stage of the reaction is displayed in Fig. 3.19 with the corresponding RUMP simulation (solid line) for comparison. The fourth stage marked on the contour plot gives the phases present in the sample at the end of the reaction at 350 ^{o}C as measured by the thermocouple. At this of the reaction, all the Ni_5Ge_3 above the Ta has completely decomposed leaving NiGe as the only compound in the sample both below and above the Ta marker. A measured spectrum taken at this stage of the reaction has already been displayed in Fig. 3.16 (b) with the corresponding RUMP simulation (solid line) for comparison.

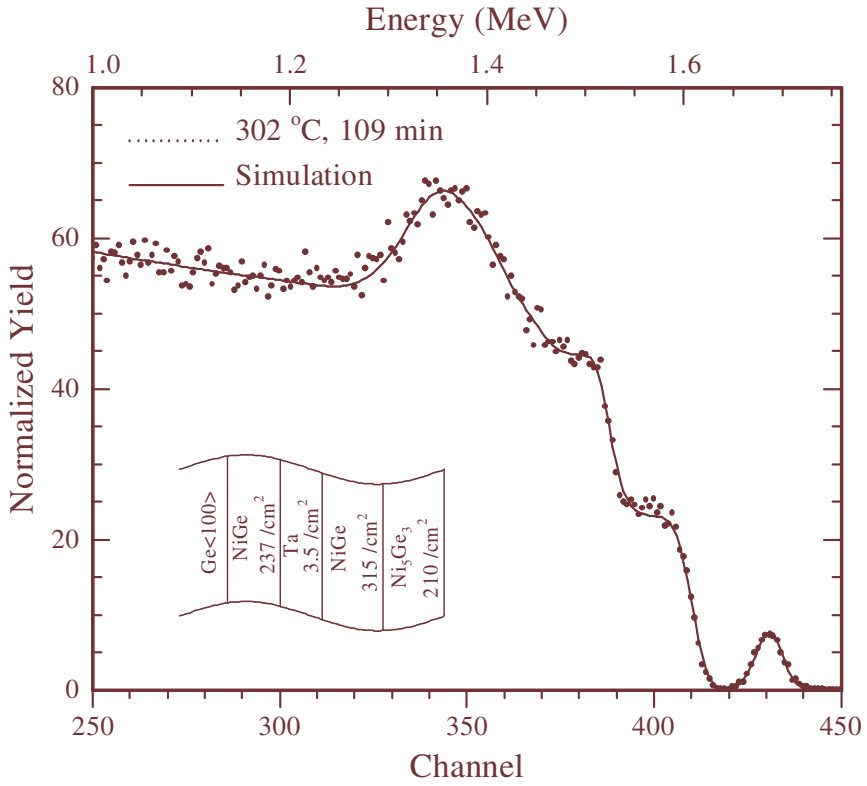

Figure 3.19: Measured spectrum (dotted line) captured around 300 ^{o}C with its RUMP simulation (solid line) showing the phases present in the sample during the transformation of Ni_5Ge_3 to NiGe. The thicknesses are in units of 10^{15} atoms/cm^2.

The spectra for the complete reaction of Ni with Ge for the second sample are summarized in a single 3-dimensional plot by adding time as the third dimension. This 3-D plot is presented in Fig. 3.20. The atomic species contributing to the formation of the various features indicated on the 3-D plot given in Fig. 3.20 were identified using the splot command of the RUMP code. Thus, the feature indicated as NiGe + NiGe + Ni_5Ge_3 means that this feature results from the

overlap of the Ni atoms in NiGe, the Ge atoms in NiGe and the Ge atoms in Ni_5Ge_3. The point where the peak formed by the overlapping of the Ni signal and Ge signal starts to split has also been indicated. The splitting of the peaks occurs in exactly the same manner as that explained in section 3.2.2.

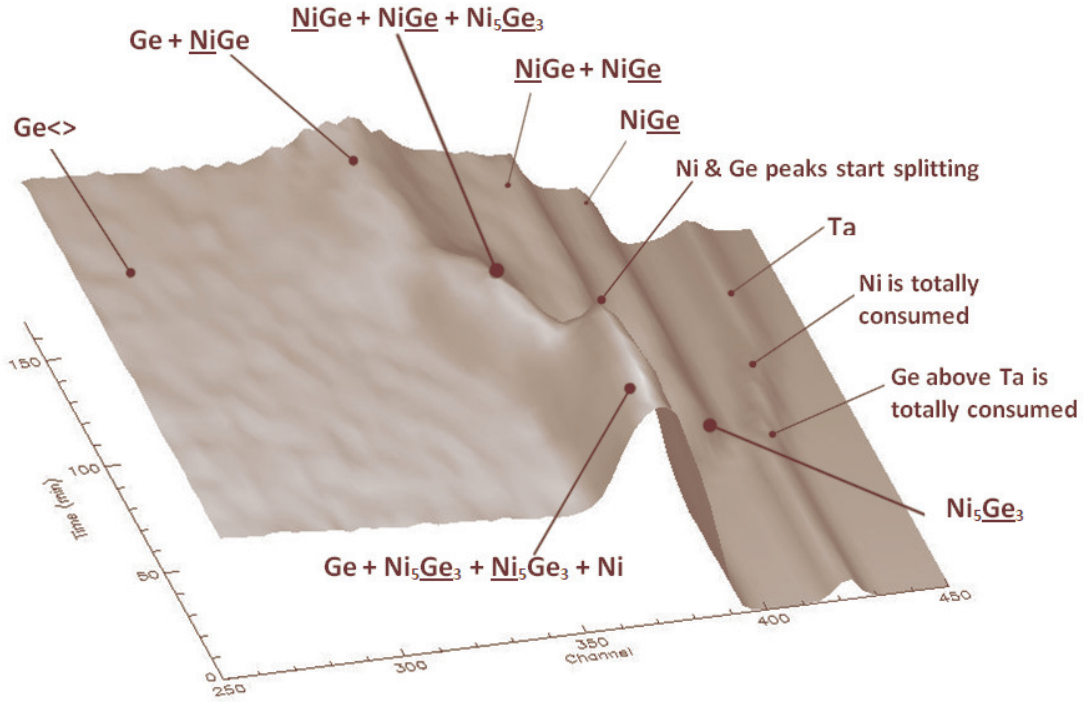

Figure 3.20: In situ, real-time RBS spectra of the formation of Ni_5Ge_3 and NiGe during ramped thermal annealing. The Ta marker initially embedded between the Ge substrate and an adjoining Ge layer shifts to higher energies during the formation of both germanides.

Although the growth of the Ni_5Ge_3 phase was found to have started at room temperature, the 3-D plot in Fig. 3.20 does not show any movement of the Ta marker. However, when Ge deposited above the marker was completely consumed the Ta started moving from its initial position at channel 422 (or 1.69 MeV) towards higher channels (i.e., towards higher energies or towards the surface of the sample). At this stage the excess Ni atoms start diffusing to the substrate. The spectrum in Fig. 3.21 was taken around the stage of the reaction when the Ni_5Ge_3 phase started decomposing to form another layer of NiGe above the Ta marker. This stage of the reaction gives good estimate of the point at which all the Ni was completely consumed. The marker signal in this spectrum was located at channel 426.2 (or 1.669 MeV). This corresponds to the

position marked as 'Ni is totally consumed' on the 3-D plot. It is evident from the 3-D plot in Fig. 3.20 that the Ta marker did not stop moving even after all the Ni above the marker had been completely consumed. This movement of the Ta marker can be seen to be towards the surface of the sample. The Ta marker finally stops moving at channel 433 (or 1.73 MeV).

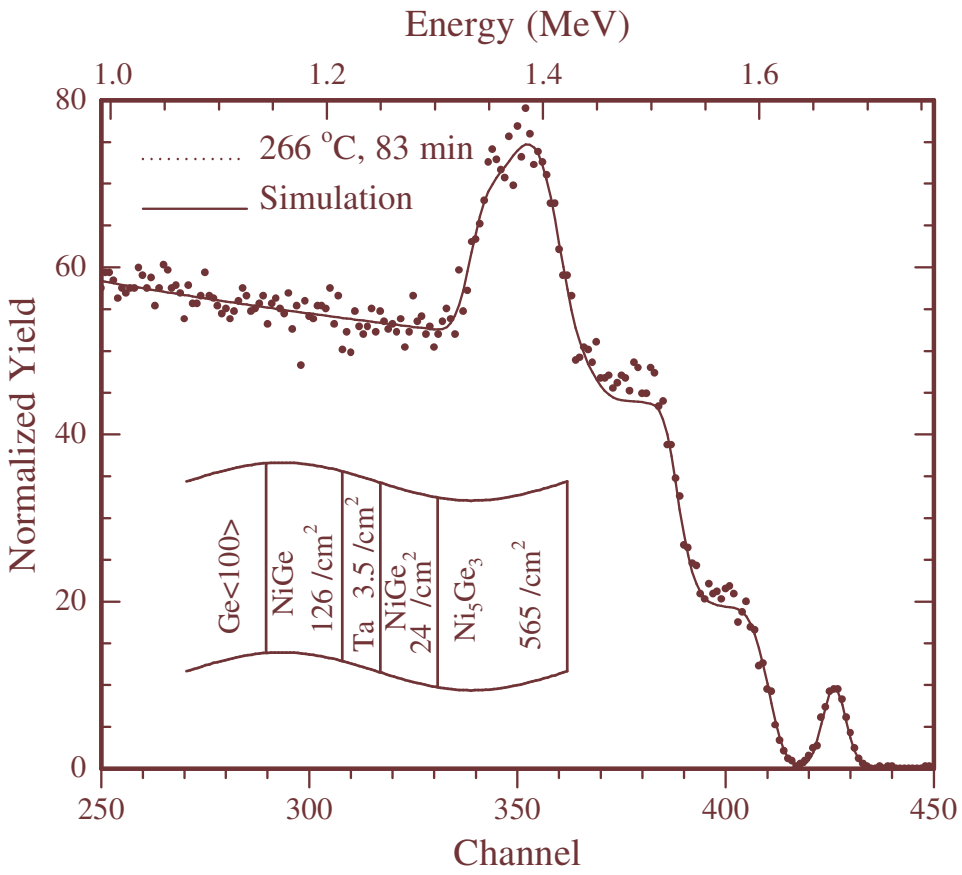

Figure 3.21: Measured spectrum (dotted line) captured around 266 °C with its RUMP simulation (solid line) showing the sample when the Ni_5Ge_3 started transforming to NiGe above the Ta. The thicknesses are in units of 10^{15} atoms/cm^2.

3.3.3 Discussion

The in situ real-time RBS data acquired from the second sample revealed the solid state reaction between α-Ge with the Ni to have started at room temperature to form Ni_5Ge_3. The formation of a phase during deposition at room temperature might be surprising. The other phase that has been reported to form at room temperature is NiGe. Nemouchi et al. [72] reported the formation of this phase during deposition at room temperature. Smith et al. [14] also reported the room

temperature formation of NiGe. Therefore, as far as room temperature formation of a phase is concerned, the room temperature to formation of Ni_5Ge_3 reported in this study is in agreement with the results of the two previously cited workers. This low temperature formation of a nickel germanide is also in agreement with the results of Gaudet et al. [79] also reported the formation of phases to take place at lower temperatures on the amorphous substrate. Gaudet et al. [79] argued that this reduced reaction temperature on α-Ge is expected on the basis of thermodynamics since the enthalpy of formation (ΔH) of the different phases will be larger for α-Ge.

The results obtained from our second sample are similar to those obtained from the first sample as both samples indicate the growth of only the Ni_5Ge_3 and the NiGe phases for the Ni-Ge system in the thin film diffusion couple. The growth of these two phases is however observed to be sequential in the second sample while a brief period of simultaneous growth was observed in the first sample.

The second and final phase obtained from both samples has been identified to be NiGe. The formation of NiGe in the sample without Ge on top of the Ta (first sample) was observed to start at 170 ^{o}C. The in situ real-time RBS data acquired from the second sample as shown in Figs. 3.14 and 3.15 indicate the temperature of formation of NiGe below the Ta marker to be around 239 ^{o}C. In both samples the temperature was held constant at 333 ^{o}C for a further 40 min but no formation of new phases was observed. This indicates that NiGe is the last germanium rich phase that forms during the solid state reaction of Ni with Ge. This agrees with the Ni-Ge binary equilibrium phase diagram where NiGe is predicted as the last and most Ge-rich phase to form in the Ni-Ge system (see Fig. 1.7). The formation of NiGe at 239 ^{o}C as observed in our second sample is almost in agreement with the results of Hsieh et al. [13] who report the formation of NiGe at 250 ^{o}C. The formation of NiGe has also been reported in the temperature ranges of 260-600 ^{o}C, 250-600 ^{o}C and 200-300 ^{o}C by Marshal et al. [67], Wittmer et al. [80] and Patterson et al. [81] respectively. Although there is disagreement on the phase that forms first in the Ni-Ge system, there is general agreement on the second and final phase (NiGe) and its temperature range of formation. Therefore, the identification of the formation of NiGe as the second and final phase in the temperature range of 239-333 ^{o}C in the present study is in good agreement with much of the published literature. There is however a pronounced difference between the results

of Nemouchi et al. [72] and those obtained in this study in that the former workers report the formation of NiGe during deposition at room temperature.

Following the marker results of the sample with configuration Ge<100>/Ta(5 Å)/Ni(800 Å), the reaction in the sample with configuration Ge<100>/Ta(6 Å)/Ge(490 Å)/Ni(470 Å) was expected to proceed through the metal-rich germanide Ni_5Ge_3 to the monogermanide NiGe. The reaction path was expected to begin with the consumption of Ni and Ge above the Ta marker to form Ni_5Ge_3 followed by the diffusion of unreacted Ni towards the substrate. The reaction was then expected to continue with the consumption of the diffusing Ni atoms with Ge atoms in the substrate to form another layer of Ni_5Ge_3 below the Ta marker. After total consumption of the unreacted Ni the reaction should then have proceeded via the dissociation of Ni_5Ge_3 below the marker. There are two possible mechanisms by which the consumption or dissociation of the Ni_5Ge_3 could have proceeded. Firstly, it could have reacted with the Ge from the substrate through the mechanism $Ni_5Ge_3 + 2Ge \rightarrow 5NiGe$ to form NiGe. Secondly, the mechanism $Ni_5Ge_3 \rightarrow 3NiGe + 2Ni$ could have taken place to form NiGe.

The reaction would then have been expected to be completed by the formation of NiGe above the marker via one or both of the mechanisms described above. The growth of nickel germanides according to the reaction path explained above is illustrated schematically in Fig. 3.22.

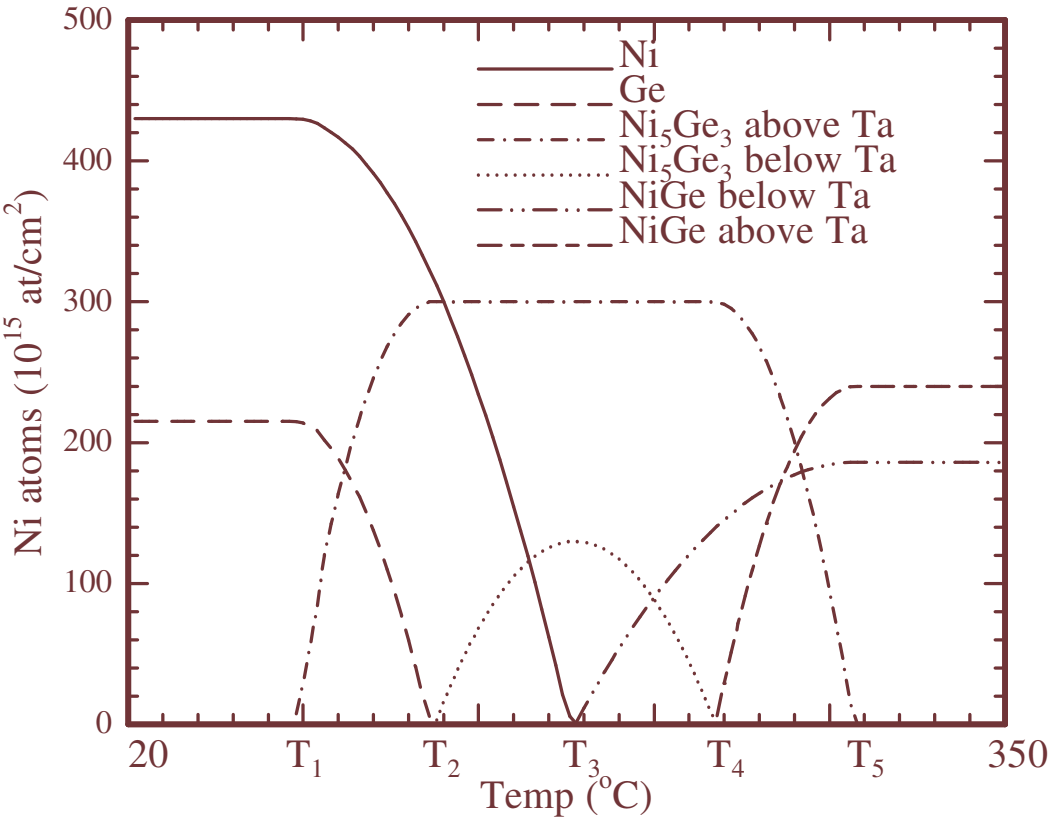

Figure 3.22: Expected reaction path for nickel germanide phase formation during ramped thermal anneal from 23 °C to 333 °C for the sample with configuration Ge<100>/Ta(6 Å)/Ge(490 Å)/Ni(470 Å).

There is agreement between the expected and the actual sequence of germanide phase formation in this second sample expect for the absence of the Ni_5Ge_3 phase below the marker. According to the reaction path illustrated in Fig. 3.22, Ni_5Ge_3 should have formed both below and above the Ta marker before the formation of NiGe below and above the marker. The growth of Ni_5Ge_3 below the marker was however not observed as was expected. The existence of the Ni_5Ge_3 could have been so short lived that it could not have been clearly observed. This short lived existence of the Ni_5Ge_3 phase could have been observed in the temperature interval between 240-250 °C in Fig. 3.14 and Fig. 3.15 where no growth seemed to be taking place. A possible explanation for this could be the limited supply of the excess Ni above the marker to the substrate.

The unreacted Ni above the marker and the Ni freed by the thermal dissociation of Ni_5Ge_3 above the marker that diffused to the substrate reacted with Ge in the substrate to form NiGe below the marker. The formation of NiGe above the marker was in large part due to the thermal

dissociation of Ni_5Ge_3 and to a lesser extent due to the reaction of Ni_5Ge_3 with Ge from the substrate.

The simulation of the end spectrum for the first sample shown in Fig. 3.7 (d) indicates a thickness of 1500×10^{15} atoms/cm^2 of NiGe. This thickness of the monogermanide contains 750×10^{15} atoms/cm^2 atoms of Ni. The simulation of the as-deposited spectrum shown in Fig. 3.7 (a) indicates a presence of 747×10^{15} atoms/cm^2 atoms of Ni; that is 722×10^{15} atoms/cm^2 in unreacted Ni and 25×10^{15} atoms/cm^2 in the 41×10^{15} atoms/cm^2 Ni_5Ge_3 layer. The difference between the Ni observed to be present from the as-deposited spectrum (747×10^{15} atoms/cm^2) and that in the end spectrum (750×10^{15} atoms/cm^2) is insignificant as is expected since we use the same sample throughout the reaction.

In the second sample, the amount of Ge found in the NiGe above the marker was in excess of that initially deposited above the Ta marker. The conclusion from this result is that the reaction above the marker could not have solely proceeded by the mechanism $Ni_5Ge_3 \rightarrow 3NiGe + 2Ni$ but partly through the mechanism $Ni_5Ge_3 + 2Ge \rightarrow 5NiGe$ because this is the only way that there would be more Ge atoms than was initially deposited above the Ta marker. The Ge atoms would have had to come from the substrate across the marker. However, the continued growth of NiGe below the marker shows that the dominant reaction mechanism above the Ta marker was $Ni_5Ge_3 \rightarrow 3NiGe + 2Ni$ rather than the mechanism $Ni_5Ge_3 + 2Ge \rightarrow 5NiGe$.

The Ta marker was observed to be stationary even after the growth of Ni_5Ge_3 had started. This shows that during the formation of the Ni_5Ge_3 the reaction was taking place entirely above the Ta marker. The Ta marker started moving when all the Ge above it was completely consumed in the formation of Ni_5Ge_3 because the excess Ni above the marker started diffusing to the substrate. However, the marker continues to move towards the surface even after the unreacted Ni is totally consumed. This indicates that the reaction $Ni_5Ge_3 \rightarrow 3NiGe + 2Ni$ rather than the reaction $Ni_5Ge_3 + 2Ge \rightarrow 5NiGe$ is the dominant mechanism which acts as another source of Ni. The Ni atoms freed through the reaction $Ni_5Ge_3 \rightarrow 3NiGe + 2Ni$ diffuse to the substrate thereby pushing the Ta atoms further outwards until the thermal dissociation of Ni_5Ge_3 is complete.

It was also observed that the NiGe below the Ta marker does not stop growing even when the unreacted Ni is totally consumed. There must then be a continued supply of Ni atoms to the substrate from above the marker which react with the Ge atoms in the substrate for the thickness

of the NiGe layer below the marker to continue increasing. This supply of Ni from above the marker comes from the dissociation or consumption of Ni_5Ge_3 which results from the $Ni_5Ge_3 \rightarrow 3NiGe + 2Ni$ decomposition mechanisms.

3.4 Dominant Diffusing Species (DDS)

3.4.1 Dominant Diffusing Species During Ni_5Ge_3 Formation

To study the dominant diffusing species during Ni_5Ge_3 growth, we first consider the sample with configuration Ge<100>/Ta(5 Å)/Ni(800 Å). It has been shown in section 3.2.2 that for this sample all the Ta moved to the surface of the sample at the end of the reaction (see Fig. 3.7 (d)). The evolution of the phases from the as-deposited sample to the end of the reaction can thus be schematically depicted as shown in Fig. 3.23.

Fig. 3.23 illustrates the interlayer inversion that occurred between the Ni and the Ta from the initial stage to the final stage of the reaction. The relative shift of the Ta marker signal from its initial position in the as-deposited spectrum to its final position in the end spectrum after completion of the reaction is illustrated in Fig. 3.24 by superposition of the virgin and end spectra. The Ta marker signal was at channel 403 (or 1.64 MeV in terms of energy) in the as-deposited sample.

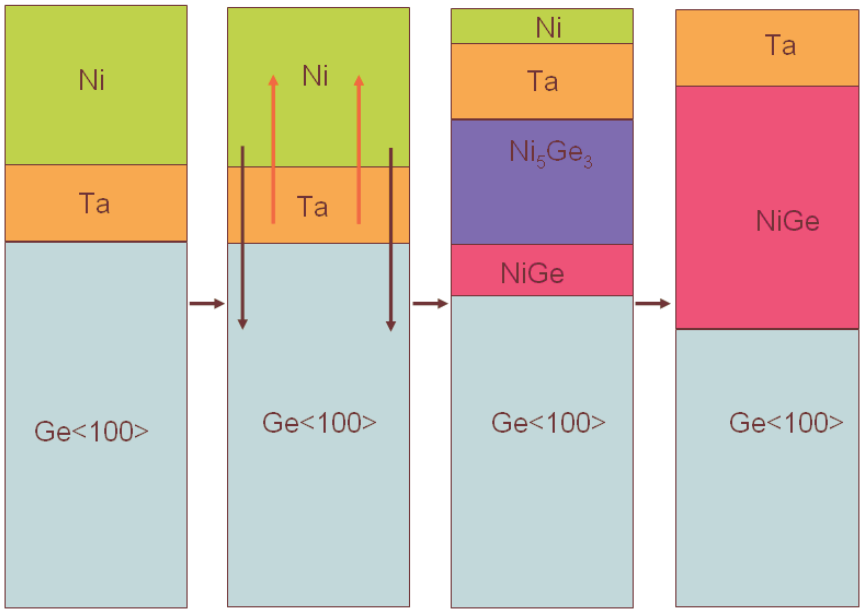

Figure 3.23: As-deposited structure and subsequent phase formation after annealing the sample with configuration Ge<100>/Ta(5 Å)/Ni(800 Å).

The final position of the Ta marker signal in the end spectrum was at channel 453.46 (or 1.83 MeV in terms of energy). The Ta marker signal thus shifted by 50.5 channels (or by 0.19 MeV in terms of energy) towards higher channels or higher energies, i.e., towards the surface. The arrow labeled K_{Ta} in Fig. 3.24 indicates the surface position of alpha particles scattered from the Ta if it was at the surface of the sample. The final position of the Ta signal coincides with its surface position at the end of the reaction. This observation further corroborates the one made in section 3.2.2 where the Ta marker was found to have reached the surface of the sample.

By noting the Ta marker position for the thickness of Ni_5Ge_3 formed, the reaction mechanism may be evaluated quantitatively.

The motion of the Ta marker as a function of Ni_5Ge_3 thickness formed together with the limiting cases of pure Ni and pure Ge diffusion is illustrated in Fig. 3.25. In order to obtain the lines for pure Ni and pure Ge diffusion, it should be noted that the point of intersection of the lines for these two limiting cases on the marker position axis was fixed by the initial position of the marker in the as-deposited spectrum.

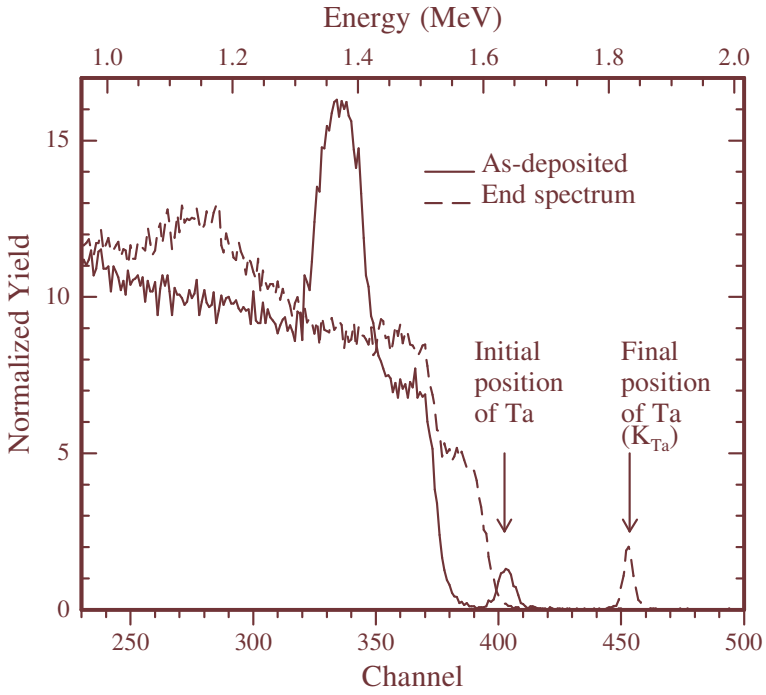

Figure 3.24: Superposition of RBS spectra of the as-deposited sample and the end spectrum after ramped thermal annealing to illustrate the relative shift of the Ta marker signal. The label K_{Ta} in brackets indicates the position of alpha particles scattered from Ta atoms located at the surface of the sample.

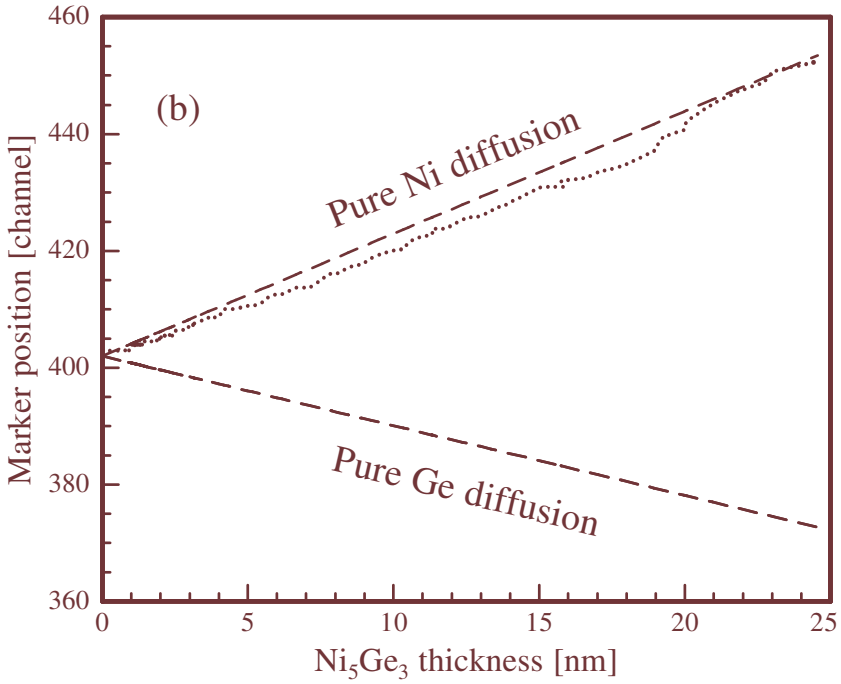

Fig. 3.25: The observed motion of the Ta marker as a function of the Ni_5Ge_3 thickness formed (dotted line), suggesting that Ni is the only diffusion species during the formation of Ni_5Ge_3. The

deviation of the observed marker motion from the limiting case of Ni diffusion can be attributed to the broadening of the marker after the start and before the end of the reaction. The two limiting cases of Ni or Ge diffusion are indicated as broken lines.

The lines for pure Ni and pure Ge diffusion were obtained using RUMP simulations of the two limiting situations. The motion of the marker plotted in Fig. 3.25 is observed to deviate from the limiting case of Ni diffusion after the start and before the end of the reaction.

3.4.2 Dominant Diffusing Species During NiGe Formation

The key features of the reaction stages observed for the second sample structure are schematically illustrated in Fig. 3.26. The schematic diagram given in Fig. 3.26 is corroborated by the marker movement as can be seen from the contour map in Fig. 3.17 and the 3-D plot in Fig. 3.20. The movement of the Ta marker towards the surface of the sample as seen in Fig. 3.17 and Fig. 3.20 is an indication of the Ni diffusing to the substrate producing a layer of NiGe below the marker. However, it is not possible to establish from this outward movement of the marker alone whether the Ge was also diffusing or not.

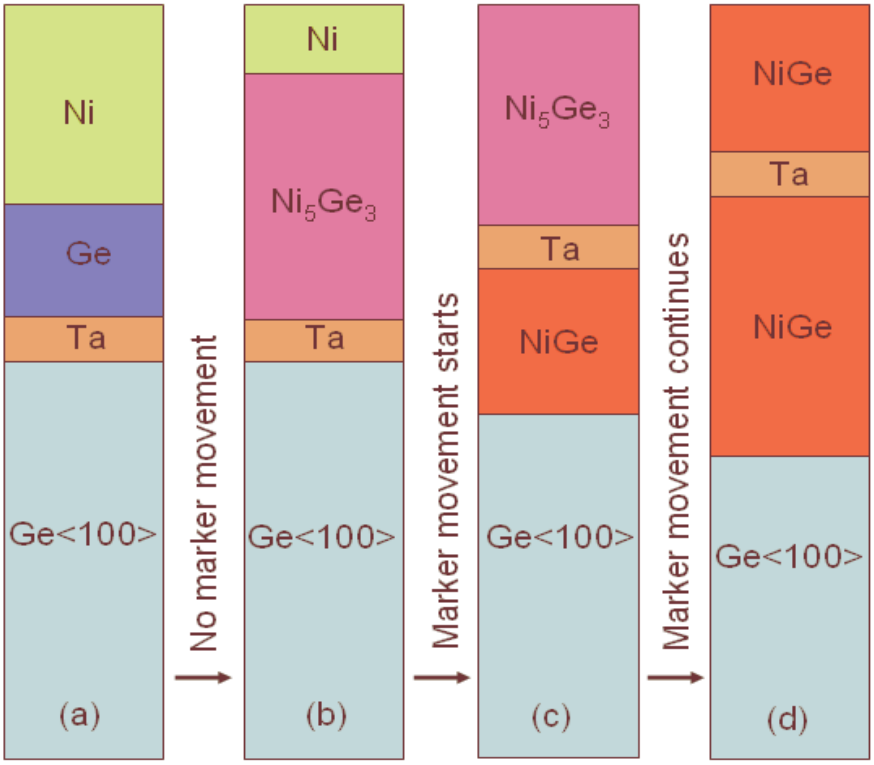

Figure 3.26: Schematic representation of the major stages of the reaction for the Ge<100>/Ta(6 Å)/Ge(490 Å)/Ni(470 Å) sample configuration used to determine the dominant diffusing species during NiGe formation. (a) As-deposited sample assuming no reaction between the Ni and Ge, (b) all the Ge above Ta is totally consumed, (c) all the Ni is completely consumed and (d) the decomposition of Ni_5Ge_3 is completed.

There is no movement of the Ta marker during the formation of Ni_5Ge_3. When the Ge above the marker has been completely consumed in the formation of Ni_5Ge_3 we would either expect the excess Ni to diffuse across the marker and react with the Ge in the substrate or the Ge in the substrate could diffuse across the marker to react with the excess Ni. After all the Ni has been completely consumed the Ni_5Ge_3 phase starts to dissociate forming another layer of NiGe above the Ta marker.

The formation of NiGe above the marker can occur as a result of thermal dissociation of Ni_5Ge_3 through the mechanism $Ni_5Ge_3 \rightarrow 3NiGe + 2Ni$ or reaction of Ni_5Ge_3 with the germanium atoms from the substrate through the mechanism $Ni_5Ge_3 + 2Ge \rightarrow 5NiGe$ or both. The possibility of Ge diffusion during NiGe formation can be established in two different ways. Firstly, if there was no Ge diffusion during the formation of NiGe the amount of Ge in the final germanide above the marker should not exceed the amount of Ge initially deposited above the marker. The RUMP simulation of the end spectrum in Fig. 3.16 (b) indicates the presence of 480×10^{15} atoms/cm^2 of NiGe above the marker. This means that there is 240×10^{15} atoms/cm^2 of Ge atoms. The RUMP simulation of the sample at room temperature presented in Fig. 3.16 (a) shows that there was initially 215×10^{15} atoms/cm^2 of Ge above the Ta marker. Therefore, there is an excess of about 25×10^{15} atoms/cm^2 of Ge above the marker. These excess Ge atoms above the marker could only have come from the diffusion of Ge from the substrate. Thus the amount of Ge that diffused across the marker is about 12% of the original amount of Ge above the marker. This amount of Ge diffused from the substrate and reacted with the Ni released from the dissociation of Ni_5Ge_3 above the marker.

We now consider the second way by which we can establish the possibility of Ge diffusion during NiGe formation. After the Ni deposited above the marker is completely consumed, the Ni_5Ge_3 above the marker could be transformed to NiGe either by thermal dissociation through the mechanism $Ni_5Ge_3 \rightarrow 3NiGe + 2Ni$ or by reacting with Ge from the substrate through the mechanism $Ni_5Ge_3 + 2Ge \rightarrow 5NiGe$. If we assume that the transformation occurs entirely by the first mechanism then the NiGe below the marker would grow as a result of the freed Ni diffusing

across the marker and reacting with the Ge from the substrate. According to the reaction equation $Ni_5Ge_3 \rightarrow 3NiGe + 2Ni$ the NiGe produced below the marker as a result of the freed Ni diffusing across the marker would be in a ratio of 2:3 with the NiGe produced above the marker. The NiGe produced above the marker in this manner will therefore be 3/5 of the total NiGe produced as a result of the dissociation of Ni_5Ge_3. In that case a plot of the total NiGe growth against the NiGe growth above the marker should yield a straight line with a slope of 5/3 or about 1.67. The intercept of this graph gives the amount of NiGe formed below the marker before dissociation of Ni_5Ge_3 above the marker. At this intercept there would be no NiGe above the marker. The graph of the total NiGe growth as a function of the NiGe growth above the Ta marker is presented in Fig. 3.27. The slope of the graph in Fig. 3.27 is 1.46. It has been noted that if all the Ni freed from the dissociation mechanism had diffused to the substrate the slope of the graph in Fig. 3.27 would have been 1.67. The difference between 1.67 and 1.46 is 0.21. This reflects the amount of the freed Ni that did not diffuse to the substrate. The Ni atoms which did not diffuse to the substrate reacted above the marker with the Ge atoms diffusing across the marker from the substrate. The percentage of the freed Ni that reacted above the marker as a result of Ge diffusing across the marker from the substrate can then be found to be 12.5%. Therefore, about 12.5% of the Ni freed from the dissociation of Ni_5Ge_3 above the marker reacted with Ge from the substrate that must have diffused across the marker.

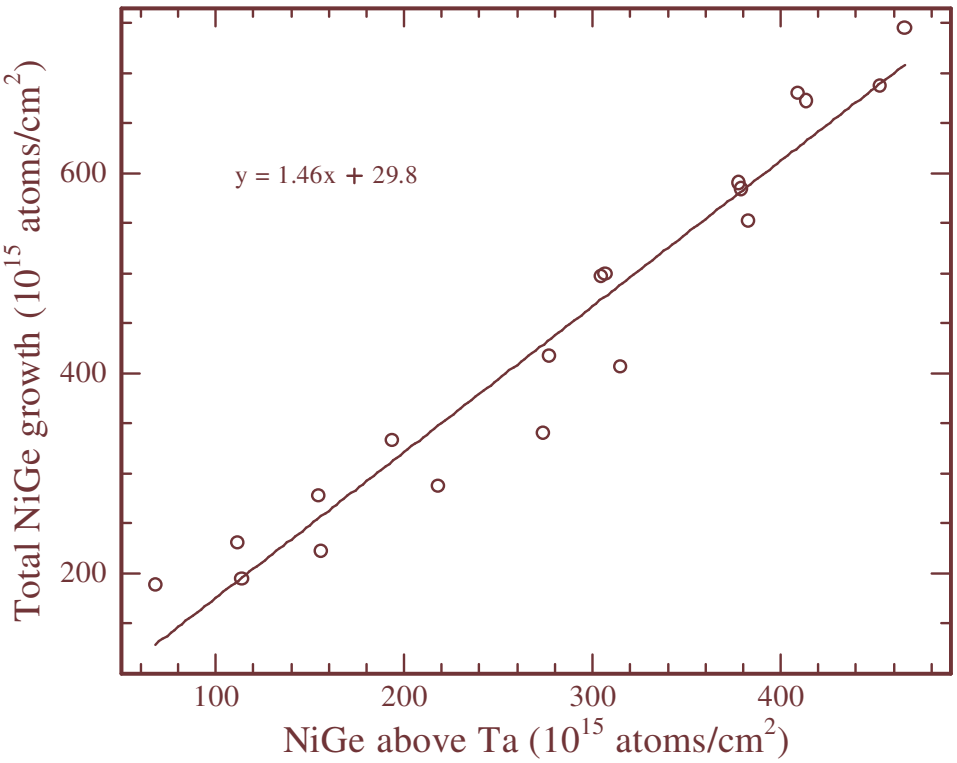

Figure 3.27: A graph of the total NiGe growth as a function of the NiGe growth above the Ta marker.

Since the final phase above the marker is NiGe the reaction of 12.5% of Ni atoms would require an equal number of Ge atoms. Thus the amount of Ge that diffused across the marker is also about 12.5% of the original amount of Ge above the marker. This correlates well with the earlier calculation where we found the amount of Ge that diffused across the marker to be about 12% of the original amount of Ge above the marker.

3.4.3 Discussion

It has been established in section 3.2.2 that in the first sample, all the Ta moved to the surface of the sample at the end of the reaction. This can also be seen from Fig. 3.24 where the final position of the Ta signal is observed to coincide with the surface position of Ta. The appearance of the Ta at its surface position is clear indication that all the Ta atoms had reached the surface of the sample at the end of the reaction. The only definite conclusion that can be drawn from this observation is that Ni is the sole diffusing species during the formation of Ni_5Ge_3. This is so because if there had been diffusion of Ge during the formation of Ni_5Ge_3 then there would have

been another germanide layer above the Ta marker. In that case the Ta marker would have been trapped between the two germanide layers and it would not have reached the surface. The motion of the Ta marker as a function of Ni_5Ge_3 thickness formed illustrated in Fig. 3.25 further confirms the observation that Ni is the sole moving species during the Ni_5Ge_3 phase formation. The deviation of the observed marker motion from the limiting case of Ni diffusion can be attributed to the broadening of the marker after the start and before the end of the reaction.
Since all the Ta atoms reached the surface at the end of the reaction it can be concluded that no germanium diffusion occurred during the formation of Ni_5Ge_3. After total consumption of Ni and with all the Ta atoms having moved to the surface of the sample the subsequent reaction took place entirely below the Ta which rendered it useless as an inert marker to monitor the direction of atomic mobility. Thus by using the results of the first sample configuration no definite conclusion could be made about the diffusing species during the formation of NiGe.

The results obtained from the second sample established that both nickel and germanium were diffusing during the formation of the last and final phase, NiGe. The movement of the Ta marker towards the surface observed in Fig. 3.17 and Fig. 3.20 clearly indicate that Ni was the dominant diffusing species during NiGe formation. These results do not however tell us whether Ni was the sole moving species during NiGe formation, i.e., it is not yet conclusive from these results that there was no diffusion of Ge during NiGe formation. Two separate analyses were employed to determine the moving species during NiGe formation.

The first analysis was based on the argument that if there was no diffusion of Ge during the formation of the NiGe then the amount of Ge in the final germanide above the Ta marker would not exceed the amount of Ge initially deposited above the marker. An atomic calculation of Ge in the NiGe above the marker in the end spectrum indicated an increase in Ge above the marker of about 12%. The other source of Ge apart from the Ge deposited on top of the Ta is the substrate. Therefore, the extra Ge atoms diffused from the substrate and reacted with Ni above the Ta marker. This is a firm confirmation that Ge was also diffusing during the formation of NiGe.

The second analysis was based on the observation that since the Ta marker signal moved towards the surface throughout the reaction period, the dominant reaction mechanism during the thermal dissociation of Ni_5Ge_3 should be $Ni_5Ge_3 \rightarrow 3NiGe + 2Ni$ and not $Ni_5Ge_3 + 2Ge \rightarrow 5NiGe$.

Therefore, if the total NiGe growth is plotted as a function of the NiGe growth above the marker a straight line should be obtained with a slope of 5/3 or 1.67. The intercept of this graph would give the amount of NiGe grown below the marker from the diffusion of the excess Ni above the marker after all Ge above the marker is totally consumed; this is before the consumption of Ni_5Ge_3 above the marker begins. If there was 100% diffusion of the Ni freed from the decomposition mechanism the slope of the graph in Fig. 3.26 would be 1.67. The slope of this graph was however found to be 1.46 which indicates that about 12.5% of the Ni released from the decomposition mechanism did not diffuse to the substrate. The only reason this amount of Ni did not diffuse to the substrate is that it reacted right above the Ta marker. Since the final phase above the marker is NiGe, the reaction of 12.5% of Ni atoms would require an equal number of Ge atoms. Thus an equal amount of Ge must have diffused from the substrate to react with Ni above the marker. This is in reasonable agreement with the result obtained using the first approach.

The results from both the atomic calculations and the graphical analysis firmly indicate that both Ni and Ge diffuse during the formation of NiGe. From the atomic and graphical calculations, the ratio of the number of Ni atoms that diffused to the substrate to the number of Ge atoms that diffused from the substrate is about 88:12. This indicates that although both Ni and Ge were mobile during the formation of NiGe, Ni was still the dominant moving species.

Since the literature surveyed did not provide any information on the DDS during the formation of both Ni_5Ge_3 and NiGe, no comparisons can be made with our results. However the tendency of both metal and Ge to diffuse, which we observed during the formation of NiGe, has also been reported by Marshal et al. [67] during the formation of Ni_2Ge.

3.5 Growth Kinetics

The same data obtained from the samples used in the identification of the phase formation sequence and determinations of the dominant diffusing species were used for growth kinetics analysis. This illustrated one of the advantages of using the in situ real-time RBS technique as different types of analyses were performed on data generated from the same samples. This eliminated the problem of sample to sample variation commonly encountered in conventional

annealing methods. Another advantage was that RBS spectra were obtained at all stages of compound growth.

3.5.1 Growth Kinetics Results

The collected RBS spectra were analyzed using the RUMP program to obtain estimates of the thicknesses of compounds formed during the solid state reactions. It will be explained later in this section that the atomic densities of Ni_5Ge_3 and NiGe must be known in order to carry out a complete analysis of the growth kinetics for Ni_5Ge_3 and NiGe. It was not possible to make a good estimate of the atomic density for NiGe and therefore the analysis of the growth kinetics was only done for the Ni_5Ge_3 phase. This analysis was done for the sample with configuration Ge<100>/Ta(5 Å)/Ni(800 Å) in which simultaneous growths of Ni_5Ge_3 and NiGe were observed. Presented below are results of the growth kinetics of Ni_5Ge_3 obtained from in situ annealing in the 1 ^oC/min ramp rate region of the temperature profile presented in Fig. 3.2.

Prior to activation energy analysis it is necessary to determine whether compound growth is diffusion or reaction limited from RBS data of isothermally annealed samples. No samples were prepared for isothermal annealing in this study. The reasons for calculating the activation energy of diffusion for Ni_5Ge_3 without first explicitly showing that the growth of this phase is diffusion controlled are twofold: Firstly, it is usually reported that silicides and germanides follow a diffusion controlled growth [48, 49]. Secondly, we have shown in section 3.4.1 that the growth of Ni_5Ge_3 is solely as a result of Ni diffusion. Therefore, our determination of the activation energy of diffusion for Ni_5Ge_3 without first explicitly showing that the growth of this phase is diffusion controlled is justified.

Since the RUMP program gives the phase 'thicknesses' in units of atoms/cm^2 (i.e. areal density), the atomic density in units of atoms/cm^3 must be known in order to make conversions of phase thicknesses from atoms/cm^2 to cm. A search for the atomic densities of both Ni_5Ge_3 and NiGe from the literature and the internet did not yield any direct results. Therefore, recourse was taken to the results of Nemouchi et al. [72] who reported the simultaneous growths of Ni_5Ge_3 and NiGe and a critical thickness for Ni_5Ge_3 growth of around 10 nm before the onset of the growth of the NiGe phase. The critical thickness is associated with the phenomenon of simultaneous phase growth in thin films. It is a thickness which one phase must reach before another phase can

start to grow. There was simultaneous growth of Ni_5Ge_3 and NiGe in our first sample as can be seen in Fig. 3.5. The critical thickness of Ni_5Ge_3 in units of atoms/cm^2 could be obtained from the point of the onset of NiGe growth before the complete consumption of the unreacted Ni. As mentioned earlier if the density of a compound in units of atoms/cm^3 is known, then the areal thickness of the compound in units of atoms/cm^2 can be converted to the thickness in units of cm. Conversely, if the thickness of a phase in cm is known then the atomic density of the compound in units of atoms/cm^3 can be obtained from its areal density. Thus, by comparing our observed thickness of Ni_5Ge_3 (in units of atoms/cm^2) at the point when NiGe started to grow and the critical thickness of Ni_5Ge_3 growth reported by Nemouchi et al. [72] (in units of cm) the atomic density of Ni_5Ge_3 was estimated. This was then used to convert the thicknesses of the Ni_5Ge_3 phase throughout the reaction from atoms/cm^2 to cm.

Referring to Eq. 1.9, $\ln(x^2/T^2)$ was plotted against $1/T$ forming a Kissinger plot and an estimate of the activation energy was obtained from the slope. The Kissinger plot from which the activation energy for the solid state diffusional growth of Ni_5Ge_3 was determined is presented in Fig. 3.28.

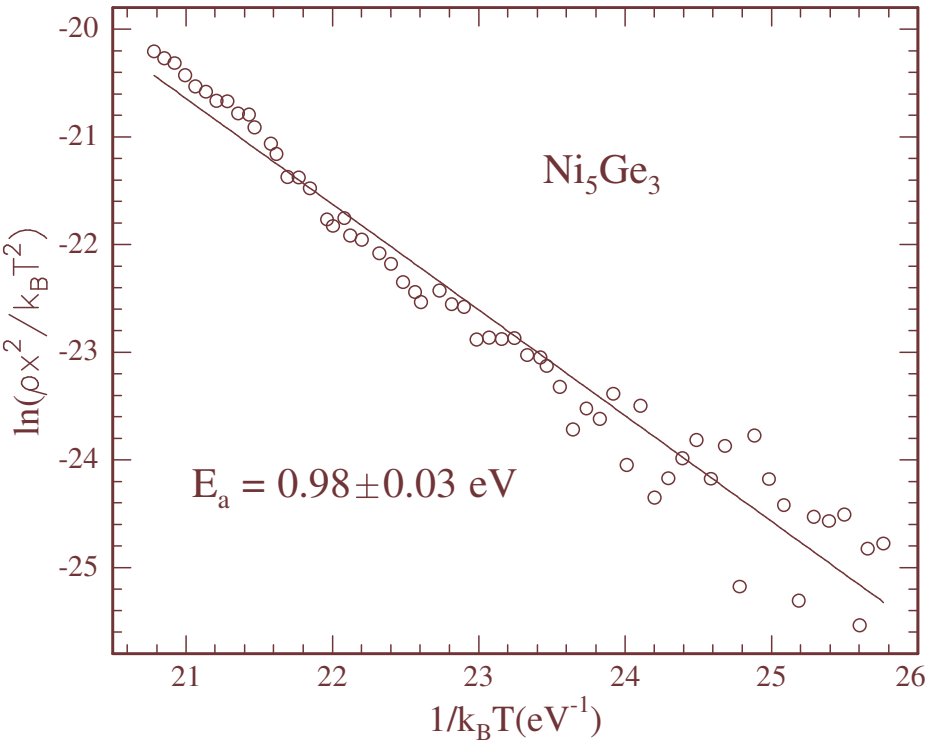

Fig. 3.28: Kissinger plot for Ni_5Ge_3 formation obtained from temperature ramping of the sample with configuration Ge<100>/Ta(5 Å)/Ni(800 Å) in the range 143-301 ^oC of the temperature profile at a ramp rate of $\rho = 1\ ^oC/min$.

The data for the Kissinger plot were taken in the 136-333 ^oC temperature window in which the ramp rate ρ was maintained at 1 $^oC/min$. The estimated activation energy for the solid state diffusional growth of Ni_5Ge_3 was found to be $E_a = 0.98 \pm 0.03$ eV.

3.5.2 Discussion

Using the critical thickness results of Nemouchi et al. [72] we were able to estimate the atomic density of Ni_5Ge_3. From this estimate of the atomic density the various growth thicknesses of the Ni_5Ge_3 phase for the first sample were converted from at/cm^2 to cm. The thicknesses in units of cm were then used in a Kissinger plot to calculate the activation energy of diffusion for Ni_5Ge_3. The activation energy of diffusion for Ni_5Ge_3 was found to be $E_a = 0.98 \pm 0.03$ eV. This is in close agreement with the result of Nemouchi et al. [71] who reported the activation energy of diffusion for the Ni_5Ge_3 phase to be 0.8 eV.

CHAPTER 4

SUMMARY AND CONCLUSION

In this work, the formation characteristics of nickel germanides were investigated in real time using in situ RBS. Nonconventional (i.e., with marker) thin film binary couples were used to study the solid phase interaction of nickel and germanium at subeutectic temperatures. The experiment was set to investigate the thermally induced solid state reaction of nickel with germanium to determine which of the many phases given by the equilibrium binary phase diagram forms first, the sequence in which these phases are formed, the temperature range of

formation of these phases, the dominant diffusing species during the formation of each phase and the activation energy for their formation.

The nonconventional thin film diffusion couples used in this study were prepared with sample configurations of Ge<100>/Ta(5 Å)/Ni(800 Å) as the first sample and Ge<100>/Ta(6 Å)/Ge(490 Å)/Ni(470 Å) as the second sample. The purpose of the thin Ta layer interposed between the germanium substrate and the overlying layers was to act as an inert marker to monitor the direction of atomic mobility during the reaction. Using these two samples the solid state reactions of thin nickel films with germanium were monitored in real-time. The depth and compositional profiling capabilities of in situ, real-time RBS were combined with linearly ramped thermal annealing in the scattering chamber which allowed the formation characteristics to be obtained from a single sample. Our in situ real-time study had the advantages of providing a continuous observation of the phases formed in the film, consumption of less time and material, and provision of a more convenient method in cases where sample preparation and sample reproducibility would be difficult. The in situ, real-time RBS proved to be well suited for the analysis of Ni-Ge thin film solid state reactions because it is a beam-based method which did not necessitate direct mechanical contact and was quite sensitive.

The solid state reactions in both samples described above were thermally induced by ramping the temperature from room temperature to 333 ^{o}C. The RBS spectra used for our analysis were acquired in real-time using in situ ramped thermal annealing with 2 MeV ^{4}He ions taken in a random geometry. The Ni-rich germanide that formed first during the reaction of thin Ni films with Ge was identified to be Ni_5Ge_3. The formation of the Ni_5Ge_3 phase in the first sample was found to have started 145 ^{o}C. In this sample the Ni_5Ge_3 phase grew steadily from this temperature (145 ^{o}C) to 298 ^{o}C after which its decomposition started. In the second sample the formation of the Ni_5Ge_3 phase was detected at room temperature. The layer thickness of the Ni_5Ge_3 phase in this sample was observed to be increasing in what appeared to be a quadratic manner from its nucleation at room temperature up to a temperature of about 239 ^{o}C where there was no growth taking place as can be seen in Fig. 3.14 and Fig. 3.16. The phase started to decompose at a temperature of about 250 ^{o}C. The decomposition of Ni_5Ge_3 was found to be complete around 328 ^{o}C.

The observed formation of Ni_5Ge_3 during deposition at room temperature in the second sample might be surprising but similar results have been reported by Nemouchi et al. [72] who reported the formation of NiGe during deposition at room temperature. The germanidation of nickel at room temperature is also in agreement with the results of Smith et al. [14] who also reported the reaction of Ni with Ge at room temperature. Nemouchi et al. [72] attributed this phenomenon to the large driving force during deposition due to the additional heat of condensation as the Ge substrate is in contact with the Ni vapor rather than a solid phase (which is the case during thermally induced solid state reactions). The identification of Ni_5Ge_3 as the phase that forms first in both samples is therefore consistent with results reported by Gaudet et al. [80], Nemouchi et al. [71, 72] and Patterson et al. [82] who also identified Ni_5Ge_3 as the first Ni-rich germanide for the Ni-Ge system. The observation of reaction at room temperature in the second sample and the identification of Ni_5Ge_3 as the first phase in both samples is however, in contrast with the results by Marshal et al. [67], Hsieh et al. [13] and Wittmer et al. [81] who reported the formation of Ni_2Ge as the first phase to form for the Ni-Ge system. It is also in contrast with the results of Jin et al. [64] who reported the formation of Ni_3Ge_2 as the first phase. These workers all reported the reaction to occur at temperatures of 150 ^oC and above. Our identification of Ni_5Ge_3 as the first Ni-rich phase in the Ni-Ge system also violates the Walser and Bené (W-B) rule [16] which predicts the formation of Ni_2Ge as the first phase in the Ni/Ge system.

The second and final phase was found to be NiGe. Its formation was detected at temperatures of 170 ^oC and 239 ^oC in the first and second samples respectively. Whereas the first phase in the Ni-Ge system is reported differently by different authors there is a consensus on the second and final phase NiGe. The formation of NiGe at 239 ^oC is in reasonable agreement with the results reported by Hsieh et al. [13]. We observed the growth of the NiGe phase in the temperature ranges from 170-333 ^oC and 239-333 ^oC in the first sample and second sample respectively. Marshal et al. [67], Wittmer et al. [81] and Patterson et al. [73] reported the formation of NiGe in the temperature ranges of 260-600 ^oC, 250-600 ^oC and 200-300 ^oC respectively. Mueller et al. [66] reported the formation of NiGe at 350 ^oC.

The formation of nickel germanides at low temperatures demonstrated in this study is agreement with the results reported by other workers [10-14]. This low reaction temperature is important for metal germanides in order to avoid degradation of high-*k* materials that are expected to be used for gate insulation instead of GeO_2 in Ge-based devices.

The growth of compound phases in thin films is generally known to be sequential. Our analysis of the first sample revealed an unusual simultaneous growth of the Ni_5Ge_3 and the NiGe phases in the presence of Ni. This simultaneous growth of the two phases was observed to last from the onset of the formation of the NiGe (170 ^oC) phase until 254 ^oC. Starting from 255 ^oC the NiGe phase was forced to decompose until 272 ^oC where the thickness of NiGe had dropped to about 54×10^{15} at/cm^2. The reasons for this rather strange behavior are not very clear but it could probably have resulted from a phase competition between the Ni_5Ge_3 and NiGe phases which favored the former phase over the latter phase. It is equally not very clear why the NiGe maintained an almost constant thickness of about 54×10^{15} at/cm^2 in the temperature window between 272 ^oC and 298 ^oC instead of decomposing completely. However, the NiGe phase was observed to resume its growth with a very rapid growth rate after all the Ni was totally consumed around 298 ^oC. This rapid growth resulted from the thermal dissociation of the Ni_5Ge_3 phase.

This exceptional behavior of simultaneous growth of Ni_5Ge_3 and NiGe while Ni is still present during the annealing treatment diverges from the observation that phases should form sequentially in thin film systems. However, this observation is in agreement with the results of Nemouchi et al. [72] who also reported the simultaneous growth of Ni_5Ge_3 and NiGe. Nemouchi et al. [72] argued that the observed simultaneous growth seems to manifest due to the low critical thickness of Ni_5Ge_3 which they found to be around 10 nm. In a comprehensive study of thin film reactions of 20 transition metals with germanium by Gaudet et al. [80] the simultaneous growth of multiple phases for Ni, Pt, cobalt (Co), iridium (Ir), and iron (Fe) films on Ge substrates was also reported. This simultaneous growth of phases in the Ni-Ge thin film system is similar to what is observed in bulk diffusion couples.

In the Ni-Ge system the first phase has been reported differently by different researchers. Gaudet et al. [10] ascribes the observation of different phase sequences to differences in film thicknesses, microstructure and annealing conditions. Gaudet et al. [10] further argued that it is possible for a phase that is present only in a narrow temperature window during annealing to be inadvertently missed in anneal-and-quench experiments where temperature intervals are typically greater than 25 ^oC. This particular problem does arise in the in situ real-time experiments. The above argument by Gaudet et al. [10] could contribute to the observation of different phase sequences for the same materials system. Differences in phase formation temperatures and in the phase sequence when the substrate was changed from crystalline to amorphous Ge have been

reported by Gaudet et al. [10] in their comprehensive study of thin film reactions of 20 transition metals with Ge.

A very thin layer of Ta was interposed between the Ge substrate and the overlying layers in each sample. This acted as an inert marker to monitor the direction of atomic mobility during the Ni-Ge reaction process. Using this Ta marker, the DDS during the formation of the Ni_5Ge_3 and NiGe phases were successfully identified. Analysis of RBS data from the sample with configuration Ge<100>/Ta(5 Å)/Ni(800 Å) showed a complete interlayer inversion in which all the Ta atoms moved to the surface of the sample at the end of the reaction. This would not have been the case if there was diffusion of Ge during the formation of Ni_5Ge_3 because this would have resulted in the formation of a germanide layer above the Ta marker. Formation of a nickel germanide above the marker would have effectively trapped the Ta causing it to fail to reach the surface. From this observation Ni was unambiguously identified as the sole diffusing species during the formation of Ni_5Ge_3. Since Ta was at the surface of the sample and the Ni_5Ge_3 underneath, this meant that Ta could not monitor the direction of atomic mobility during the formation of NiGe; NiGe formation in the first sample took place entirely below the Ta marker. This necessitated an alteration of the sample configuration. Therefore the identification of the mobile species during the formation of NiGe was done on the basis of results from the sample with configuration Ge<100>/Ta(6 Å)/Ge(490 Å)/Ni(470 Å). This sample configuration forced the Ni_5Ge_3 phase to form above the Ta marker without the Ni diffusing to the substrate which enabled us to identify the diffusing species during formation of the NiGe phase.

The identification of the diffusing species during NiGe formation was achieved by using two different approaches. Firstly, it was observed that if there was no diffusion of Ge then the total amount of Ge in the germanide above the marker at the end of the reaction would be the same as the amount of Ge above the marker in the as-deposited sample. A simple atomic calculation showed that the total amount of Ge in the final germanide (NiGe) above the marker increased by about 12%. This is a confirmation that there was Ge diffusion from the substrate. Secondly, the observed progressive movement of the marker towards the surface indicated that the dominant formation mechanism of the NiGe layer above the marker was $Ni_5Ge_3 \rightarrow 3NiGe + 2Ni$ and not $Ni_5Ge_3 + 2Ge \rightarrow 5NiGe$. This is the only source of Ni that diffused across the Ta to produce the observed progressive outward movement of the Ta signal. Since the Ni freed from the dissociation reaction forms NiGe below the marker, a plot of the total NiGe growth against the

NiGe growth above the marker should yield a straight line with a slope of 5/3 or 1.67. The NiGe that formed below the marker before decomposition of Ni_5Ge_3 then appears as the intercept of this line. If a 100% diffusion of the Ni released from the decomposition mechanism occurred, the gradient of the graph of the total NiGe growth as a function of the NiGe growth above the Ta marker would be exactly 1.67. When this straight line was plotted a slope of 1.46 was obtained. This gives a difference in the slope of 0.21 which is 12.5% of 1.67. This shows that only 87.5% of the Ni freed from the decomposition mechanism diffused across the Ta to the substrate and the remainder reacted above the marker. We see that the only phase above the marker at the end of the reaction is NiGe. This means that an equal number of Ge atoms should have diffused from the substrate across the marker to react with the freed Ni above the marker. Since there is a one-to-one ratio of Ge to Ni atoms in the NiGe phase the amount of Ge that diffuses across the marker also translates to about 12.5% of Ge that was originally above the marker. This observation is in agreement with the findings from the atomic calculation method. These two results indicate unambiguously that both Ni and Ge diffused during the formation of NiGe. According to our first calculation the ratio of the number of Ni atoms that diffused across the marker to the number of Ge atoms that diffused across the marker from the substrate is about 88:12. This shows that although both Ni and Ge diffused during the formation of NiGe, Ni was still the dominant diffusing species. Since the literature surveyed did not yield any information on which species moves during the formation of Ni_5Ge_3 and NiGe, no comparisons could be made with our results. Therefore, to the best of our knowledge the absence of information about DDS during the formation of both Ni_5Ge_3 and NiGe shows that this is the first time that the DDS during Ni_5Ge_3 and NiGe has been quantitatively determined.

By estimating the atomic density of Ni_5Ge_3 the activation energy for the solid state diffusional growth of this germanide was estimated from the slope of the Kissinger plot. The activation energy of diffusional growth of the Ni_5Ge_3 phase was found to be 0.98 ± 0.03 eV. This result was in close agreement with that of Nemouchi et al. [71] who reported the activation energy of diffusion for Ni_5Ge_3 growth to be 0.8 eV.

The possibility of using Ge in deeply scaled MOSFETs has been made attractive by the successful demonstration of replacing high-*k* materials over thermally grown SiO_2 as new gate dielectrics in CMOS devices. However, the metal germanides for use in Ge-based devices must be formed at low temperatures in order avoid degradation of the high-*k* materials based gate

dielectrics. This study has demonstrated low temperature formation of nickel germanides. A room temperature formation of Ni_5Ge_3 on α-Ge was observed in the second sample. The growth of Ni_5Ge_3 was also observed at a low temperature of about 145 ^oC in the sample without Ge above the Ta. The second and last phase during the SPR of Ni with Ge was found to NiGe. The growth of this phase was equally detected at low temperatures in both samples. In the sample without Ge above the Ta marker, the growth of NiGe was found to have started at around 170 ^oC. In the sample with Ge above the marker, the growth of this phase below and above the marker was found to have started around 239 ^oC and 249 ^oC respectively. Knowledge of the temperature at which each phase forms is of paramount importance for industrial applications as it can determine the heat treatment required to obtain a unique targeted phase with specific properties.

For device integrity, it is important to identify the dominant diffusing species during the formation of each phase as it can influence their thermal stability. In device manufacture it is often found that when the substrate element (Si or Ge) is the DDS, this results in overgrowth and bridging in devices, which in turn has a detrimental effect on their performance. Although recent studies have shown that NiGe and PdGe are the most promising candidates for contact materials with germanium [10], little is known about the kinetics of these germanides formation and reports about the diffusing species during formation of these monogermanides are missing in literature. By monitoring the movement of the marker as a function of growth it was possible to determine which species diffused at every stage of the nickel germanide growth. Therefore, the single most important contribution of this study is the identification of the DDS during the formation of both Ni_5Ge_3 and NiGe which has not yet been reported in any other study of the Ni/Ge system. In this study, Ni was unambiguously identified as the sole diffusing species during the formation of Ni_5Ge_3. It was further established from this study that both Ni and Ge diffuse during the formation of NiGe. Although both Ni and Ge were mobile during the formation of NiGe, it was established that Ni was still the dominant diffusing species. Given that very little is known about diffusing species during germanide growth, it is hoped that the results obtained from this investigation will be of great interest to the thin film research community and of benefit to the microelectronic industry where NiGe films are targeted for applications in microelectronic circuits.

Binary equilibrium phase diagrams (see Fig. 1.7) show the presence of many phases but only some of these phases form during solid state reactions in thin film diffusion couples. It is

therefore of interest to determine which of the many phases present in the phase diagram forms first and the order in which the subsequent phases form. In the Ni/Ge system, there is still a controversy regarding formation of the first phase which is reported differently by different researchers. When the two samples used in our investigation were thermally annealed by linearly ramping the temperature, only two compound phases were observed in the Ni/Ge system. In both samples, the phase that formed first was found to be Ni_5Ge_3. The final phase was identified to be NiGe. The two phases grew sequentially in the second sample as expected in thin films. On the other hand, the reaction of Ni with Ge in the first sample showed rather an uncommon behaviour for a thin film formation in which a simultaneous growth of Ni_5Ge_3 and NiGe in the presence of Ni was observed at a later stage of the reaction. Therefore, this study has established the phase formation sequence of the nickel germanides to be Ni_5Ge_3 followed by NiGe. It is hoped that these findings will contribute to the body of knowledge that will eventually resolve the controversy surrounding the first phase formation in the Ni/Ge system.

The literature surveyed showed that the solid state reactions in the Ni/Ge system have not been investigated before using in situ real-time RBS. This could probably be due to the excessive overlapping of Ni and Ge peaks which has been demonstrated in Chapter 3. Nevertheless, this study has shown that with the computer programs such as RUMP it is possible to use RBS to study a system like Ni/Ge binary system in there is excessive overlap of peaks. One of the many advantages of in situ real-time RBS is that different types of analyses can be performed on the same data. In this way, the activation energy for the solid state diffusional growth of Ni_5Ge_3 was estimated. Since activation energy is a measure of the easy with which a phase can be formed, it would have been better to determine the activation energy of diffusional of the NiGe because it is one the promising candidates for contact materials with germanium [10]. However, this could not be done because the density of NiGe was not available from literature surveyed at the time of writing the dissertation.

The distinct advantage of in situ real-time RBS in providing continuous observations of the solid state reactions between Ni and Ge has been demonstrated for planar binary thin film diffusion couples in this study. Thin film diffusion couples and bulk diffusion couples are the two extreme regimes in which solid state reaction can be investigated. Although the lateral diffusion couple regime forms the bridge between the two extreme regimes, application of in situ real-time RBS

to binary diffusion couples in the lateral diffusion couple regime was not considered in this work and is thus one area in which future research could be conducted.

Appendix A

Thermocouple calibration

The relationship between the actual sample temperature and the temperature reading of the thermocouple embedded in the copper heating stage was determined by melting Au-Si (T_m = 363 ^oC) and Al-Si (T_m = 577 ^oC) samples. The surface resistance was measured as a function of the thermocouple temperature. The resistance was measured using the standard four point probe geometry. Both of these systems are simple eutectics with no intermetallic phases. The melting of a eutectic is not a thermally activated process and results in a large and abrupt change in resistance. The melting point temperatures measured by the thermocouple were 382 ^oC and 610 ^oC for the Au-Si and Al-Si systems respectively. The actual eutectic temperatures are 363 ^oC and 577 ^oC respectively. Using this information and assuming a linear correlation a calibration curve was plotted and is presented in the Fig. A1below. This calibration allows the temperature reading

of the thermocouple to be converted to the true sample temperature at any point during the annealing. The curve shows that the temperature reading of the thermocouple is equal to the true sample temperature at 73 ^{o}C.

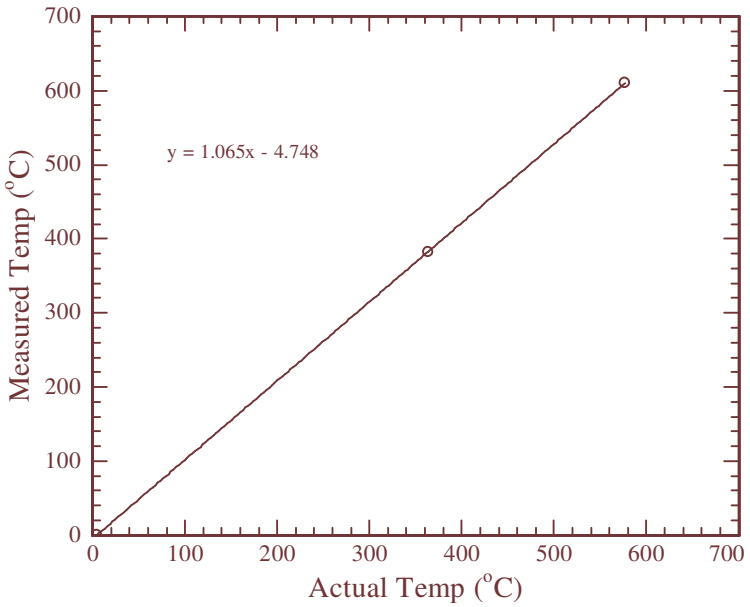

Figure A. 1: Thermocouple calibration curve using the Au-Si and Al-Si eutectic melting points by measuring the surface resistance.

Bibliography

[1] C.O. Chui, H. Kim, D. Chi, B.B. Triplett, P.C. McIntyre, and K.C. Saraswat, "A sub-400 ^{o}C germanium MOSFET technology with high-k dielectric and metal gate," *IEDM Tech. Dig*., (2002) 437–440.

[2] A. Ritenour, S. Yu, M.L. Lee, N. Lu, W. Bai, A. Pitera, E.A. Fitzgerald, D.L. Kwong, and D.A. Antoniadis, "Epitaxial strained germanium p-MOSFETs with HfO_2 gate dielectric and TaN gate electrode", *IEDM Tech. Dig*., (2003) 433–436.

[3] H. Shang, H. Okorn-Schmidt, K.K. Chan, M. Copel, J. A. Ott, P.M. Kozlowski, S.E. Steen, S.A. Cordes, H.-S. P. Wong, E.C. Jones, and W.E. Haensch, "High mobility p-channel germanium MOSFETs with a thin Ge oxynitride gate dielectric", *IEDM Tech. Dig*., (2002) 441–444.

[4] C.O. Chui, S. Ramanathan, B.B. Triplett, P.C. McIntyre, and K.C. Saraswat, "Germanium MOS Capacitors Incorporating Ultrathin High-k Gate Dielectrics", *IEEE Electron Device Lett*., **23** (8) (2002) 473-475.

[5] Michel Houssa and Marc Heyns, 2004. "High-*k* gate dielectrics: why do we need them?" In: *High-k Gate Dielectrics*, Michel Houssa (ed), 3-14, Bristol and Philadelphia: Institute of Physics Publishing.

[6] M. Depas, B. Vermeire, P.W. Mertens, R.L. Van Meirhaeghe and M.M. Heyns, "Determination of tunnelling parameters in ultra-thin oxide layer poly-. $Si/SiO_2/Si$ structures", *Solid-State Electron.*, **38** (8) (1995) 1465-1471.

[7] S.H. Lo, D.A. Buchanan, Y. Taur and W. Wang, "Quantum-mechanical modeling of electron tunneling current from the inversion layer of ultra-thin-oxide nMOSFET's", *IEEE Electron. Dev. Lett.*, **18** (1997) 209-211.

[8] G. D. Wilk, R. M. Wallace, and J. M. Anthony, "High-k gate dielectrics: Current status and materials properties considerations," *J. Appl. Phys.*, **89** (10) (2001) 5243-5275.

[9] H. Shang, K.L. Lee, P. Koslowski, C. D'Emic, I. Babich, E. Sikorshi, M. Ieong, H.S.P. Wong, K. Guarini and W. Haensch, " Self-aligned n-channel germanium MOSFETs with a thin Ge oxynitride gate dielectric and tungsten gate", *IEEE Electronic Device Lett.*, **25** (3) (2004) 135-137.

[10] S. Gaudet, C. Detavernier, A.J. Keliock, P. Desjardins and C. Lavoie. "Thin film reaction of transition metals with germanium", *J. Vac. Sci. Technol. A* **24** (3) (2006) 474-485.

[11] M. Tinani, A. Mueller, Y. Gao, E.A. Irene, Y.Z. Hu and S.P. Tay, "In situ real-time studies of nickel silicide phase formation", *J. Vac. Sci. Technol. B* **19** (2) (2001) 376-383.

[12] R. Nath, C.W. Soo, C.B. Boothroyd, M. Yeadon, D.Z. Chi, H.P. Sun, Y.B. Chen, X.Q. Pan and Y.L. Foo, "NiGe on Ge(001) by reactive deposition epitaxy: An *in situ* ultrahigh-vacuum Transmission-electron microscopy study", *Appl. Phys. Lett.* **86** (2005) 201908.

[13] Y.F. Hsieh, L.J. Chen, E.D. Marshall, S.S. Lau and N. Kawasaki, "Partial epitaxial growth of Ni_2Ge and NiGe on Ge(111)", *Thin Solid films* **162** (1988) 287-294.

[14] G.A. Smith, Li Luo and W.W. Gibson, "Ion Channeling Study of Nickel Metal Growth on Ge<111> at Room Temperature", *J. Vac. Sci. Technol., A. Vac. Surf. Films,* **9** (3) (1991) 646-648.

[15] D. Mangelinck, J.Y. Dai, J.S. Pan and S.K. Lahiri, "Enhancement of thermal stability of NiSi films on (100)Si and (111)Si by Pt addition", *Appl. Phys. Lett.* **75** (1999) 1736-1738.

[16] R.M. Walser and R.W. Bené, "First phase nucleation in silicon-transition-metal planar interfaces" *Appl. Phys. Lett.* **28** (1976) 624-625.

[17] R.W. Bené, "First nucleation rule for solid-state nucleation in metal-metal thin-film systems", *Appl. Phys. Lett.* **41** (6) (1982) 529.

[18] B.Y. Tsuar, S.S. Lau, J.W. Mayer and M.-A. Nicolet, "Sequence of phase formation in planar metal-Si reaction couples", *Appl. Phys. Lett.* **38** (1981) 922.

[19] U. Gösele and K.N. Tu, "Growth kinetics of planar binary diffusion couples: "Thin-film case" versus "Bulk cases"", *J. Appl. Phys.* **53(4)** (1982) 3252-3260.

[20] M. Ronay, "Reinvestigation of First Phase Nucleation in Planar Metal-Si Reaction Couples", *Appl. Phys. Lett.* **42(7)** (1983) 577.

[21] G. Ottavian, "Metallurgical aspects of the formation of silicides", *Thin Solid Films* **140** (1986) 3-22.

[22] F.M. d'Heurle, "Nucleation of a New Phase from the Interaction of Two Adjacent Phases: Some Silicides," *Mater. Res.* **3** (1988) 167-195.

[23] L. Zhang and D.G. Ivey, "A kinetic model for silicide formation through thin-film metal-silicon reactions", *Appl. Phys. Lett.* **71** (1992) 4314-4328.

[24] C.V. Thompson, "On the Role of Diffusion in Phase Selection During Reactions at Interfaces" *J. Mater. Res.* **7** (1992) 367.

[25] R. Pretorius, "Prediction of silicide first phase and phase sequence from heats of formation", *Mater. Res. Soc. Symp. Proc.* **25** (1984) 15.

[26] R. Pretorius, "Phase sequence of silicide formation at metal-silicon interfaces", *Vacuum* **41** (4-6) (1990) 1038-1042.

[27] R. Pretorius, R. de Reus, A.M. Vredenberg and F.W. Saris, "Use of the effective heat of formation rule for predicting phase formation sequence in Al-Ni systems", *Mater. Lett.* **9** (12) (1990) 494-499.

[28] R. Pretorius, A.M. Vredenberg, F.W. Saris and R. de Reus, "Prediction of phase formation sequence and phase stability in binary metal-aluminum thin-film systems using the effective heat of formation rule", *J. Appl. Phys.* **70** (7) (1991) 3636-3646.

[29] R. Pretorius, T.K. Marais, A.E. Muller and D. Knoesen, "PREDICTION OF FIRST PHASE FORMATION AT Au-METAL INTERFACES USING THE EFFECTIVE HEAT OF FORMATION MODEL", *Mater. Res. Soc. Symp. Proc.*, **238** (1992) 475.

[30] T.K. Marais, E. Tayor, M. Ndwandwe, B. Spoelstra and R. Pretorius, "Prediction and characterization of compound phase formation at Ge-metal interfaces in thin film structures", *Nucl. Instrum. Methods Phys. Res. Sect. B,* **85** (1994) 183-187.

[31] R. Pretorius, T.K. Marais and C.C. Theron, "Thin film compound phase formation sequence: An effective heat of formation model", *Mater. Sci. Eng. Res.*, **10** (1-2) (1993) 1- 83.

[32] E. Colgan, B.Y. Tsaur and J.W. Mayer, "Phase Formation in CR-SI Thin-Film Interactions", *Appl. Phys. Lett.* **37** (1981) 938.

[33] B.Y. Tsaur, J.W. Mayer and M.-A. Nicolet, "Sequence of phase formation in planar metal-silicon reaction couples", *Appl. Phys. Lett.* **38** (1981) 922.

[34] O. Kubaschewski and C.B. Alcock, 1979. *Metallurgical Thermochemistry,* 5th ed. Oxford: Pergamon.

[35] A.M. Brown and M.F. Ashby, *Acta Materialia* **28** (1980) 1085.

[36] C.C. Theron, O.M. Ndwandwe, J.C. Lombaard and R. Pretorius, "First phase formation at interfaces: Comparison between Walser and Bené and efectiveheat of formation model", *Materials Chemistry and Physics* **46** (1996) 238-247.

[37] Y.F. Hsieh, L. J. Chen, E. D. Marshall and S. S. Lau, "Partial epitaxial growth of cobalt germanides on (111)Ge", *Appl. Phys. Lett.* **51** (20) (1987) 1588.

[38] M.G. Grimaldi, I. Wielunski, M-A. Nicolet and K.N.Tu, *Thin Solid Films* **21** (1981) 207.

[39] O. Thomas, S. Delage, F.M. d'Huerle and G. Scilla,"Reaction of titanium with germanium and silicon-germanium alloys", *Appl. Phys. Lett.* **54** (1989) 228-230.

[40] Marc-A. Nicolet and S.S. Lau, 1983. "Formation and Characterization of Transition-Metal Silicides", in: *VLSI Electronics: Microstructure Science,* N. Einspruch and G.B. Larrabee (eds), 329-464, New York: Academic Press.

[41] P. Gas and F. M. d'Heurle, "Formation of silicide thin films by solid state reaction", *Appl. Surf. Sci.,* **73** (1993) 153-161.

[42] Johan Seger, 2005. Interaction of Ni with SiGe for electrical contacts in CMOS technology. Ph.D. Thesis, Royal Institute of Technology (KTH), Stockhom, Sweden.

[43] P. Gas, F.M. d'Heurle, F. LeGoues and S.J. La Placa, "Formation of intermediate phases, Ni_3Si_2 and Pt_6Si_5: Nucleation, identification, and resistivty", *J. Appl. Phys.* **59** (10) (1986) 3458-3466.

[44] F.M. d'Heurle, 1983. IBM RC Report 10422 Publications Dept. IBM Research Yorktown Heights New York.

[45] W.C. Roberts-Austen, "On the diffusion of metals", *Phil. Trans. Roy. Soc.,* **A 187** (1896) 383-415.

[46] R. F. Mehl, *Trans. AIME (American Institute of Mining and Metallurgical Engineers),* **122** (1936) 11-56.

[47] W. Schockley, "The theory of p/n junctions in semiconductors and p/n junction transistors", *Bell Sys. Tech. Journal*, **28** (7), (1949) 436-489.

[48] C.-D. Lien, M.-A. Nicolet and S.S. Lau, "Kinetics of silicides on Si<100> and evaporated silicon substrates", *Thin Solid Films* **143** (1986) 63.

[49] P. Gas and F. d'Heurle, 1998. *Numerical and functional relationships in Science and Technology, Vol. III 33 A*, Landolt-Börnstein, Berlin.

[50] A.D. Smigelkas and E.O. Kirkendall, "Zinc diffusion in alpha brass", *Trans. AIME* **171** (1947) 130-134.

[51] A. Fick, "Uber diffusion", *Progg. Ann.* **94** (1855) 59.

[52] G. V. Hevesy and W. Seith-Freiburg, "Diffusion in metallen", *Z. Electrochem.* **37** (1931) 528-531.

[53] G. Grube and A. Jedele, "Diffusion und korrosion von kupfer-nickel-Legierungen", *Z. Electrochem.*, **38** (1932) 799-807.

[54] Pauli Laitinen, 2004. Self and Impurity Diffusion in Intrinsic Relaxed Silicon-Germanium. Ph.D. Thesis, University of Jyväskylä.

[55] Brian Tuck, 1974. *Introduction to Diffusion in Semiconductors*, Stevenage: Peter Peregrinus.

[56] F.C. Frank and D. Turnbull, "Mechanisms of Diffusion of Copper in Germanium", *Phys. Rev.* **104** (1956) 617-618.

[57] V.B. Glazmann and G.S. Maykeǹkaya, *Izv. Akad. Nauk. Kuz. SSR, Ser. Fiz. Mat.* **15** (1977) 28.

[58] S. Geodecker, T. Deutsch and L. Billard, *Appl. Phys. Lett.*, **88** (2002) 235501.

[59] I. Kaur, Y. Mushin and W. Gust, 1995. *Fundamentals of grain and interphase boundary diffusion*, New York: John Wiley and Sons.

[60] D. Turnbull, "Grain Boundary and Surface Diffusion", *Trans. A.S.M.*, **43A** (1951) 129.

[61] G. Samsonov and V.N. Bondarev, 1970. *Germanides*, New York: Primary Sources.

[62] ASM International's Binary Alloy Phase Diagrams CD-ROM, ASM International, Materials Park, OH.

[63] Qingchun Zhang, Nan Wu, Thomas OSIPOWICZ, Lakshmi Kanta BERA and Chunxiang Zhu, "Formation and Thermal Stability of nickel germanide on germanium substrate", *Japanese Journal of Applied Physics* **44** (45) (2005)

[64] L.J. Lin, K.L. Pey, W.K Choi, E.A. Fitzgerald, D.A. Antoniadis, A.J. Pitera, M.L. Lee, D.Z. Chi and C.H. Tung, "The interfacial reaction of Ni with (111)Ge, (001)$Si_{0.75}G_{0.25}$ and (100)Si at 400 ^{o}C", *Thin Solid films* **462-463** (2004) 151-155.

[65] Sankar Dhar, Tapobrata Som and V. N. Kulkarni, "Ion-induced room temperature synthesis of low resistivity nickel germanide", *J. Appl. Phys.* **83** (4) (15 February 1998) 2363-2365.

[66] M. Mueller, Q.T. Zhao, C. Urban, C. Sandow, D. Buca, S. Lenk, S. Estévez and S. Mantl, "Shottky-barrier height tuning of NiGe/n-Ge contacts using As and P segregation", *Materials Science and Engineering B* **154-155** (2008) 168-171.

[67] E. D. Marshall, C. S. Wu, C. S. Pai, D. M. Scott and S. S. Lau, "Metal-Germanium Contacts and Germanide Formation", *Mater. Res. Soc. Symp. Proc.* **47** (1985) 161-166.

[68] H. Takizawa, K. Uheda, and T. Endo, "$NiGe_2$: a new intermetallic compound synthesized under high pressure", *J. Alloys Compd.* **305** (2000) 306.

[69] R. Nath, C.W. Soo, C.B. Boothroyd, M. Yeadon, D.Z. Chi, H.P. Sun, Y.B. Chen, X.Q. Pan and Y.L. Foo, "NiGe on Ge(001) by reactive deposition epitaxy: An *in situ* ultrahigh-vacuum Transmission-electron microscopy study", *Appl. Phys. Lett.* **86** (2005) 201908.

[70] G. A. Smith, Li Luo and W.W. Gibson, "Ion Channeling Study of Nickel Metal Growth on Ge<111> at Room Temperature", *J. Vac. Sci. Technol., A. Vac. Surf. Films,* **9** (3) (1991) 646-648.

[71] F. Nemouchi, D. Mangelinck, J.L. Lábár, M. Putero, C. Bergman and P. Gas, "A comparative study of nickel silicides and nickel germanides: Phase formation and kinetics", *Micro Electronic Engineering* **83** (2006) 2101-2106.

[72] F. Nemouchi, D. Mangelinck. C. Bergman, G. Clugnet and P. Gas, "Simultaneous growth of Ni_5Ge_3 and NiGe by reaction of Ni films with Ge", *Appl. Phys. Lett.* **89** (2006) 131920.

[73] D.M. Kim and A.J. Ardell, "Coarsening of Ni_3Ge in binary Ni-Ge alloys: Microstructure and volume fraction dependence of kinetics", *Acta Materialia* **51** (2003) 4073-4082.

[74] Y. Jin and C. Chaturvedi, "Crystallographic Study of Ni_2Ge Phase in Binary Ni-Ge Alloy System", *Acta Materialia* **44** (9) (2003) 3833-3845.

[75] A. Antolak, D. Oleszak, M. Petala and T. Kulik, "Structure and magnetic properties of mechanically alloyed Ni-Ge and Co-Ge Alloys", *Materials Science and Engineering A* **449-451** (2007) 440-443.

[76] L. Perring, J.J. Kuntz, F. Bussy and J.C. Gachon, "Heat capacity measurements on the equiatomic compounds in Ni-X (X = Al, In, Si, Ge, and Bi) and M-Sb (M = Ni, Co, and Fe) systems", *Intermetallics* **7** (1999) 1235-1239.

[77] S. L. Liew, R.T.P. Lee, B. Balakrisnan, S.Y. Chow, M.Y. Lai and D.Z. Chi, "Enhanced morphologicalstability of NiGe films formed using Ni(Zr) alloy", *Thin Solid films* **504** (2006) 104-107.

[78] Dedong Han, Yi Wang, Dayu Tian, Wei Wang, Xiaoyan Liu, Jinfeng Kang and Ruqi Han, "Studies in Ti- and Ni-germanide Shottky contacts on n-Ge(100) substrates", *Microelectronic Engineering* **82** (2005) 93-98.

[79] S. Gaudet, C. Detavernier, C. Lavoie, and P. Desjardins, "Reaction of thin Ni films with Ge: Phase formation and texture", *J.Appl. Phys.,* **100** (2006) 034306

[80] M.W. Wittmer, M.-A. Nicolet and J.W. Mayer, "The First Phase to Nucleate in Planar Transition Metal-Germanium Interfaces", *Thin Solid Films* **42** (1977) 51-59.

[81] J. Ken Patterson, B.J. Park,K. Ritley, H.Z. Xiao, L.H. Allen and A. Rockett, "Kinetics of Ni/a-Ge reactions", *Thin Solid films* **253** (1-2) (1994) 456-461.

[82] S.-L. Hsu,C.-H. Chien, M.-J. Yang, R.-H. Huang, C.-C, Leu, S.-W. Shen and T.-H. Yang, "Study of therma stability of nickel monogermanide on single- and polycrystalline germanium substrates", *Appl. Phys. Lett.* **86** (2005) 251906-1251906-3.

[83] F. Nemouchi, *Reactivite de Films nanométriques de nickel sur Substrats Silicium-Germanium* (Université Paul Cezzane Aix-Maiseille III, Faculté de Sciences et Technique de Saint Jérôme, 2005).

[84] F. Nemouchi, V. Carron, J. L. Lábár, M. Putero, L. Ehouarne, B. Arrazat, Y. Morand, J. P. Barnes, D. Mangelinck, Y. Campidelli and O. Kermarrec, "Dopant Effect On NiGe Texture During Nickel Germanide Growth", *ECS Transactions* **6** (16) (2007) 49-59.

[85] T.B. Massalski, 1986. *Binary Alloy Phase Diagrams*, American Society for Metals, Ohio: Metal Park.

[86] C. Lavoie, F.M. d'Heurle, C. Detavernier and J.C. Cabral, "Towards implementation of a nickel silicide process for CMOS technologies", Microelectron. Eng. Mater. Adv. Metall. **70** (2-4) (2003) 144-157.

[87] P. Gergaud, C.R. Rivero, M. Gailhanou, O. Thomas, B. Frome and H. Jaouen, "Exploring Ni–Si thin-film reactions by means of simultaneous synchrotron X-Ray diffraction and substrate curvature measurements", *Mater. Sci. Eng. B* **114-115** (2004) 67-71.

[88] M. Ellner, T. Goedecke and K. Schubert, "The Structure of Ni-Ge Alloys", *J. Less-Common Met.*, **24** (1971) 23-40.

[89] C.C. Theron, J.C. Lombaard and R. Pretorious, "Real-time RBS of solid state reaction in thin films", *Nuclear Instruments and Methods in Physics Research B* **161-163** (2000) 48-55.

[90] L.R. Doolittle, "A Semi-automatic Algorithm for Rutherford Backscattering Analysis", *Nucl. Instrum. Methods Phys. Res., Sect. B*, **15** (1986) 227-231.

[91] L.R. Doolittle, "Algorithm for rapid simulation of Rutherford Backscattering Spectra", *Nucl. Instrum. Methods Phys. Res., Sect. B*, **9** (1985) 344.

[92] Wei-Kan Chu, James W. Mayer and Marc-A. Nicolet, 1978. Backscattering Spectrometry, New York: Academic Press.

[93] A.B. Brown, C.W. Snyder, W.A. Fowler and C.C. Lauritsen, "Excited States of the Mirror Nuclei, Li^7 and Be^7", *Phys. Rev.* **82,** (1951) 159-181.

[94] Kenji Kimura, 2000. "Rutherford Backscattering Spectrometry", in: *Encyclopedia of Analytical Chemistry*, R.A. Meyers, Ed, 12809-12823, Chichester, © John Wiley & Sons Ltd.

[95] Leonard C. Feldman and James W. Mayer, 1986. *Fundamentals of Surface and Thin Film Analysis*. New York/Amsterdam/London: Elsevier/North-Holland.

[96] J. Saarilahti and E. Rauhala, "Interactive Personal Computer Data Analysis of Ion Backscattering Spectra", *Nucl. Instrum. Methods Phys. Res., Sect. B*, **64** (1992) 734-738.

[97] J. Saarilahti and E. Rauhala, "GISA computer program", *Nucl. Instrum. Methods Phys. Res., Sect. B*, **64** (1992) 734.

[98] M.D. Strathman and S. Bauman, "Angle-Resolved Imaging of Single Crystal Maetrials with MeV Helium Ions", *Nucl. Instrum. Methods Phys. Res., Sect. B*, **64** (1992) 840-845.

[99] SIMNRA computer program, http://www.rzg.mpg.de/ma/.

[100] M. Mayer, 1997. "SIMNRA User's guide", Technical Report IPP 9-113 `Max-Planck-Institut fur Plasmaphysik Garching German.

[101] J. Demeulemeester, D. Smeets, C. Van Bockstael, C. Detavernier, C.M. Comrie, N.P. Barradas, A. Vieira, and A. Vantomme, "Pt redistribution during Ni(Pt) silicide formation", *Appl. Phys. Lett*. **93** (2008) 261912.

[102] N.P. Barradas and A. Vieira, "Artificial neural networks for the analysis of Rutherford Backscattering data", *Phys. Rev. E* **62** (2000) 5818.

[103] A. Kling, "CASSIS – a new Monte-Carlo computer program for channelling simulation of RBS, NRA, and PIXE", *Nucl. Instrum. Methods Phys. Res., Sect. B*, **102** (1995) 141-144.

[104] C. Jeynes, N.P. Barradas, P.K. Marrott, G. Boudreaud, M. Jenkin, E. Wendler and R.P. Webb,"Elemental thin film depth profiles by ion beam analysis using simulated annealing - a new tool", *J. Phys. D: Appl. Phys.*, **36** (2003) R97-R126.

[105] N. P. Barradas, C. Jeynes and R.P. Webb, "Simulated Annealing Analysis of Rutherford Backscattering Data", *Appl. Phys. Lett*. **71** (1997) 291-293.

[106] Leopold Palmetshofer, 2002. "Rutherford Backscattering Spectroscopy (RBS)", in: *Surface and Thin Film Analysis: Principles, Instrumentation, Applications*, H. Bubert and H. Jenett, Eds, Verlag GmbH: Wiley-VCH.

[107] G.S. Hartley, "Diffusion and swelling of high polymers Part I: The swelling and solution of a high polymer solid considered as diffusion process", *Trans. Faraday Soc.* **46** (1946) 6-11.

[108] D.M. Scott and M.-A. Nicolet, "Implanted oxygen in NiSi formation" *Phys. Status Solidi* (a) **66** (2) (1981) 773-778.

[109] J. Baglin, F. d'Heurle and S. Petersson, "An alternative marker experiment in the formation of Mo and W silicides", *Appl. Phys. Lett*. **33** (4) (1978) 289.

[110] T.G. Finstad, "Silicide Formation with Nickel and Platinum Double Layers on Silicon", *Thin Solid Films* **51** (1978) 411.

[111] L.S. Darken, "Diffusion, mobility and their interrelation through free energy in binary metallic systems", *Trans. AIME* **175** (1948) 184-201.

[112] C.M. Comrie and J. M. Egan, “Diffusion of silicon in Pd_2Si during silicide formation”, J. Appl. Phys. **64** (3) (1988) 1173-1177.

[113] Chu, W. K. and Kraütle, H. and Mayer, J. W. and Müller, H. and Nicolet, M.-A. and Tu, K. N. (1974) “*Identification of the dominant diffusing species in silicide formation”, Appl. Phys. Lett.* **25** (8) (1974) 454-457.